TECHNICAL ADVANCES IN NEUTRON POLARIMETRY AND STUDIES OF THE (p,n) REACTION IN ^{13}C

By

NELSON VIDELA

A THESIS

Submitted to the Faculty of Graduate Studies In Partial Fulfillment of the Requirements for the degree

DOCTOR OF PHILOSOPHY

Department of Physics
University of Manitoba,
Winnipeg, Manitoba

October, 1984

TECHNICAL ADVANCES IN NEUTRON POLARIMETRY AND STUDIES OF THE (P,N) REACTION IN ^{13}C

BY

NELSON VIDELA

A thesis submitted to the Faculty of Graduate Studies of the University of Manitoba in partial fulfillment of the requirements of the degree of

DOCTOR OF PHILOSOPHY

ABSTRACT

TECHNICAL ADVANCES IN NEUTRON POLARIMETRY AND STUDIES OF THE (p,n) REACTION IN ^{13}C

The asymmetry in the $^{4}He(\vec{n},n)^{4}He$ reaction has been measured at three different incident neutron energies: 19.40; 22.85 and 27.31 MeV, and 120^{0} from forward direction. Values of the asymmetry have been used to calculate the polarization of fast neutrons produced in the $^{13}C(p,\vec{n})^{13}N$.

The $^{13}C(p,\vec{n})^{13}N$ reaction was studied as part of a programme being undertaken at the University of Manitoba Cyclotron Laboratory to study (p,n) reactions linking isobaric analog states of mirror nuclei in the energy range of 22 to 50 MeV. The study involves a comparison of the proton analyzing power, A(θ), in the reaction $^{13}C(\vec{p},n)^{13}N$ to the neutron polarization in the inverse reaction $^{13}C(p,\vec{n})^{13}N$. The importance of the comparison between these two observables is based in Conzett's polarization-analysing power theorem for time reversed reactions, the theorem states that the proton analyzing power in the reaction $^{13}C(\vec{p},n)^{13}N$ is equal to the neutron polarization in the reaction $^{13}C(p,\vec{n})^{13}N$ provided the reaction proceeds between members of an isospin doublet and when charge symmetry and time reversal invariance hold exactly. However isospin symmetry is broken by the Coulomb interaction. So comparison of analyzing power

A(θ) and polarization P(θ) should yield information on the breaking of isospin symmetry by the Coulomb force.

To carry out this experiment a high pressure helium-xenon polarimeter was designed and built; the polarimeter consist of a stainless steel cylinder closed at both end by two acrylic windows. The scintillations produced inside the polarimeter by the recoiling helium nuclei are transmited to two phototubes optically coupled to the acrylic windows. A remote controlled system for the filling and venting of the polarimeter was built and used during the experiment. This polarimeter was used as an analyzer in the asymmetry measurements.

Because of the low neutron flux, the experiments have been performed using two large (NE-213) side detectors and a broad geometry. Therefore it was necessary to correct the data for finite geometry and multiple scattering in the target using a Monte Carlo computer code.

At higher energies, around 50 MeV, there is a decrease in n-He scattering cross section and an increase of He-recoil range.This calls for a maximun target density; for this reason an existing liquid helium polarimeter was redesigned and built with the aim of improving the energy resolution and light collection efficiency.

OUTLINE OF THE THESIS

Chapter 1 is a brief theoretical introduction to the problem. It discusses the comparison between proton analyzing power and neutron polarization. These two observables should have the same magnitude(Sa58) for the reaction stated at a given cm energy and they have been proved by Byrd(By81,83) to be identical by means of spatial symmetry arguments in the case of (p,p) and (n,n) elastic scattering. However, they are not necessarily the same for (p,n) reactions. Departure from relation P=A could imply perhaps both

1) Isospin Symmetry breaking

2) An asymmetric spin-flip transition.

This is a very important statement and more data are needed for the comparison of the two observables especially within the energy range of the Manitoba Cyclotron.

Chapter 2 is divided into four sections. The first two sections describe the experimental arrangement and the electronics used. The experiment was carried out in two parts separated by 6 months however; the main features were common to both runs and for that reason emphasis is given to the description of the first part of the experiment. The third section is devoted to the work done in the design and construction of a high pressure ^{4}He gas polarimeter. Helium has been used for many years in the measurement of neutron polarization. It scintillates in both the liquid and gaseous states.

A liquid polarimeter has the advantage of having a much higher density than a gas polarimeter, however a gas polarimeter does not present any of the cryogenic problems related to the liquid helium polarimeter. Both are useful, and for practical reasons we have used the gas polarimeter in the experiment described in chapter 2. Section four describes a superconducting solenoid. In order to minimize the instrumental asymmetry introduced during the experiment a superconducting solenoid has become an integral part of most neutron polarimeter systems. The magnet allows rotation of the spin of the neutron through 180^0, thus interchanging the roles of the left and right detectors without exchanging their positions.

Chapter 3 is devoted to the analysis of the experiment. This includes measurement of the asymmetry and the corrections for finite geometry and multiple scattering using a Monte Carlo computer code. The polarization is then calculated using the experimental value of the asymmetry and the known value of the polarimeter analyzing power at 120^0. In order to compare the neutron polarization and the proton analyzing power, two entirely different experiments are necessary. The first is the one described in this thesis and the second is the experiment concerning the inverse reaction, which will be carried out in the not too distant future.

Chapter 4 is dedicated to the liquid helium polarimeter, its design and performance. An existing polarimeter(Bi68) has been redesigned in order to reduce the boil-off rate of liquid helium and improve the energy resolution.

ACKNOWLEDGEMENTS

I would like to express my gratitude to Professor J.S.C McKee for his effective supervision, guidance and unfailing support throughout the course of these investigations.

It is a pleasure to thank Dr. J.Birchall who has been involved in this project from the very beginning and has contributed a great deal of advice and practical help without which this project could not have been brought to a satisfactory conclusion.

I am grateful to the staff of the machine shop, especially to J. Lancaster for his advice and help during the early stages of the project.

Members of the so-called "PIXE-neutron" research group (past and present) have been understanding and supportive. They contributed a considerable amount of their time during the painstaking stage of data taking. Their efforts are appreciated by the author.

I wish to thank Dr. W.D.Ramsay who has read this thesis and made many helpful comments

Thanks are expressed to C.Lapointe his participation during the data taking and analysis of the experiment are appreciated.

Finally I especially thank my wife Elsa and my children Rodrigo, Patricia and Lucia, whose support and understanding through the years has been crucial.

TABLE OF CONTENTS

Page

LIST OF FIGURES

LIST OF TABLES

CHAPTER 1

THEORETICAL BACKGROUND

1.1 INTRODUCTION

The nuclear force is spin-dependent. Early work of Mayer and Jensen on the nuclear shell model established that it was necessary to include in the nuclear Hamiltonian terms which explicitly contain spin. The realization that spin-dependent forces are fundamental to the nuclear interaction led to experiments which are selective in emphasizing such spin-dependent effects. Throughout the past decade polarised nucleon beams have been used extensively for this purpose, and this program has already greatly improved our detailed understanding of the nucleon-nucleon interaction.

The comparison between the neutron polarization and the proton analyzing power for (p,n) reactions on light nuclei has been a subject of interest for many years. The two observables should have the same magnitude (Sa58). At low energy, the Lane model, in its simplest version neglects the spin of the target, and for this case Byrd(By81,83) showed that the values calculated for the observables are indeed identical by spatial symmetry for (p,p) and (n,n) elastic scattering. However, they are not necessarily the same for (p,n) reactions.

At low energies the reaction mechanisms involve a non-direct contribution which can result in a more complicated relationship between the $P(\theta)$ and $A(\theta)$ observables. In particular, differences between $P(\theta)$ and $A(\theta)$ can be produced by processes which

[illegible] and spin-flip transitions(By83).

The equality of proton analysing power and neutron [illegible] has been demonstrated by H.E. Conzett(Co74), and is known as Conzett's theorem. The theorem states that the analyzing power, [illegible] in the reaction $A(\vec{p},n)B$, should be equal to the polarization, [illegible] in the reaction $A(p,\vec{n})B$ provided A and B are isobaric analog [illegible] and that $A(p,n)B$ is quasielastic.

This theorem is based on the assumption that the (p,n) [illegible] connects isobaric analog states. Consequently one [illegible] the results to be more nearly correct if the target and [illegible] nuclei are members of an isospin doublet (mirror nuclei, [illegible] closer if they are members of a larger isospin multiplet. This [illegible] a $\Delta T_z = 1$ (p,n) transition between members of an isospin [illegible] corresponds to a 180^0 rotation in isospin space and [illegible] which under this operation only requires the limited assumption of [illegible]. On the other hand, conservation of isospin for a $\Delta T = 0$ transition between members of a larger ($T \geq 1$) isospin [illegible] requires complete rotational invariance in isospin space [illegible] be synonymous with the more general assumption of charge [illegible].

Arnold(Ar77) on the other hand has expressed the [illegible] ($P = A$) in terms of transition probabilities T_{fi}, where [illegible] subscripts refer to the polarization of the initial proton and the [illegible]. Using "↑" and "↓" to denote spin up and spin down,

$$P(\theta) = (T_{\uparrow\downarrow} + T_{\uparrow\uparrow}) - (T_{\downarrow\downarrow} + T_{\downarrow\uparrow})$$

In the case of polarized incident beam, we measure the analyzing power $A(\theta)$ as the difference in sums over outgoing polarizations.

$$A(\theta) = (T_{\uparrow\uparrow} + T_{\downarrow\uparrow}) - (T_{\downarrow\downarrow} + T_{\uparrow\downarrow}) \qquad 1.1$$

We may now compare the polarization and analyzing power by expressing them as a difference in transition probabilities, i.e.,

$$P(\theta) - A(\theta) = 2(T_{\uparrow\downarrow} - T_{\downarrow\uparrow}) \qquad 1.2$$

If we now define the spin-flip $S(\theta)$ probability as

$$S(\theta) = T_{\uparrow\downarrow} + T_{\downarrow\uparrow}$$

and the spin-flip asymmetry $\Delta S(\theta)$ as

$$\Delta S(\theta) = T_{\uparrow\downarrow} - T_{\downarrow\uparrow} = (A-P)/2 \qquad 1.3$$

Probabilities, $T_{\uparrow\downarrow}$ and $T_{\downarrow\uparrow}$ are both positive, therefore algebraically their sum and difference are related by:

$$|T_{\downarrow\uparrow} - T_{\uparrow\downarrow}| \leq T_{\uparrow\downarrow} + T_{\downarrow\uparrow}$$

$$|\Delta S| \leq S \qquad 1.4$$

$$|A(\theta) - P(\theta)| \leq ?S \qquad 1.5$$

From equations (1.3) to (1.5) above we can extract some very important conclusions with respect to the difference between the analyzing power and the polarization. First from (1.4), $\Delta S \neq 0$ is obtained only with a non-zero spin-flip probability $S \neq 0$. Since spin flip is forbidden for a spin-zero target by parity conservation, we obtain the trivial result that $P \equiv A$ for that case. This result suggests that target spin may be a necessary consideration in understanding cases of $P \neq A$. Further, to obtain $P \neq A$, the $\Delta S \neq 0$ condition (1.3) states that spin flip alone is insufficient; one must have an asymmetric spin flip, i.e., unequal probabilities for $T_{\uparrow\downarrow}$ and $T_{\downarrow\uparrow}$.

The arguments mentioned above indicate that an asymmetric spin-flip mechanism is a necessary condition for $P \neq A$. These arguments may be combined to obtain the following two minimum requirements for observation of $P \neq A$ in (p,n) mirror reactions:

1) isospin symmetry breaking, and

2) an asymmetric spin-flip transition.

The principle of measuring the degree of polarization of a beam of fast neutrons is well known. The beam is elastically scattered by a sample the analyzer, composed of nuclei chosen so that neutrons with spin "up" are scattered preferentially to one side, while those with spin "down" are scattered preferentially to the other. The resulting asymmetry in scattering is equal to the product of polarization of the incident beam and the analyzing power, which must

be known in order to determine the polarization of the incident neutron beam. For the special case of elastic scattering the analyzing power is equal to the polarization that would result if an unpolarized beam of neutrons of the same energy were scattered through the same angle. Experimentally the left-right asymmetry is calculated from the expression:

$$\varepsilon = \frac{N_L - N_R}{N_L + N_R} \qquad 1.6$$

Then using the expression $\varepsilon = P(\theta)A(\theta)$ the polarization can be calculated, or one can proceed in the reverse mode; using a beam of known polarization measure the asymmetry and then calculate the analyzing power. The measurement of the asymmetry is customarily done by means of a double scattering. Polarized neutrons are produced in a nuclear interaction, either directly in a charged-particle induced reaction or else by elastic scattering of unpolarized neutrons produced previously in some charged particle induced reaction. After such a polarized neutron beam is scattered by a sample, the neutron must be detected by means of another nuclear process, e.g., (n,p) scattering in a scintillator.

Most neutron detectors are not effective energy spectrometers, this means some method of energy discrimination must be contrived in order to obtain polarization information for all elastic

scattering measurements when the inelastic channel is open, or for the highest-energy neutron group produced in a charged-particle induced reaction. For this reason neutron experiments have concentrated on scattering from H, D, ^{4}He, ^{12}C, ^{16}O, and most reaction studies involve light nuclei where the groups of neutrons are well separated in energy. Both time of flight techniques and coincidence spectrometers (where the scatterer or analyzer are in a scintillator form), have been employed to obtain varying degrees of energy resolution.

In order to minimize the instrumental asymmetry introduced during the experiments a superconducting solenoid has become an integral part of most neutron polarimeters. The magnet allows one to rotate the spin of the neutrons through 180^{0}, thus interchanging the roles of the left and right detectors without changing their position.

The one nucleus for which the most complete set of neutron analyzing power data exists is ^{4}He and, in consequence, is the most useful analyzer. It has been widely used in both the liquid and gaseous states. In both forms it scintillates. This feature is used to discriminate against the high background present in a neutron experiment.

In the last few years a significant contribution to the comparison of the $P(\theta)$ and $A(\theta)$ observables at low energy has been undertaken at the Triangle Universities Nuclear Laboratory (TUNL). This comparison of $P(\theta)$ and $A(\theta)$ includes (p,n) reactions on ^{3}H, ^{9}Be, ^{11}B and ^{13}C nuclei (By83a), (To81), (Mu81). Their approach

extended the polarization-analyzing power theorem(Bi59) for the elastic scattering of nucleons to include a quasielastic model of (p,n) reactions. This argument compared the bombarding energy E_p to the Coulomb displacement energy Δ_c between the initial and final states. Equality of P(θ) and A(θ) would be expected at energies E_p greater than about $3\,\Delta_c$.

The conclusions of this group for the measurements of (p,n) reactions on light nuclei from ^{3}H to ^{15}N are that these measurements now provide a fairly complete picture of the differences between P(θ) and A(θ) in (p,n) reactions on light nuclei at low energy(up to 11 MeV). Although additional shell-model calculations will be required to obtain detailed information about the source of the differences or their sensitivity to nuclear structure parameters, some relatively simple arguments have been able to explain most of the dependence on target mass and bombarding energy. In particular (1) the quasielastic approximation (By83) shows that P(θ)=A(θ) for energies $E_p \geq 3\,\Delta_c$, (2) Arnold's discussion (Ar77) of the spin-flip asymmetry S(θ) shows that ΔS(θ)=0 is a necessary condition for P(θ)=A(θ), and (3) the isospin symmetry arguments of Conzett (Co74) and Wilkinson(Wi56) suggest an explanation for the dependence of differences on bombarding energy and target mass. Again, these simple arguments can only suggest situations in which a difference might exist; further shell-model calculations will be needed to predict whether a difference should actually be observable or to provide a detailed explanation of its significance.

Birchall and McKee (Bi81) showed that asymmetry of the spin flip is, in fact a consequence of the breaking of charge symmetry or time reversal invariance. The argument used in this case is that the (p,n) cross-section for σ_{ud} can be transformed into the (n,p) cross-section for σ_{du} under detailed balance, spatial rotation, and charge symmetry. On the other hand, Byrd et al(By83b) claim that this point of view does not take into account the microscopic nature of time reversal. According to them the comparison of the two observables in practice is impossible. From the "microscopic" point of view the time reversal invariance constraint connects scattering states which cannot be created experimentally, such as coherent combinations of incoming spherical waves. This distinction between macroscopic reaction and microscopic reversibility indeed has very important consequences.

Biedenharn(Bi59) identified the actual relationship between the P(θ) and A(θ) observables for a pair of inverse experiments $a+A \rightleftarrows b+B$. If for example two experimentally observed states $|a+A\rangle$ and $|b+B\rangle$ are represented in terms of microscopic states of definite total angular momentum, $|\alpha\rangle$ and $|\beta\rangle$, then the polarization P(θ) is given in terms of the S-matrix by the weighted summation over the amplitudes $S_{\beta\alpha} = \langle\beta|S|\alpha\rangle$. This is a very important statement, because the equality P(θ) = A(θ) at the macroscopic level has been reduced to a requirement of microscopic reciprocity for each value of angular momentum, that is, to the equality $|S_{\beta\alpha}| = |S_{\alpha\beta}|$. Then it is necessary to find the connection between time reversal invariance (TRI) and reciprocity. Coester(Co51) showed that invariance under time reversal

requires that $S_{\beta\alpha} = S_{\alpha t,\beta t}$ where $|\alpha_t>$ and $|\beta_t>$ are time reversed versions of the microscopic states involved in the P(θ) and A(θ) experiments. The transitions represented by $S_{\alpha t,\beta t}$ are not directly involved in the A(θ) experiment. These transitions are dynamically possible but experimentally very improbable. Coester(Co51) extended the connection between a reaction and its time reverse to obtain $S_{\alpha\beta} = S_{\beta\alpha}$ which provides the necessary connection between the microscopic transitions in the actual P(θ) and A(θ) experiments.

The argument to discuss possible mechanisms for differences between P(θ) an A(θ) could be inverted. If a process is invariant under time reversal, then its S-matrix is symmetric (in a particular choice of representation) and P(θ) for any binary reaction is identically equal to A(θ) for the inverse reaction. Observation of a difference between P(θ) and A(θ) would be a direct violation of reciprocity between the inverse reactions and therefore also a violation of time reversal invariance.

The above discussion stresses even more the necessity of collecting more information to compare the two observables, especially in the range of medium energy, i.e., between 20 and 50 MeV.

CHAPTER 2

EXPERIMENTAL METHOD

2.1 INTRODUCTION

In this chapter a description is given of the equipment and the electronic circuitry used in the measurement of neutron polarization by means of n-^{4}He elastic scattering.

The unpolarized proton beam from the University of Manitoba Spiral Ridge Cyclotron impinges on a ^{13}C target, producing partially polarized neutrons via the $^{13}C(p,\vec{n})^{13}N$ reaction. These neutrons are then scattered from a high pressure helium target used as an analyzer and detected by two identical NE-213 detectors located at symmetric angles from the analyzer.

The experiment was carried out over two different periods of time. The first consisted of runs at 23.2 and 26.8 MeV incident proton energy, and the second part an extension to 31.1 MeV incident proton energy.

During experiments, the background plays an important role. This background comes from neutrons scattering directly from the target assembly or indirectly from the laboratory walls, floor, etc. A component of the background is induced by gamma-rays i.e there are neutron or gamma-induced events. It is very important therefore to be able to separate neutrons from gammas, the real events from the random background and to separate groups of different energies. This has been done using two different techniques.

2.2 Recoil Energy Analysis

This enables the analysis of the energy pulse to be made according to both its pulse height and pulse shape. The pulse height gives the total energy deposited in the detector while the shape gives the decay time information which varies with the type of particle. There is thus a straightforward connection between recoil energy and the energy of a certain type of particle, and between the type of particle and the decay time of its recoil pulse. Further, recoil energies and the resulting pulse heights differ for different particles of the same energy, so pulse height analysis is capable of separating different types of events. Our basic neutron energy measurement uses the recoil-energy pulse height distribution from either hydrogen or helium scattering.

2.3 Time of Flight

The time of flight requirement provides a coincidence condition between target and detector, therefore identifying effectively the time-uncorrelated room background neutrons. If one is interested in determining the neutron velocity using the time of flight technique, some basic conditions must be fulfilled.

1. The starting time of the neutrons must be well defined i.e the duration of a beam burst must be short compared with the total flight time.

2. The detection time must be equally well defined.

3. The flight path must be known.

All the information about the experiment must be extracted from raw data which are simply electronic signals. In even the most complex case, these signals are only timing (anode or fast) pulses and linear (dynode or slow) pulses from each neutron detector, and from the He polarimeter. These raw signals are then processed for computer acquisition, a procedure which may require simple shaping alone or include complex combinations of discrimination, timing, and coincidence circuits.

During the experiment at 31.1 MeV proton energy we rearranged our electronic setup. However, the circuits kept essentially the same features.

Fig 2.1 Shows a plan view of the University of Manitoba Cyclotron Laboratory. The Cyclotron itself is a machine adjustable to produce a proton beam in the energy range of 20 to 50 MeV. Neutron time of flight and polarization experiments are carried out on the beam line marked "NEUTRON TIME OF FLIGHT FACILITY" in Fig 2.1. A complete description of the facility has been given by Ramsay(Ra80) and Watson(Wa79) and I will describe therefore only the most important features relevant to our experiments.

The ^{13}C target and a NE-102 viewing screen were mounted in a target holder at the center of the scattering chamber(41cm in diameter). The screen was used to aid the focusing of the beam at

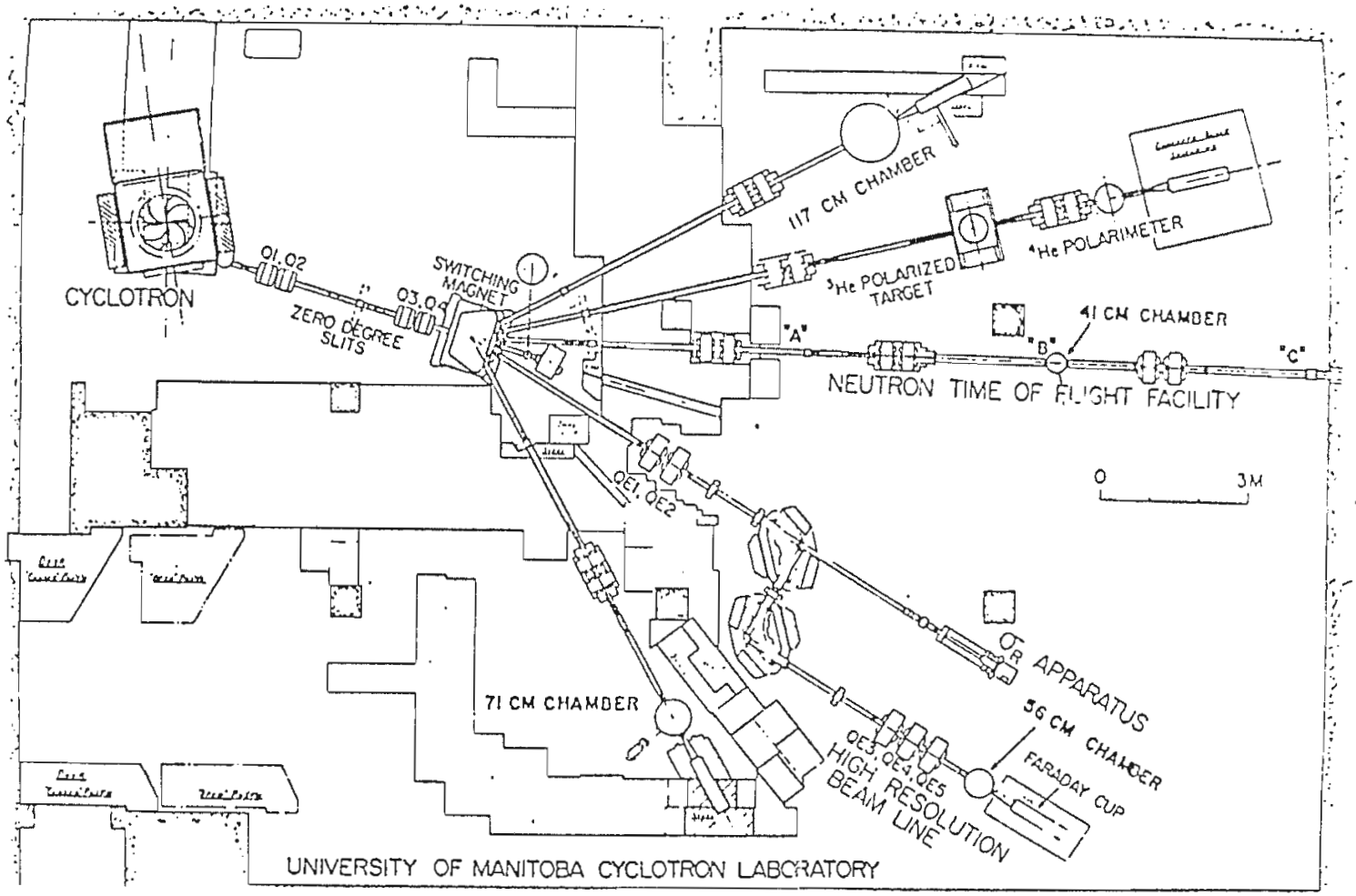

Fig. 2.1 Floor plan of the University of Manitoba Cyclotron Laboratory. The $^{13}C(p,\vec{n})^{13}N$ experiment was performed on the beam line marked "neutron time of flight facility".

the center of the target. The beamline downstream of the chamber up to the Faraday cup was assembled entirely of 15cm diameter pipe. This was done to reduce the neutron and gamma ray background that could result from the halo of beam hitting the pipe. The beam is collected in a Faraday cup downstream from the scattering chamber and the charge integrated in the usual manner. The location of the Faraday cup, 4m along a shaft bored 7m into the wall, is also important for reducing background. Very little radiation can be detected with the beam running through into the Faraday cup without a target in the chamber. The target itself was made from amorphous carbon enriched to 99% in ^{13}C. A special binder made of a mixture of 10 parts by weight of methylene chloride and 1 part by weight of polystyrene was injected into the target. This binder proved to be very useful. After a few minutes the methylene chloride evaporates, leaving the dissolved polystyrene injected into the target acting as a very strong binder. This binder enhances the target rigidity, thus eliminating the problems due to the target being too fragile. The charcoal-like powder was placed in a hydraulic pellet press and compacted into a carbon disc 1.9cm in diameter[+](the pressure used in the hydraulic pellet was around 24MPa).

-------- + Weighing the disc and dividing by its area indicated an average thickness of $25.0 \pm 0.2[mg/cm^2]$. This thickness produced a neutron flux of measurable intensity 3200neut/sec at 350cm from the scattering chamber with beam of $0.5\mu A$.

The beamline was aligned by using a theodolite. A number of points along the beamline were chosen and aligned with respect to a level line drawn on the wall of the experimental area specially for this purpose.

For the experiment it is necessary to know the angular position of the neutron detector with respect to the proton beam. Therefore we decided to scribe all these angles on the floor of the experimental room around the scattering chamber. This was accomplished by locating a laser on the floor under the beamline at the entrance of the beam to the experimental area. A few metres from this location, exactly under the scattering chamber, a mirror mounted on a rotary table was located on the floor. This was done with the help of a plumb-bob. The table is calibrated from 0 to 180^0, and has a built-in vernier scale able to read to an accuracy of $\pm 0.05^0$. The laser beam was turned on and the mirror rotated until the laser beam was reflected from the mirror to the center of the incident laser beam. In this position the center of the mirror is aligned with respect to the center of the target. Then, by simply rotating the table while the laser beam is on, we were able to mark on the floor the different angles of reflection of the laser beam from 0^0 to 180^0 around the scattering chamber.

The ^{4}He gas polarimeter was positioned at 40^0 from the incident proton beam, and 3.5m from the ^{13}C target. This particular angle was chosen mainly for practical reasons. The value of the differential cross section for this reaction(Ra80) is between 2.70

and 1.51 mb/sr in the energy range of 22.5 to 37.2 MeV, and relatively flat with angle. The asymmetry produced when the neutrons scatter from the ^{4}He analyzer is measured by two identical NE-213 detectors positioned at symmetric angles from the detectors (120^0). This angle corresponds to a maximum value of the analyzing power for the given energies (0.9).

The NE-213 neutron detectors are 11.4cm in diameter by 12.7 cm thick each coupled to an RCA-4522 photomultiplier. The assembly is mounted on a sturdy wheeled wagon which can be rolled around the area. The detectors are surrounded by 80cm of steel blocks on each side, and 20cm of steel on top and underneath. To reduce the room background the shielding was increased between the neutron detectors and the scattering chamber by adding two 91x81x61cm concrete blocks and two walls of approximately 20cm thick, one built from lead and the other from steel.

The background should be similar in the two side detectors and signal to noise should be maximised. The real count rate in the NE-213 side detector is given by

$$R \propto \frac{1}{L_1^2 . L_2^2} \propto \Omega_1 \Omega_2$$

where L_1 is the distance between the ^{13}C target and the polarimeter. L_2 is the distance between the polarimeter and the NE-213 detector, see fig 2.2.

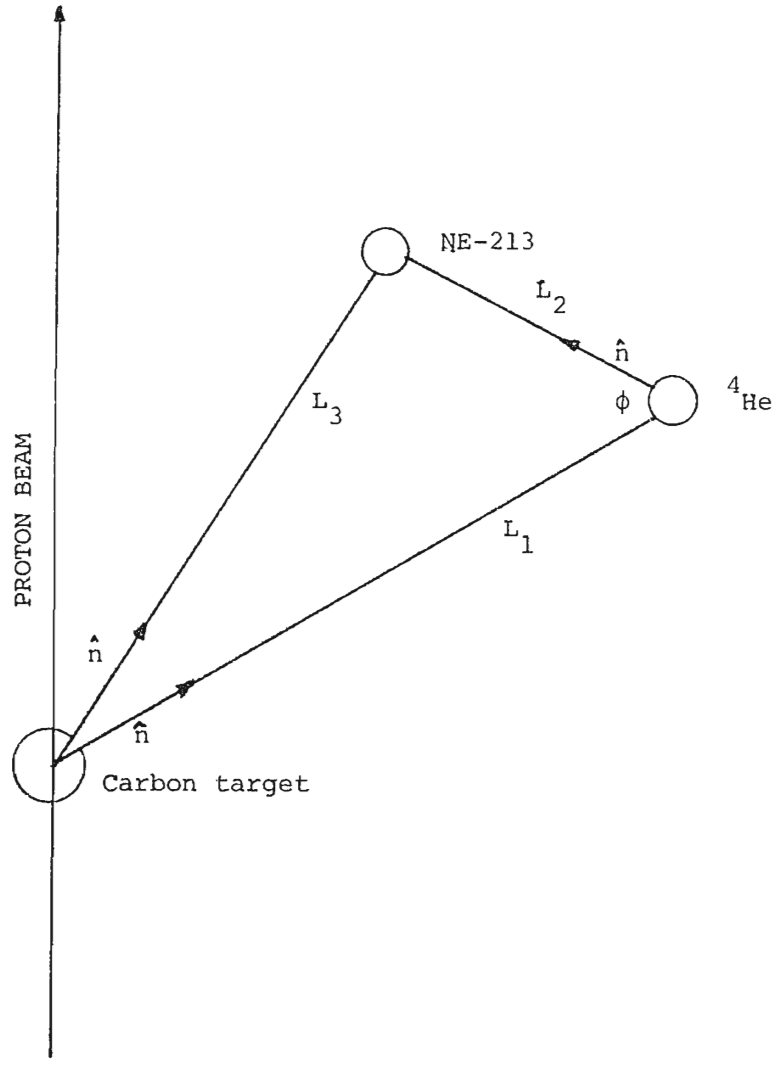

Fig. 2.2 Schematic diagram used to calculate the relation between the different distances during the experiment.

Keeping the quantity L_1L_2 fixed we keep the count rate fixed. Let us call $L_1L_2 = C$. Most of the background comes from random coincidences between the neutrons from the ^{13}C target travelling directly to ^4He and to a side detector and is given by

$$B \propto \frac{1}{L_1^2 \cdot L_3^2} \propto \Omega_1\Omega_3$$

where L_3 is the distance between the ^{13}C target and the NE-213 side detector(Fig 2.2). Then

$$B/R \propto L_2^2 / L_3^2$$

From geometry, $L_3^2 = L_1^2 + L_2^2 - 2L_1L_2\cos\phi$

Then

$$\frac{B}{1.} \propto \frac{L_2^2}{\frac{C^2}{L_2^2} + L_2^2 - 2C\cos\phi}$$

By inspection:

$$B/R \to 1 \text{ as } L_2 \to \infty$$

$$B/R \to 0 \text{ as } L_2 \to 0,$$

so it is necessary to choose a geometry in which L_1 is large and L_2

small. The worst case is given by $L_2 = 2L_1$. In order to keep the ratio of random background to real count rate less than one it is necessary to know by how much the neutron flux coming directly from the ^{13}C target must be attenuated. The real counting rate of the detector is related to the flux from the neutron source by the relation

$$N_r = N_1 \Omega_1 (\sigma \Omega_2) N_t \varepsilon$$

where

N_r = number of recoils counted per second by the detector,

N_1 = number of neutrons per steradian per second in the direction of the target,

N_t = number of ^4He nuclei per unit area,

Ω_1 = solid angle subtended at the source by the aggregate N_t

Ω_2 = solid angle subtended by the side detector at N_t

σ = neutron- ^4He differential cross-section,

ε = detection efficiency of NE-213 detector for neutrons scattered from ^4He.

The rate of random coincidences is given by:

$$N_R = 2N_1N_3\tau_r\varepsilon$$

where

N_3 = number of neutrons per steradian per second in the direction of the NE-213 detector,

τ_r = Coincidence resolving time,

ε = Efficiency of the ^{4}He scintillator.

Using these expressions the ratio of random to real counts calculated without shielding is about 600. This means the neutron flux coming directly from the ^{13}C target to the NE-213 side detector must be reduced by a factor of several hundred. When steel shielding is used around the detector this ratio is lowered by a factor of eight hundred which is enough to keep the ratio of random coincidence to real events much less than one. The further use of concrete shield reduces even more the ratio of random to real events by another factor of two hundred.

During the experiment we used a smaller NE-102 detector 4cm diameter by 2cm thick fitted with a 0.32cm diameter brass collimator and mounted on the side of the chamber at 30^0 from the center of the target and away from the neutron detectors. The NE-102 detector viewed the target through a 76μm Kapton-H window and its

purpose was to detect elastically scattered protons so as to extract the time structure of the beam with respect to the R.F. The count rate of the NE-102 detector was high enough to ensure that a usable time spectrum could be accumulated in about 3sec. In order to have a system able to resolve the different neutron groups it is necessary to tune the machine for a minimum beam burst width, so the neutrons coming from different beam bursts could be well separated. A routine was written to display the spectrum of the elastically scattered protons representing the time structure of the beam. This routine calculated the FWHM and the position of the centroid of the peak in a time of flight spectrum. If for any reason the centroid moved by one or more channels, a sound alarm was activated and we proceeded manually to trim the cyclotron parameters (R.F field and main magnet) to recover the centroid position and to minimize the width of the beam burst. During the first experiment a typical "time tune" of 0.8ns FWHM was obtained, while for the second experiment the "time tune" was about 1.0ns FWHM.

A further detector (NE-102 and NE-213 in the first and second runs, respectively) was positioned behind the gas polarimeter to monitor the neutron flux and the time of flight spectrum at the beginning of the experiment.

The effect of unequal neutron detection efficiencies, solid angle, and possible scattering angle differences between the left and right detectors was minimized by the use of a superconducting solenoid producing an axial magnetic field. The function of the solenoid was to precess the direction of the spin of the neutron

leaving the target through 180 degrees. In this way the roles of the left and right detectors could be reversed and first order systematic errors cancelled(At65). Stray magnetic field from the solenoid could affect the gain of the photomultipliers. For this reason it was necessary to use a magnetic shield in the form of a 1mm thick sheet of μ-metal between the solenoid and the polarimeter.

At 19.38, and 22.85MeV we performed three different runs. First we ran with no magnetic field. Then the superconducting solenoid was energized and we ran for approximately the same amount of time. Then the current in the solenoid was reversed and the run repeated.

Beam currents on target ranged from about 80 to 200nA, a typical figure being 140nA.

The second experiment at 27.31MeV neutron energy was repeated twice, first with no magnetic field, then we energized the solenoid and ran for the same amount of time.

Beam currents on target ranged from about 110 to 220 nA, a typical figure being 150 nA.

Fig 2.3 shows a schematic diagram of the experiments.

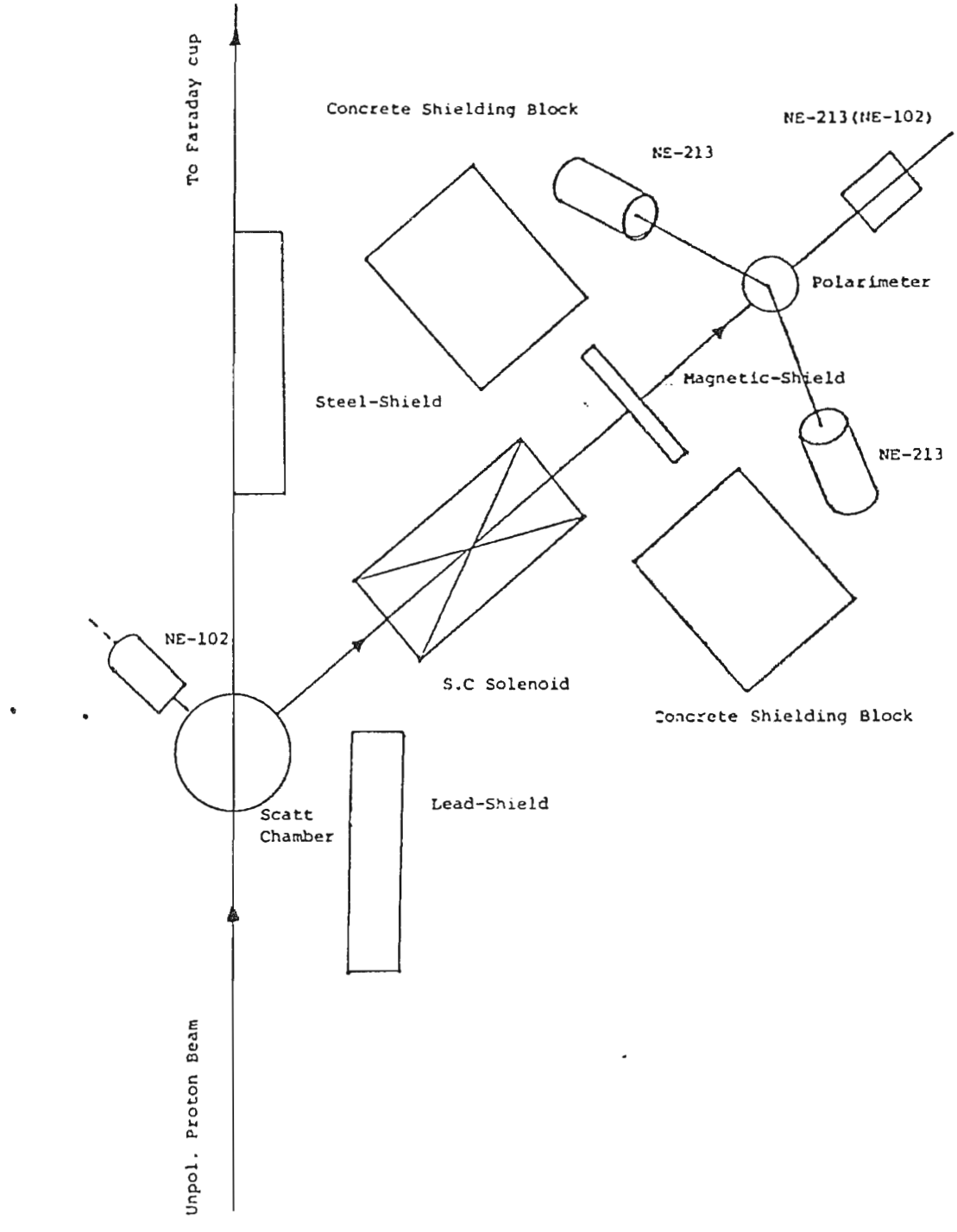
To Faraday cup
Concrete Shielding Block
NE-213(NE-102)
NE-213
Polarimeter
Steel-Shield
Magnetic-Shield
NE-213
NE-102
S.C Solenoid
Concrete Shielding Block
Scatt
Chamber
Lead-Shield
Unpol. Proton Beam

2.4 MULTIPLE SCATTERING IN THE TARGET

When the proton beam travels through the ^{13}C target the multiple scattering and energy loss produced in the target gives rise to two important processes; angular divergence and energy spread.

The angular divergence determines the amount of beam getting to the Faraday cup, smears out the angular distribution of (p,n) events and introduces a relatively small energy spread.

The energy spread gives the energy spread of the neutron beam (which must be less than the 2.37MeV excitation energy of the first state of ^{13}N) and smears out the cross-section and polarization over energy.

2.4.1 ANGULAR DIVERGENCE

Beam angular divergence produced by multiple scattering has been estimated by making use of data derived from numerical calculations by Marion and Zimmerman(Ma67). The calculations are made according to an approximation to the theory of Nigan, Sundaresan and Wu (NSW59). The NSW theory employs the Dalitz single scattering cross-section of a relativistic Dirac particle by a screened Coulomb field, calculated up to the second order in the Born approximation, and describes multiple scattering, especially at large angles, more accurately than the Moliere theory (Mo47). The approximate NSW theory gives for the angular distribution F(x) of multiply scattered particles:

$$F(x) = [1/(\chi_0^2 B)][F_0 + (1/B)F_1 + \{1/(2B^2)\}F_2], \qquad 2.1$$

where

$$F_0 = 2\exp(-x^2),$$

$$F_1 = -\frac{1}{4}\int_0^\Gamma u^3 J_0(ux)\ln(\tfrac{1}{4}u^2)\exp(-\tfrac{1}{4}u^2)du,$$

$$F_2 = \frac{1}{16}\int_0^\Gamma u^5 J_0(ux)[\ln(\tfrac{1}{4}u^4)]\exp(-\tfrac{1}{4}u^2)du. \qquad 2.2$$

x is related to the scattering angle θ through the relation

$$X = \theta/(\chi_c B^{\frac{1}{2}}),$$

here

$$\chi_c^2 = 0.1569[Z(Z+1)z^2/A][t/(pv)^2] \qquad 2.3$$

and B is a constant related to the average number of scatterings and is the root of the equation

$$B - \ln B = b, \qquad 2.4$$

where

$$b = \ln[2730\{(Z+1)Z^{1/3}z^2 t/(A\beta^2)\}] - 0.1544. \qquad 2.5$$

The remaining parameters are given below

J = Bessel function of zero order,

z = atomic number of incident particle,

Z = atomic number of scattering foil,

t = thickness of foil (g/cm),

A = atomic weight of foil material,

pv = [momentum][velocity of incident particle](MeV)

β = v/c

α = zZ/137

The upper limit of the integrals in (2.2) is given by

$$\Gamma = 2B^{\frac{1}{2}} \exp[(B - 1.5)/2.2]$$

Marion and Zimmerman have calculated and tabulated F(x) for values of B equal to 4, 5, 6, 7, 8, 9, 10, and 12. It is found that reliable results are not obtained if the number of collisions of the particle in the foil is less than about 10-20. Cases are therefore only considered for which B is greater than or equal to 4. The theory also becomes inaccurate if the foil is thick, since the NSW theory assumes no energy loss during collisions. A reasonable criterion to judge the applicability of the theory is that the particle must lose less than about 20% of its initial energy in the foil. In calculating the value of the parameter β the mean energy in the target should be used.

In order to calculate the mean energy and the energy

spread of the neutron beam it is necessary to know the energy loss and mean energy. These two quantities have been calculated using tables of energy loss(Ja66). Table 2.1 gives the results of these calculations.

TABLE 2.1

BEAM ENERGY [MEV]	ENERGY LOSS [MEV]	MEAN ENERGY [MEV]
23.3	0.504	23.04
26.9	0.452	26.67
31.1	0.401	30.89

In order to evaluate the angular divergence produced by the multiple scattering in the target we have to calculate the quantities χ_c and b given by equations (2.3) and (2.5) respectively, but the value of the energy entering the equation(2.5) through β must be the value of the mean energy evaluated in table 2.1. The values of b, B and χ_c calculated in this form are represented in table 2.2.

TABLE 2.2

ENERGY[MeV]	b	$\chi_c \cdot 10^{-3}$	B
23.04	7.09130	2.41	9.3239
26.67	6.9520	2.09	9.1677
30.89	6.8040	1.80	9.0014

The value of B is approximated by 9. The angular distribution function for B=9 is plotted in fig. (2.4). From the graph it can be seen that multiple scattering in the target produces an angular divergence of 0.52^{0} FWHM.

Instead of using this angle to evaluate the angular divergence the width parameter X_w is used. This parameter gives the angle at which the angular distribution has fallen to 1/e of its value at x=0. For a value of B=9 the calculated value of X_c is 0.927 then using

$$X = \theta_{1/e}/B^{\frac{1}{2}}X_c \qquad 2.6$$

in radians one can calculate the angle in degrees. Table 2.3 represents the value of the angular divergence for the three energies.

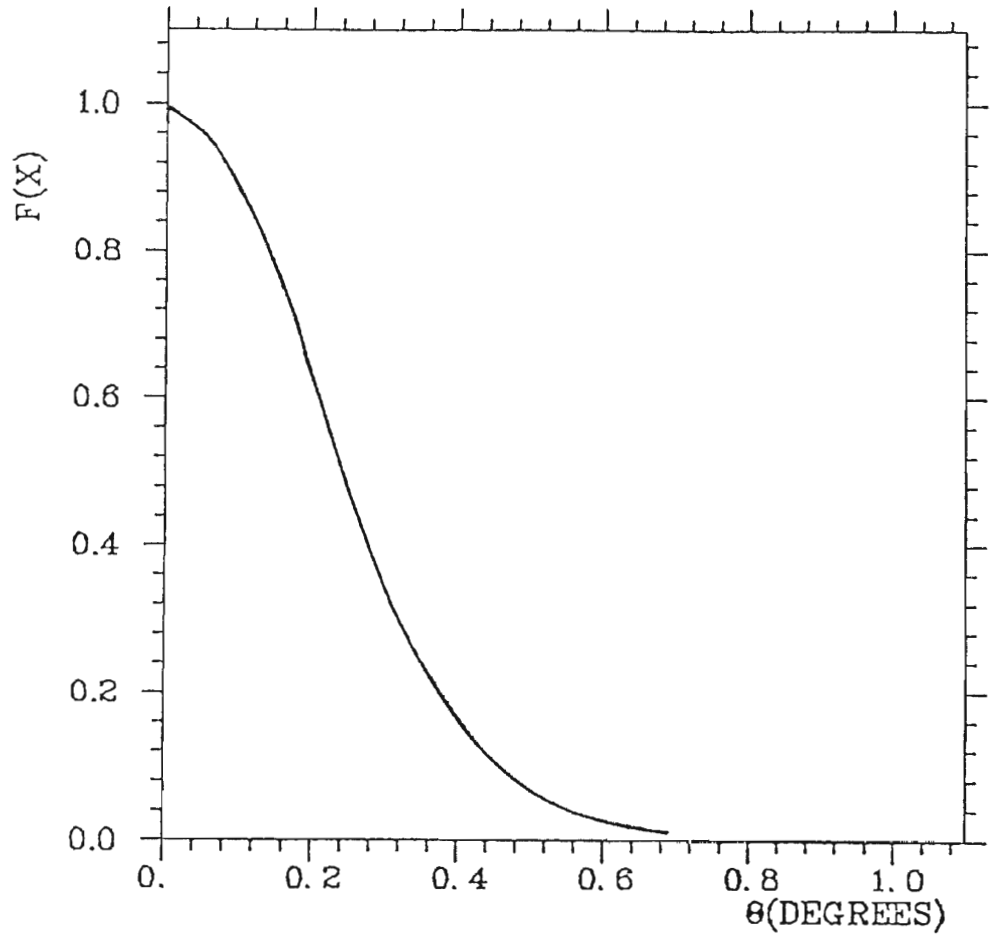

Fig. 2.4 Angular distribution function F(x) calculated using the parameter B=9, the FWHM in this case is 0.52^0

column 2 in table 2.3 gives the angular divergence produced by the ^{13}C target, column 3 gives the total anguiar divergence.

TABLE 2.3

ENERGY[MeV]	$\theta_{1/e}$	$\theta_{1/e}$
23.3	0.38	0.77
26.9	0.33	0.74
31.1	0.28	0.72

The particles scattered from the target are focused into the Faraday cup by the quadrupole magnet located behind the scattering chamber. It is possible then to calculate the fraction of particles scattered into the cone with a half angle θ_q which corresponds to the angle subtended by the quadrupole at the carbon target. This quantity is calculated using the expression

$$\Delta = \text{FRACTION} = \int_0^{\theta_q} [F(\theta)\sin\theta d\theta] / \int_0^{\theta_{max}} F(\theta)\sin\theta d\theta$$

where θ_{max} is the max angle of scattering. $F(\theta)$ becomes very small for a very large angle and the integration was cut off at this point. The results of these calculation are shown in table 2.4

TABLE 2.4

ENERGY[MeV]	FRACTION
23.3	0.9972
26.9	0.9931
31.1	0.9902

From these calculation one can see than more than 99% of the beam will be caught by the Faraday Cup. However the angular divergence produced by the multiple scattering in the target is a factor that should be taken into account when it is necessary to calculate cross sections and analyzing powers (because of smearing of differential cross-section by energy spread).

2.4.2 ENERGY RESOLUTION

The energy loss in the ^{13}C target produced an energy spread in the neutron beam equal to 0.25MeV (the energy spread of the beam in the beam line is around 0.25MeV). The total energy spread in the neutron beam is then 0.36MeV. This energy spread is small in comparison to the energy difference between the neutron ground state and the first excited state (2.37 MeV). In consequence it is no problem to differentiate between the two neutron groups, provided that the flight

path is long enough. The question of how long the flight path must be is indeed very important. For one thing, if overlap occurs between the fast neutron groups from one beam burst and slow neutrons from a previous beam burst, then a long flight path may not be wanted. If that is not the case then the experimenter would like to have a very long neutron flight path, if good neutron energy resolution is required. Clearly if two very fast neutron groups have almost the same energy, they will have to travel a long distance before the difference in their flight times becomes detectable. Kinematic calculations (Fig 2.5) show that the time difference between two neutron groups, ground state and first excited state (2.37MeV) produced by a 22MeV proton beam incident on ^{13}C target is 3.76ns for a flight path of 3.5m (from the ^{13}C target to the polarimeter). For a more energetic proton beam, say 30MeV incident on ^{13}C the time difference between the two neutron groups (for the same flight path) will be 2.4ns. To resolve the two neutron groups the system should have a resolution of better than 2.4ns. The timing resolution during the experiment was 1.0ns and in consequence we were able to resolve these two neutron groups.

Fig 2.6 represents the time of flight from the polarimeter to the side detectors(120^0 and 0.53m flight path) as a function of proton energy incident on ^{13}C the lower curve being the time of flight of the ground state neutron group produced in the $^{13}C(p,\vec{n})^{13}N$ and later scattered from the polarimeter. The top curve represents the first excited state neutron group produced in the same reaction and later scattered from the polarimeter to the side

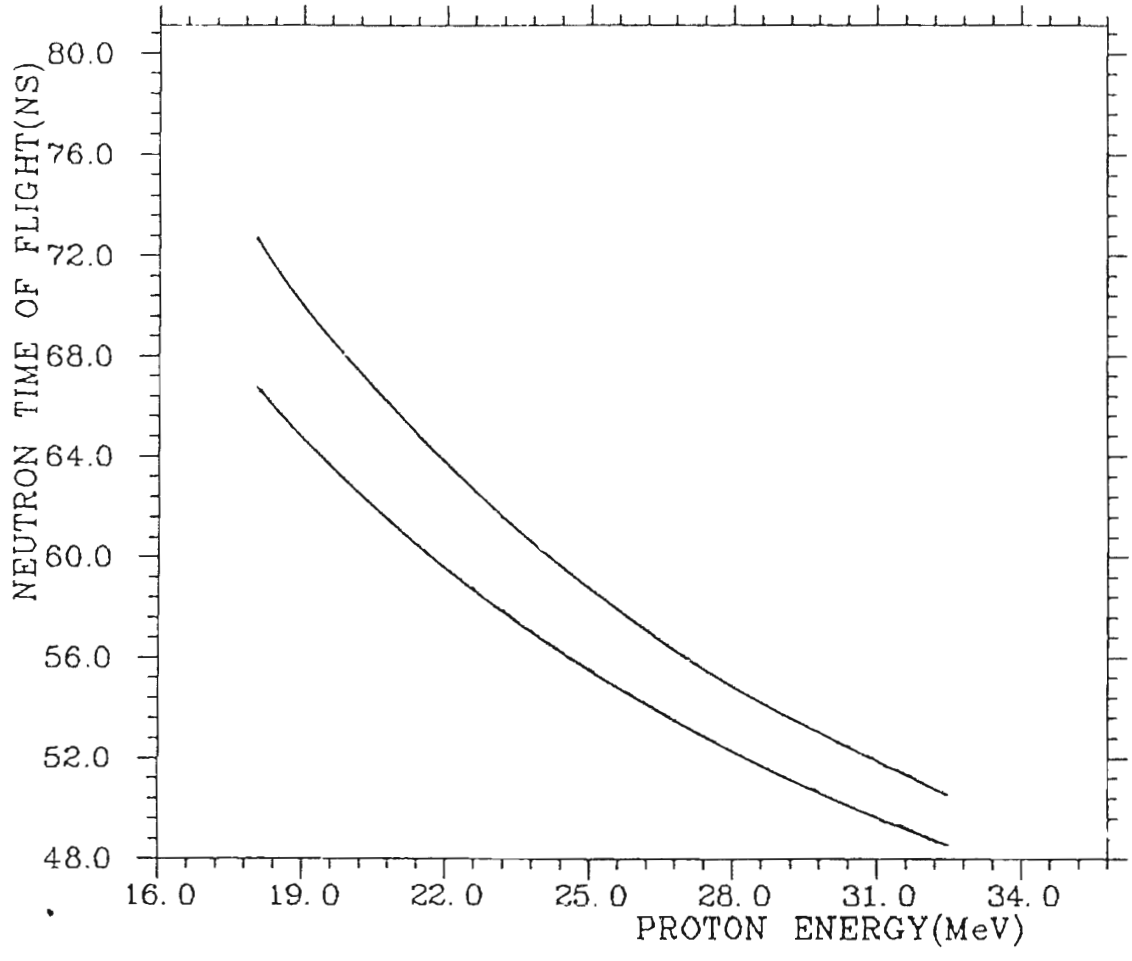

Fig. 2.5 Neutron time of flight from target to polarimeter. The lower curve represents the ground state neutron group produced at 40^0 lab, in the reaction $^{13}C(p,\vec{n})^{13}N$. The upper curve represents the first excited state from the same reaction.

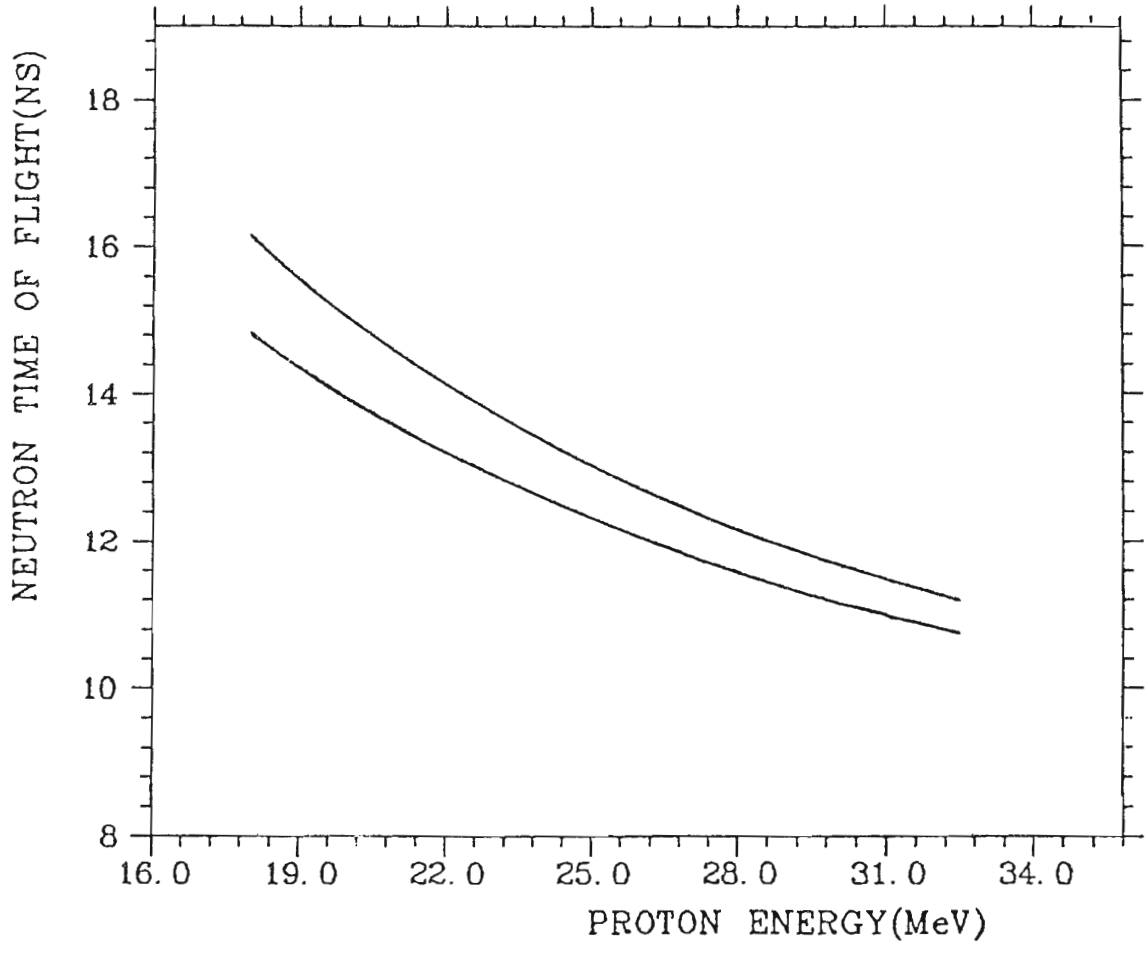

Fig. 2.6 Neutron time of flight from the polarimeter to the side detector (120°). The lower curve represents the ground state neutron group produced in the reaction $^{13}C(p,\vec{n})^{13}N$ and later scattered from the polarimeter to the side detector. The upper curve represents the neutron group from the first excited state produced in the same reaction. and for the same flight path.

detector. The time difference at 22MeV in this case is 0.84ns between the two neutron groups. At 30MeV this time difference decreased to 0.4ns. The total time difference at 22MeV will be 4.60ns from target to side detector.

Fig 2.7 Shows the time of flight from the ^{13}C target to the polarimeter. This time one can see the same two neutron groups from a previous beam burst(35ns earlier) in the lower left corner.

Fig 2.8 shows the energy resolution for the two neutron groups as a function of proton energy for the time of flight from the ^{13}C to the polarimeter. The higher the energy the lower the energy resolution and this is because at higher energy the time difference for a given flight path becomes smaller.

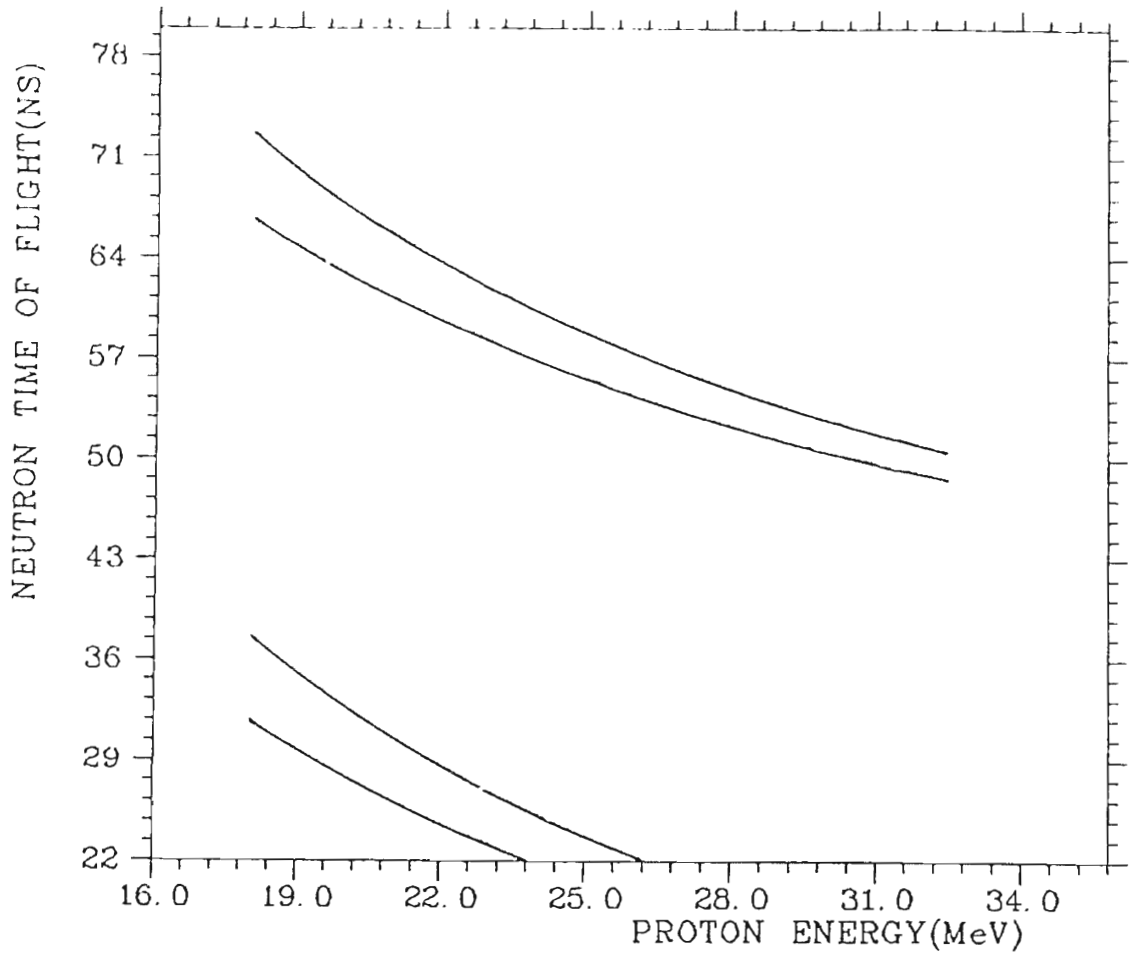

Fig. 2.7 Same as fig 2.6 but this time one can see the same two neutron groups from an earlier beam burst.

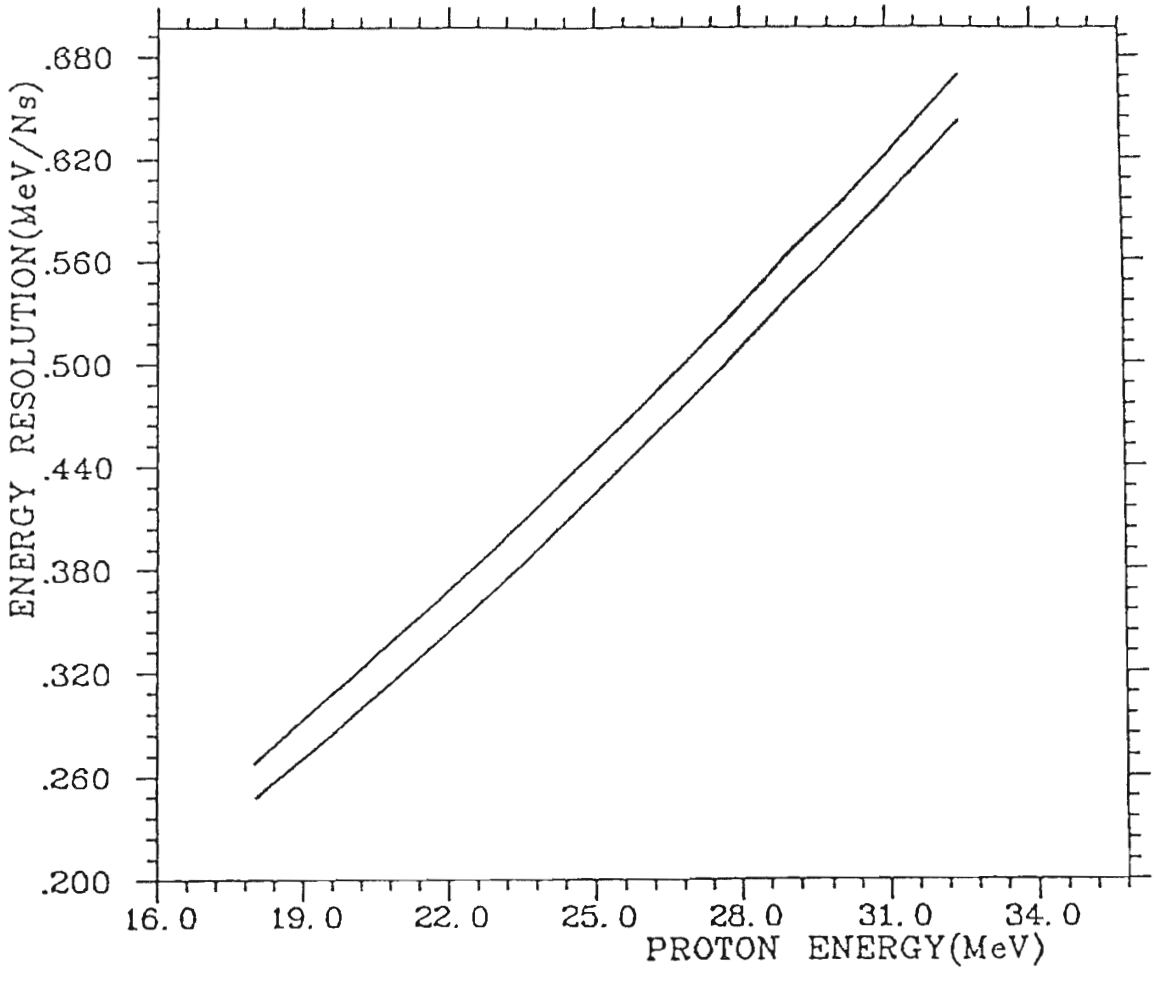

Fig. 2.8 Energy resolution as a function of proton energy for flight path of 3.5m (target to polarimeter).

Table 2.5

Parameters used during the experiment

a) Target: Carbon-13.

b) Distance from the carbon-13 target to the gas polarimeter 3.50m.

c) Distance from the detector to the gas polarimeter:0.53m.

d) Angle of the He polarimeter with respect to the proton beam line: 40 degrees

e) Angle of the side counters with respect to the gas polarimeter: 120 degrees.

f) shielding used: lead, steel, concrete.

g) magnetic shield: μ-metal

h) Neutron detector NE-213 liquid scintillator, end-on cylinder 11.43cm diameter and 12.7cm thick

2.5 INSTRUMENTATION

Block diagrams of the electronics used are shown in Figs 2.11 to 2.18. At the left of Fig 2.11 are shown the two NE-213 liquid scintillator detectors, chosen for their good n-Y pulse shape discrimination (PSD) properties.

The NE-213 is contained in a thin aluminum can with a glass window at one end. The inner surface of the can is coated with white reflector paint. The unit is fastened to the front face of a RCA-4522 14 stage photomultiplier with RTV-602[+] clear silicone rubber potting compound. This provides a bond that is removable yet strong enough to keep the rather heavy scintillator in place during use. The photomultiplier is operated in the grounded anode configuration. This permits the anode to be DC coupled and gives the best timing. It does, however, place the cathode at high voltage. To prevent adverse voltage gradients across the face of the photomultiplier, the aluminum can of the scintillator and the conducting coating of the photomultiplier are operated at cathode potential. The entire assembly is covered with an insulating sleeve and a high permeability magnetic shield.

+ General Electric, New York, U.S.A

2.5.1 PULSE SHAPE DISCRIMINATION (PSD)

This widely used method of discriminating between neutron and gamma-ray events in scintillators is based on the fact that organic scintillators have different scintillation responses for neutron and gamma rays. In particular, the variation of scintillation intensity with time has two (or more) components with different decay rates, of which the slow decay component is relatively more intense for neutrons than for gamma ray produced scintillations. To a good approximation the scintillation intensity from the scintillator can be represented by the expression (Br59)

$$I(t,E) \simeq A_f(E)\exp(-t/\tau_f) + A_s(E)\exp(-t/\tau_s)$$

where

$$\tau_f << \tau_s$$

$$A_f << A_s$$

A_f, and A_s are respectively, the light amplitudes of the fast and slow components at t=0 and t_f, t_s are the decay time constants for the fast and slow components respectively. and

$$\frac{[A_f/A_s]\text{electrons}}{[A_f/A_s]\text{Protons}} \simeq 2$$

The following possible explanation of this behaviour has been suggested by Brooks(Br59). An ionizing particle travelling through the

scintillator produces electronically excited M^* molecules and ionised molecules M^+. The excited molecules return to their ground state by (1) emitting a photon or (2) quenching, that is, conversion of their electronic excitation energy into vibrational energy. The ionised molecules recombine with electrons producing further electronically excited molecules M^*. The speed of this recombination process depends on the diffusion of electrons back to molecules and may be relatively slow ($\gtrsim 10^{-7}$ sec). This time is 1-2 orders of magnitude longer than the electronic de-excitation time, so it is reasonable to expect fast and slow decay components of the scintillation. The different amounts of fast and slow component for neutron and gamma ray produced scintillations might also be expected from the observation that, for a heavily ionising particle, the light output of an organic scintillator is not proportional to the incident energy and is less than would be expected from a linear light output versus energy relation. The idea arises from the fact that heavily ionising particles produce a higher concentration of quenching centers than do lightly ionising particles and, in consequence, they inhibit light output in a higher proportion than do lightly ionising particles, and so the quenching probability is greater in the first case than in the second. Neutron and gamma ray scintillations are produced largely by recoil of heavily ionising particles (mostly protons) and electrons, respectively. Thus, the fast component of neutron scintillations tends to be quenched to a greater degree than that due to gamma rays. However, 10^{-7} sec after the initial excitation when electron-ion

recombination is becoming an important process, excited molecules M^* are in a region of lower ionisation density than was the case for the primary M^* and scintillations are less strongly quenched. Therefore, although the scintillation intensity due to neutrons may be less than that due to gamma rays, the relative amount of slow decay component in neutron scintillations is greater than that in gamma ray scintillations.

2.5.1.1 THE ELECTRONICS FOR THE PULSE SHAPE DISCRIMINATION TECHNIQUE

Fast timing signals are derived from the anode of the photomultiplier by means of a constant fraction discriminator. The use of a constant fraction discriminator results in a minimum of timing walk over a wide range of pulse heights. These fast timing signals start two time to amplitude converters, labelled "TAC1" and "TAC2" (in fig 2.11), used to differentiate between neutron and gamma signals by means of pulse shape discrimination. The fact that scintillations induced in the liquid scintillator by neutrons have a longer slow component than those resulting from gammas means that the linear bipolar pulse from the spectroscopic amplifier produced by the neutron signal crosses zero at a later time than the pulse derived from a gamma signal. By starting the TAC on the initiation of an event (as indicated by the fast timing signal from the anode) and stopping it on the zero crossing of the linear signal (as determined by the single channel analyzer operated in crossover mode) one gets a spectrum

containing two distinct peaks, one corresponding to the detection of neutrons and the other corresponding to the detection of gammas.

The signal to stop the PSD-TAC , derived from the zero crossing of the bipolar linear pulse, has worse timing walk than the start signal which comes from the constant fraction discriminator on the anode. The result of this difference in walk is that the neutron and gamma peaks in the PSD spectrum tend to shift toward the origin for very low pulse heights. Hence, when accumulating a one dimensional PSD spectrum for a large number of events having a wide range of pulse heights, the neutron and gamma peaks tend to smear together and it is very difficult to separate them completely. Fig 2.9 is a one-dimensional representation of the PSD spectrum. The large peak to the left corresponds to the gammas and the small peak to the right represents the neutrons. We have removed most of the problems concerning this spectrum by using a two dimensional PSD versus pulse height representation.

In the PSD-pulse height (PH) plane (Fig 2.10) the signal appears as separated neutron and gamma "islands". The PSD-PH plane is displayed and loci are drawn around the neutron and gamma islands. These loci are then stored. The data analysis routine used during the experiment is then able to sort the incoming events into different single parameter spectra depending on whether they fall within the neutron or gamma loci.

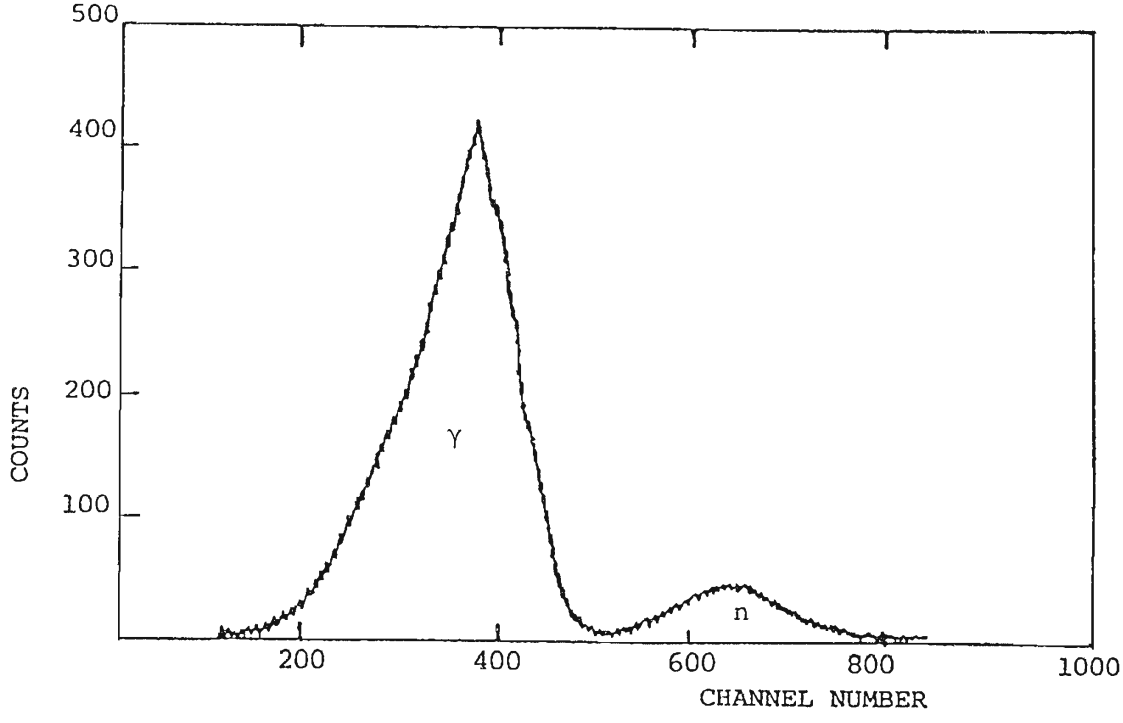

Fig. 2.9 One dimensional representation of the PSD spectrum. The large peak to the left corresponds to the gammas and the small peak to the right corresponds to neutrons.

Fig. 2.10 Two dimensional PSD versus pulse height representation. The top fig corresponds to the left detector and the bottom fig corresponds to the right detector.

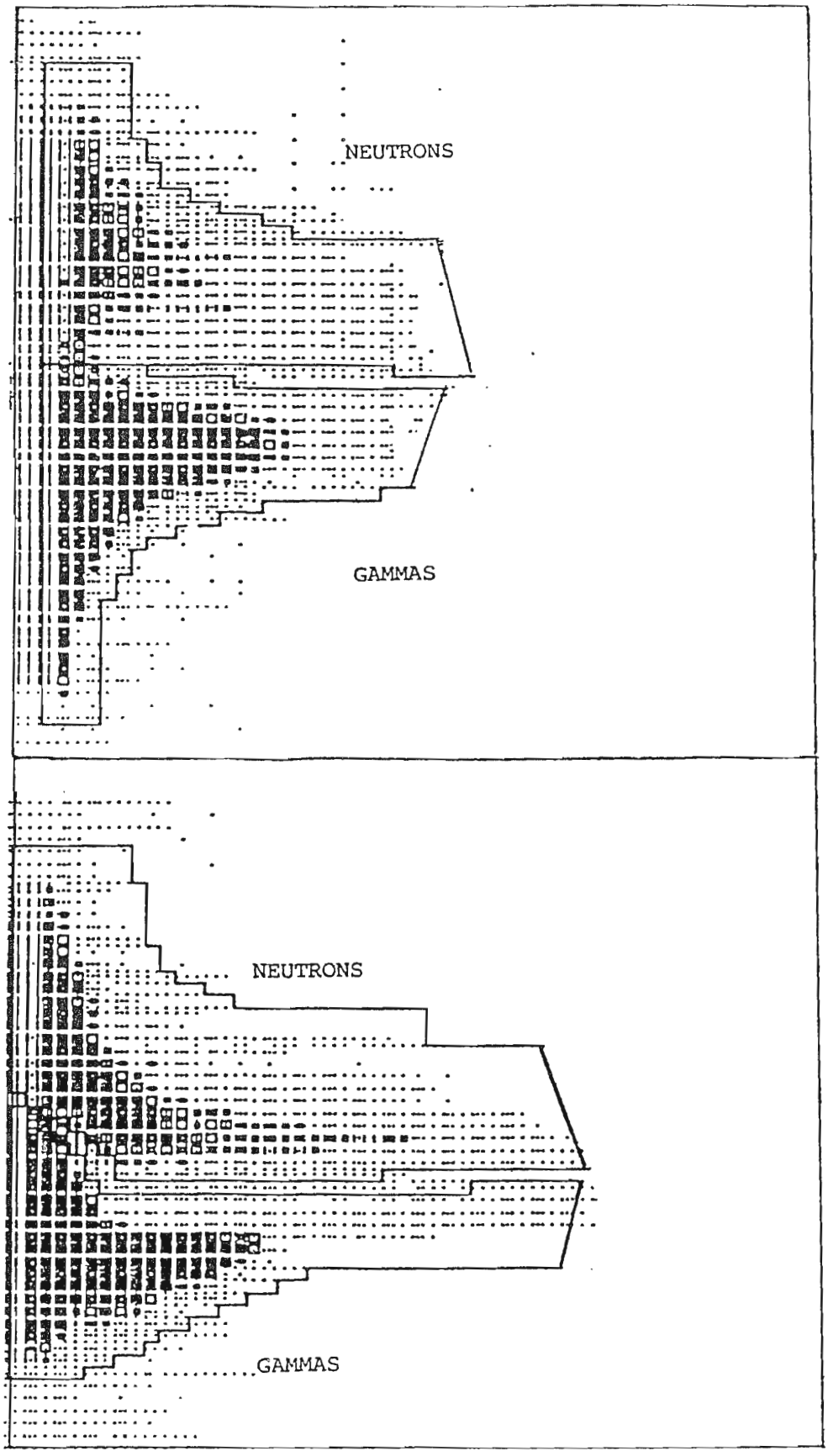
NEUTRONS
GAMMAS
NEUTRONS
GAMMAS

2.5.2 TIME OF FLIGHT

2.5.2.1 Time of flight from ^{13}C target to the gas polarimeter

The time of flight information from the neutron production source to the gas polarimeter was obtained by using the electronics shown in fig 2.12. The lower time to amplitude converter (labelled"TAC4") is started on the fast timing signal from the neutron polarimeter (this follows standard practice of starting on the signal having the lower count rate, hence reducing the number of false starts) and stopped on a signal derived from the machine RF (a small antenna fixed near to the cyclotron RF oscillator provides a waveform having the RF frequency, 28.48 MHz). A stop pulse is applied only every other RF period, which means every 70.2 ns. With the stop signal generated every other RF period, there will be two peaks in the TAC spectrum, one RF period (35.1 ns) apart. Since the machine period is accurately known, this provides a built-in time calibration. The delay in the stop channel is adjustable and serves to position the time of flight spectrum within the 100ns range of the TAC.

2.5.2.2 Time of Flight from The Gas Polarimeter To The Side Detectors

In this case the fast timing signals from the two neutron detectors are mixed and used to start the TAC labelled "TAC3"(fig 2.11). The stop signal is derived from the anode of the polarimeter (delay is introduced into the stop channel as required to place the desired

coincidence within the range of the TAC). Of all the neutrons scattered into the detectors only a certain number of them correspond to neutrons scattered from the polarimeter. These "true" events can be identified by their time relation to the scintillation in the polarimeter. If, for example, a scattered neutron is known to take τ ns to travel from the polarimeter to the side detector, then any detector pulse corresponding to a legitimate event will be preceded by a helium scintillation ocurring τ ns earlier. TAC3 establishes this time relation.

Table 2.6

Electronics for the experiment

Modules are standard NIM units

A = Amplifier

ADC = Analog to digital converter

CFD = Constant fraction discriminator

COINC = Universal coincidence unit

D = Discriminator

DA = Delay amplifier

DD = Dual discriminator

DSI = Dual sum and inverter

GDG = Gate and delay generator

LGS = Linear gate and stretcher

MCA = Multi channel analyzer

PA = Charge sensitive (integrating) preamplifier

QD = Quad. 100MHz discriminator

RM = Ratemeter

SA = Shaping spectroscopy amplifier

SC = Scaler

TA = Timing amplifier

TAC = Time to amplitude converter

TFA = Timing filter amplifier

TSCA = Timing single channel analizer

Fig. 2.11 Electronics used during the experiment, PSD (left and right), TOF (polarimeter to side detector) and PH (left and right detectors).

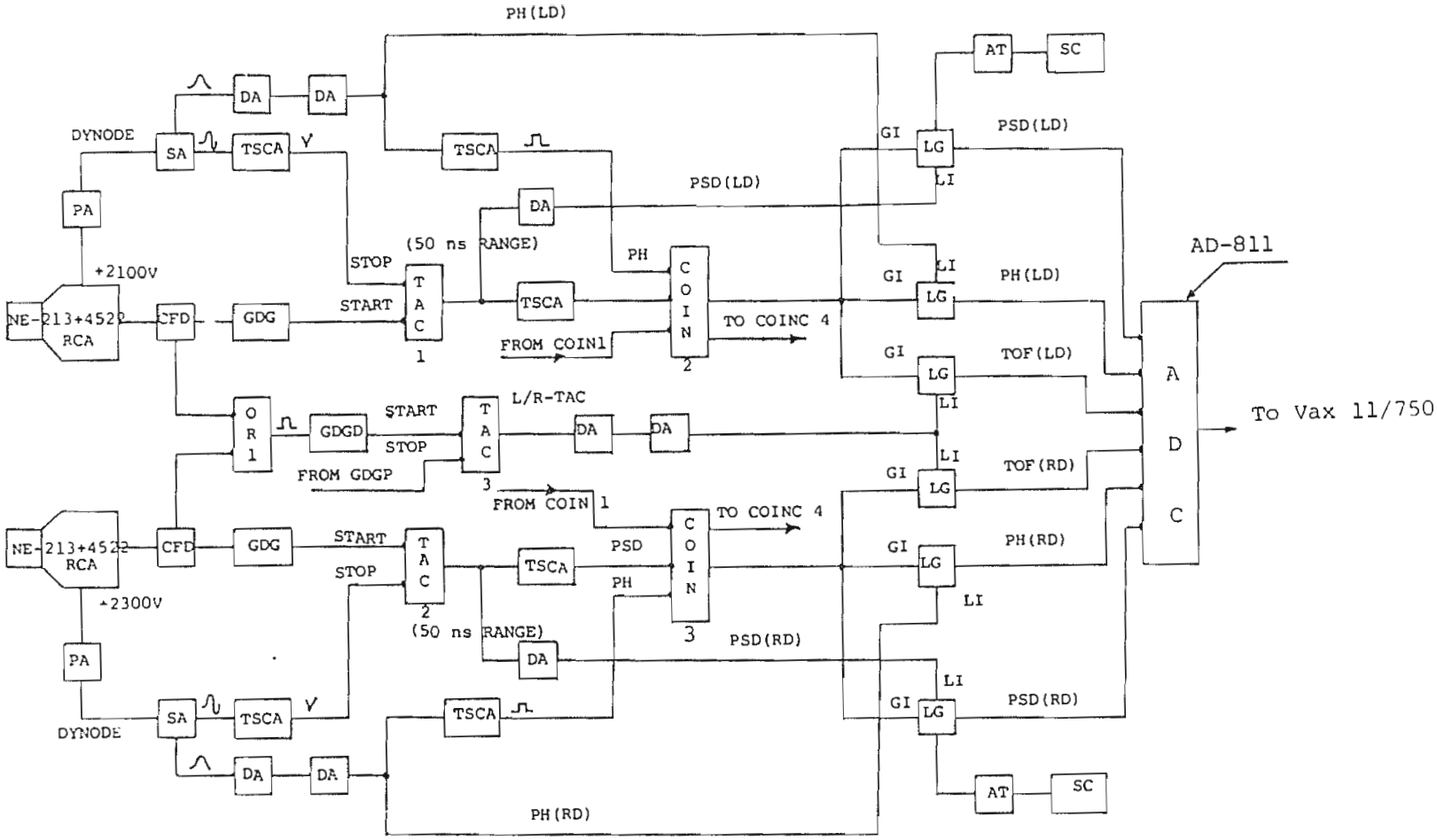
PH(LD)
DA
DA
AT
SC
DYNODE
SA
TSCA
V
TSCA
GI
LG
PSD(LD)
LI
PA
DA
PSD(LD)
(50 ns RANGE)
STOP
PH
AD-811
+2100V
GI
LI
PH(LD)
NE-213+4522
RCA
CFD
GDG
START
T
A
C
1
TSCA
C
O
I
N
2
TO COINC 4
FROM COIN1
GI
LG
TOF(LD)
LI
O
R
1
GDGD
START
T
A
C
L/R-TAC
DA
DA
A
D
C
To Vax 11/750
STOP
FROM GDGP
3
GI
LG
TOF(RD)
FROM COIN 1
TO COINC 4
NE-213+4522
RCA
CFD
GDG
START
T
A
C
PSD
C
O
I
N
GI
LG
PH(RD)
STOP
TSCA
PH
LI
+2300V
2
(50 ns RANGE)
3
PSD(RD)
PA
DA
LI
DYNODE
SA
TSCA
V
TSCA
GI
LG
PSD(RD)
DA
DA
AT
SC
PH(RD)

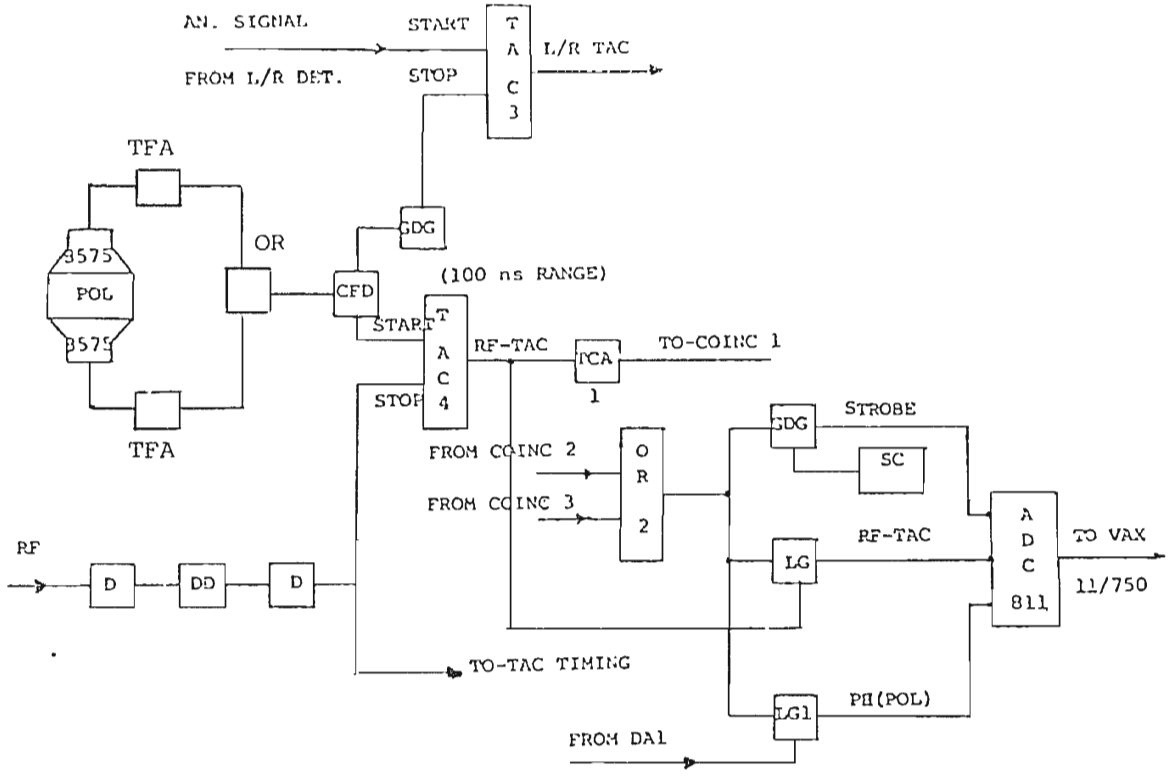

Fig 2.12 Electronics for the time of flight from the carbon target to the Polarimeter.

Fig. 2.13 Electronics used to extract pulse height information (top fig.)

Fig. 2.14 Electronics used to extract the time structure information.

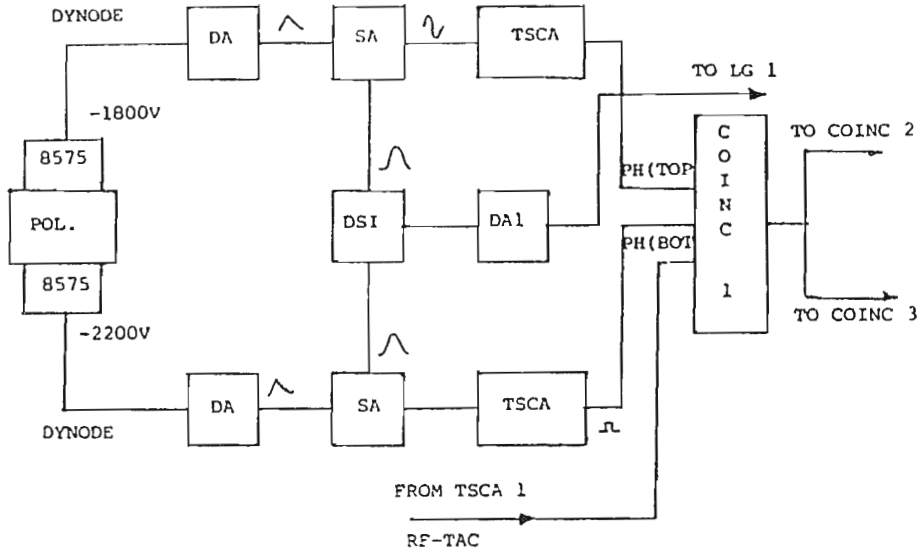
DYNODE
DA
SA
TSCA
TO LG 1
-1800V
8575
POL.
8575
DSI
DA1
PH(TOP
PH(BOT
C O I N C 1
TO COINC 2
TO COINC 3
-2200V
DYNODE
DA
SA
TSCA
FROM TSCA 1
RF-TAC

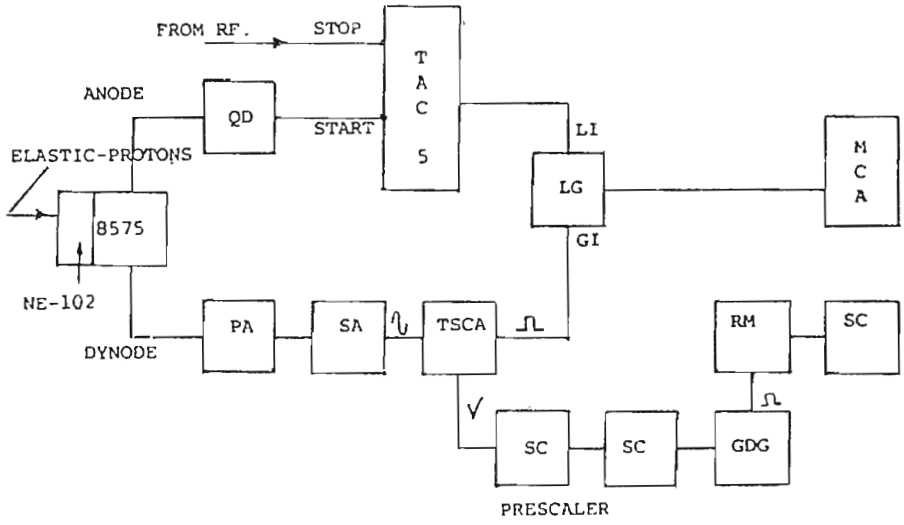
FROM RF.
STOP
T A C 5
ANODE
QD
START
LI
M C A
ELASTIC-PROTONS
LG
8575
GI
NE-102
DYNODE
PA
SA
TSCA
RM
SC
SC
SC
GDG
PRESCALER

Fig. 2.15 Electronics used during the second part of the experiment.

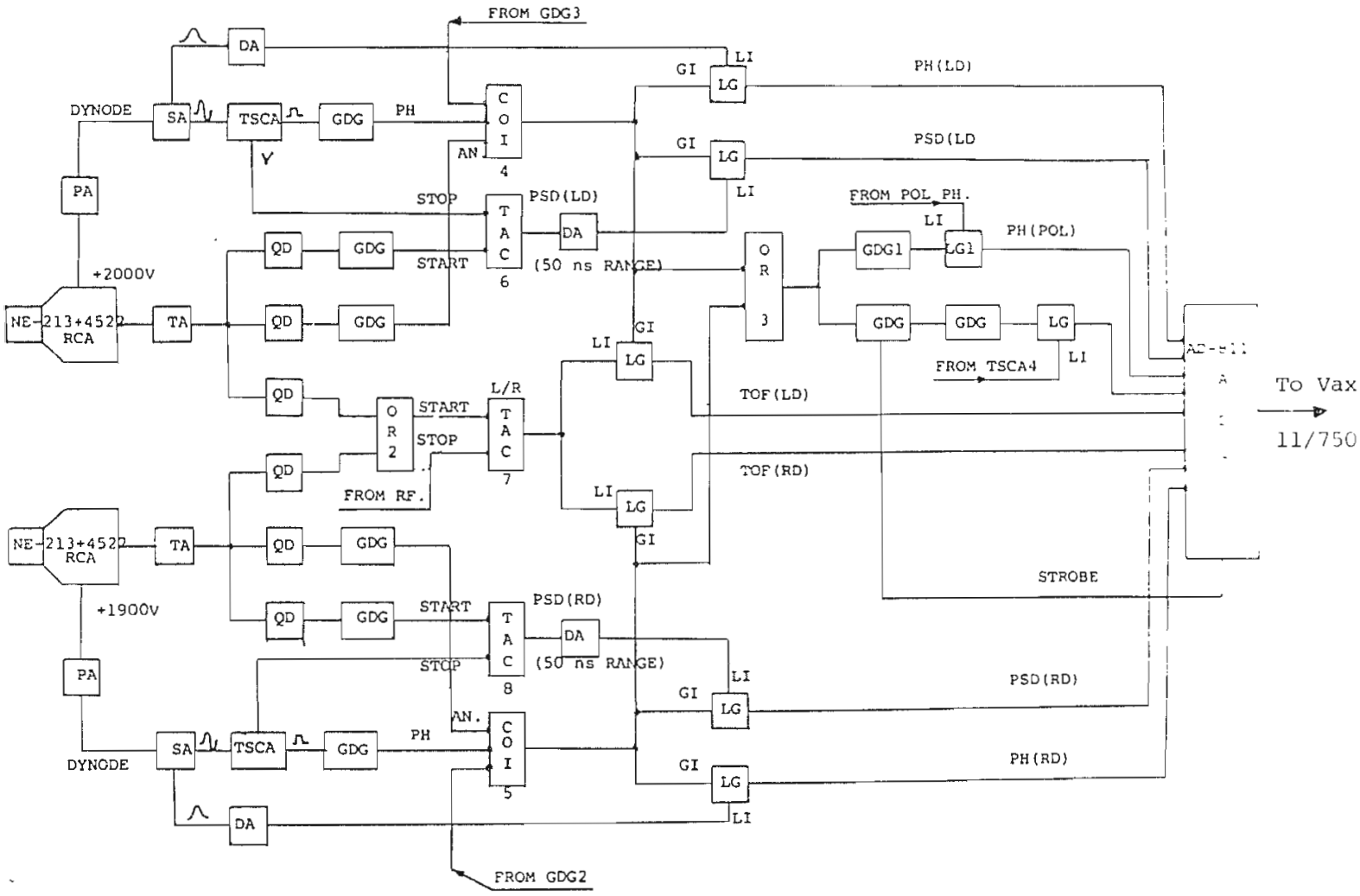
FROM GDG3
DA
DYNODE
SA
TSCA
GDG
PH
COI
4
AN
Y
PA
STOP
PSD(LD)
TAC
6
DA
(50 ns RANGE)
QD
GDG
START
+2000V
NE-213+4522
RCA
TA
QD
GDG
QD
OR
2
START
STOP
L/R
TAC
7
FROM RF.
QD
NE-213+4522
RCA
TA
QD
GDG
+1900V
QD
GDG
START
PSD(RD)
TAC
8
DA
(50 ns RANGE)
STOP
PA
AN.
DYNODE
SA
TSCA
GDG
PH
COI
5
DA
FROM GDG2
GI
LI
LG
PH(LD)
GI
LG
PSD(LD
LI
FROM POL PH.
LI
PH(POL)
OR
3
GDG1
LG1
GDG
GDG
LG
LI
FROM TSCA4
GI
LI
LG
TOF(LD)
TOF(RD)
LI
LG
GI
STROBE
GI
LI
LG
PSD(RD)
GI
LG
PH(RD)
LI
To Vax
11/750

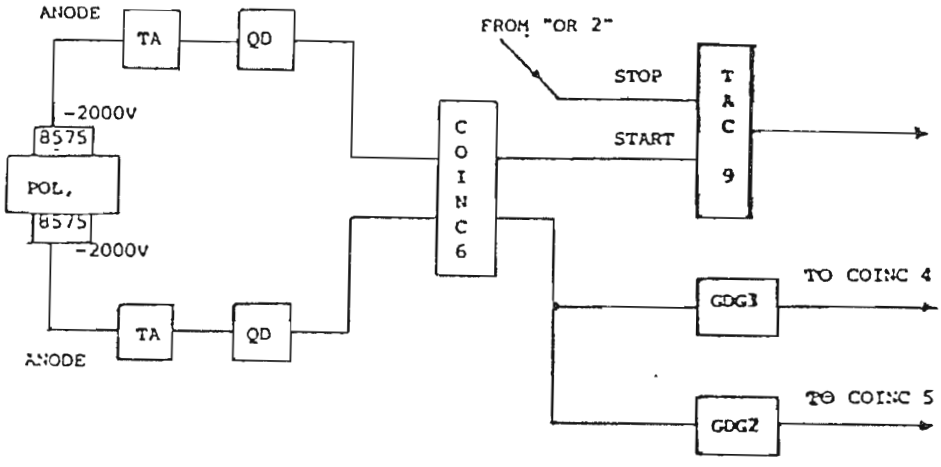

Fig. 2.16 Electronics for the TOF from the polarimeter to the side detector.

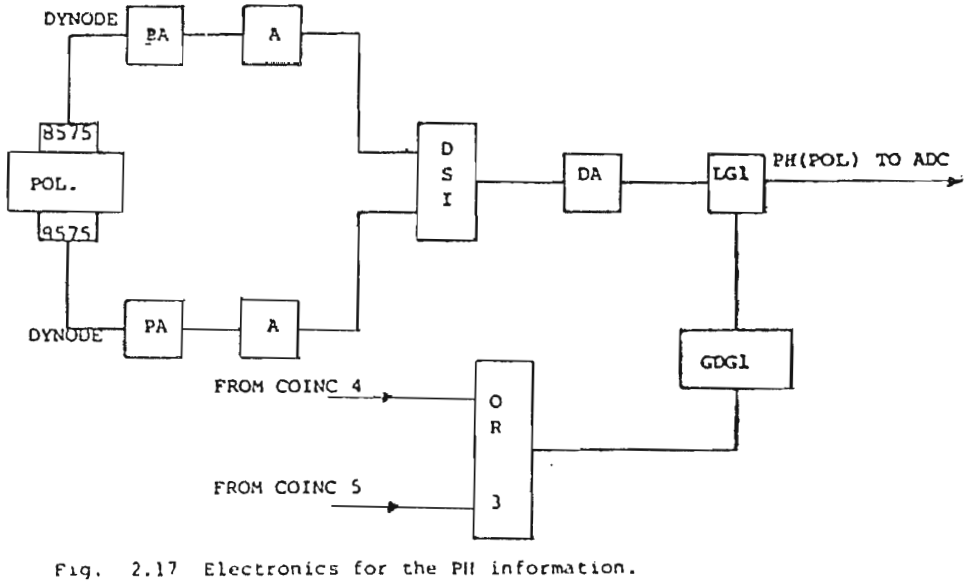

Fig. 2.17 Electronics for the PH information.

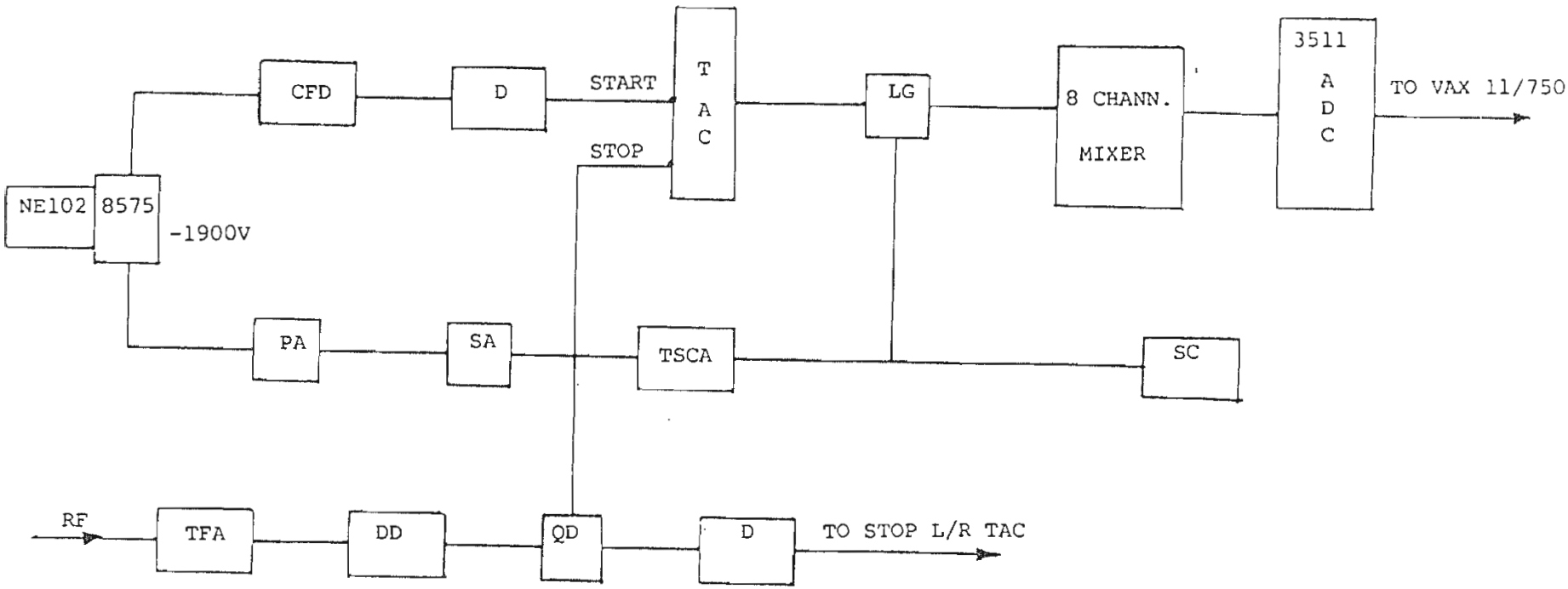

Fig. 2.18 Electronics for the time Structure arrangement.

2.5.3 PULSE HEIGHT INFORMATION

2.5.3.1 Pulse Height From The Polarimeter

Fig 2.13 is a diagram of the electronics used to extract the pulse height information from the polarimeter. The linear signal from top and bottom phototubes are amplified and fed into a Dual Sum and Inverter and from here they are passed to a linear gate and then to the ADC and to the Vax-11/750 computer. The scintillations produced in the polarimeter by the neutrons and gammas from the ^{13}C target are viewed by an RCA-8575 photomultiplier at either end of the polarimeter. A coincidence condition was set between the linear signal from the top phototube, the linear signal from the bottom phototube and the signal corresponding to the time of flight from the ^{13}C to the polarimeter. This coincidence has two functions.

1. to reduce the effect of noise produced by the phototubes.
2. to ensure the events induced in the polarimeter are caused only by neutrons produced in the target.

2.5.3.2 Pulse Height In The Side Detectors.

Pulse height information from the side detectors is derived by taking a linear signal from an earlier stage (dynode 9) of the photomultiplier. Linear pulses from the phototube used with the NE-213 are amplified by a charge sensitive preamplifier and shaped by a spectroscopy amplifier. The resulting bipolar pulse is used in the PSD circuit. Ideally, the

events detected by the two side counters should correspond to events that have truly been produced in the helium polarimeter, and are not a part of the room background. To achieve this in practice a second coincidence requirement has been set between the signal from "COINCIDENCE1", the linear signal corresponding to the Pulse Height (PH) of the side detector, and the Pulse Shape Discrimination signal (PSD) (this is done in the left channel as well as in the right). These coincidence signals are labelled "COINCIDENCE2" AND "COINCIDENCE3" (fig 2.11) and are used to open the linear gates that transfer the signals to the ADC. After appropriate delays the signals are converted to digital form and transferred to the Vax 11/750 computer. A scaler counts the total number of strobes on the CAMAC ADC. Comparing this number to the total number of events actually recorded by the computer permits us to correct for deadtime. The signals from COINC2 and COINC3 are used by means of unit "OR4" to open the linear gates that are passing the time of flight signal RF-TAC and the helium pulse height (PH).

2.5.4 The Time Structure

The time structure information was obtained by using the circuit shown in Fig 2.14. The fast timing signal from the RCA-8575 photomultiplier derived using the quadruple discriminator is used to start a time to amplitude converter(TAC5). This TAC is stopped on the signal taken from the machine RF. Thus a time spectrum for protons

scattered elastically from the target is accumulated by a multi channel analyzer. This time spectrum shows both the burst width and phase (relative to the RF) of the beam on target. An on-line FORTRAN routine is used to calculate the centroid and FWHM of the peak. This information is used to improve the timing resolution of the beam by

1. manually adjusting the RF amplitude and,

2. compensating for beam phase drift, i.e, shift in the centroid. The method used is based on the observation that the beam phase is very sensitive to small changes in the cyclotron's main magnetic field. This sensitivity is a common feature of cyclotrons, and is presumably due to accumulated phase slip over many orbits for a small change in the cyclotron resonance conditions. The effect is much larger than the change in the transit time between the cyclotron and the target due to small shifts in the beam energy when the main magnet field is changed slightly.

The average resolution at FWHM was kept at 0.9ns during the experiment.

The arrangement of electronics produced a set of eight different raw spectra containing all the information needed to calculate the polarization via the left right asymmetry.

Further online and offline analysis was necessary to fully extract the neutron yield necessary for the asymmetry calculation.

2.5.5 RUN AT 31.8 MeV

Fig 2.15 shows the main part of the electronics used during the run at 31.8 MeV.

2.5.5.1 TIME OF FLIGHT INFORMATION

2.5.5.2 Time Of Flight From The ^{13}C Target To The Polarimeter

The RF-TAC("TAC9") shown in Fig 2.16 was started on the signal derived from the coincidence between the top and bottom phototubes, and stopped on the signal from the coincidence between the fast signal of the side detectors. In consequence, we no longer have time of flight from the ^{13}C target to the polarimeter. The measured time of flight is now from the ^{13}C target to the polarimeter and from the polarimeter to the side detectors.

2.5.5.3 Time Of Flight From The Polarimeter To The Side Detectors

The time of flight in this case is recorded by the TAC labelled (L/R-TAC9), left and right TAC. It is started on the signal derived from the coincidence between the fast signals of the two side detectors and stopped on the signal derived from the machine RF. The TAC output passes to two linear gates in order to be transferred to the computer.

As before the TACs labelled this time "TAC6"and "TAC8"(fig 2.15) are used to differentiate between neutrons and gammas by mean of pulse shape discrimination. Both are started on the fast

timing signal derived from a NIM model 821 QUAD 100 MHz discriminator and stopped on the signal from the TSCA which gives the time of the zero crossing of the linear signal. The anode, the PH signal from the side detector and the anode signal from the polarimeter are brought into coincidence in both channels("COINC4" and "COINC5"), and this coincidence signal is used to open the linear gates that are passing the PH, PSD and TAC signals to the ADC. These signals are then digitised to be transferred to the computer. This of course is done in both channels.

The Pulse Height information Fig 2.17 was obtained in the same manner as in the first part.

The time structure signal was obtained in a similar way, Fig 2.18 but, this time we used the Vax computer instead of the MCA. The overall timing resolution this time was around 1.07ns FWHM (Fig. 2.19) with a best value of 0.77ns FWHM.

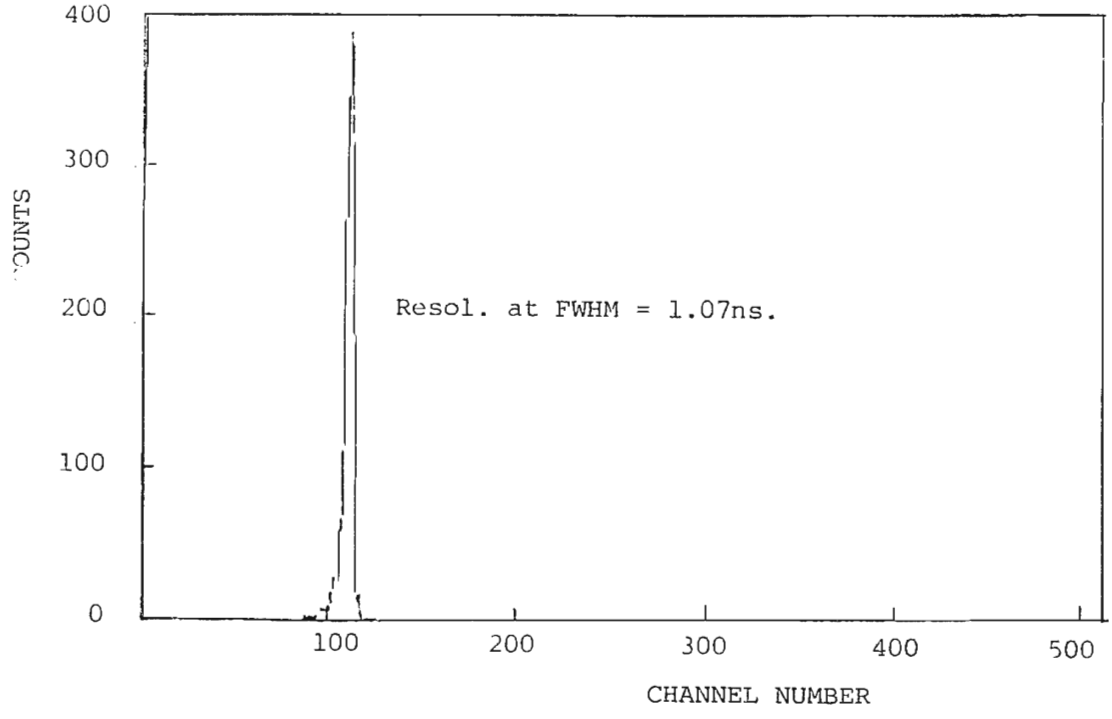

Fig. 2.19 Time structure of the beam during the experiment. resolution is 1.07ns at FWHM.

2.6 THE GAS POLARIMETER

2.6.1 INTRODUCTION

When ionizing particles traverse matter, they lose their kinetic energy by electromagnetic interactions with the atomic electrons, resulting in the excitation and ionization of the atoms. In the deexcitation and recombination processes following the interaction, photons are emitted. One therefore expects scintillation phenomena in gases due to the passage of ionizing particles. The first successful observation of gas scintillations using a photomultiplier was reported by Grun and Schopper (Gr51). Other instruments of this type using inert gas scintillators have been described by Eggler and Huddleston(Eg54,56), Segre and Wiegang(Se53), Boicourt and Brolley(Bo54), Villaire and Wouters(Vi55), Nobles et al(No55), Nobles(No56), Northrop and Nobles(No56a,56b), Palevsky et al(Pa56), Forte(Fo56), Sayres and Wu(Sa57), Koch and Lesueur(Ko58), Hentschel et al(He67), Morgan and Walter(Mo68), Manduchi et al(Ma69), Davie and Galloway(Da71), Tornow(To73), Drigo et al(Dr79) and others. Further developments established the fact that the pulses have a fast rise time and the pulse heights are a linear function of energy.

The light emitted during the de-excitation and recombination processes has a distinctly different optical spectrum for different gases, and each spectrum covers a wide range of frequencies. On the other hand, the photocathode of a photomultiplier is sensitive

only to a very narrow range of wavelengths. To fully utilize the photons emitted from the de-excitation and recombination processes, one must convert as efficiently as possible the photons of short wavelength to the appropriate frequency region to suit the photocathode. This is done by using a wavelength shifter (generally an organic substance e.g., diphenylstilbene), which absorbs the light produced in the ultra violet region (162nm in the case of helium) and reemits it in the visible region where most photomultipliers are sensitive.

It is well known that the scintillation property of a gas is very sensitive to impurities(Ko60a,b). A small amount of contaminant, such as oxygen or other polyatomic gases, may completely quench its useful scintillation properties.

In the early gas scintillators the energy signal was position dependent; tracks of equal energy loss occurring in different parts of the scintillation volume did not produce pulses of the same height because of absorption of light on the reflecting surfaces surrounding the gas volume. Moreover, they were designed with only one light window, so the poor transport of light within the scintillator to the cathode of the photomultiplier produced a low energy resolution. G.Hentschel et al(He67) designed a scintillator cylindrical in shape, capable of standing high pressure and equipped with light windows on both ends. This scintillator has the advantage that if the pulse heights from the two phototubes are added, then with a suitable adjustment of the photomultiplier gain the output pulses become independent of the position of the scintillation event in the

scintillator and the pulse height is doubled compared to the arrangement with a single window and phototube. In this fashion the energy resolution of the system is improved over the old design.

Because of these advantages, we decided to build a gas polarimeter incorporating the features mentioned.

2.6.2 THE NEUTRON GAS POLARIMETER

The basic structure of the neutron gas polarimeter described in this thesis is shown in Fig 2.20. The He gas used as the analyzer is contained in a high pressure gas chamber. Scintillations from the He recoils are viewed by two photomultipliers which provide the electronic signal for the recoil energy measurement and timing.

The gas chamber was machined from a solid piece of stainless steel type 304. The shape of the gas volume is a cylinder 5cm in diameter and 15cm long with walls 0.2cm thick. The ends of the cylinder are sealed with two acrylic windows depicted in fig 2.21, which are mounted over a teflon ring, and a Viton "O ring"; the first, to avoid damage to the windows, and the second to get a proper high pressure seal. The windows are kept in place by two heavy stainless steel flanges bolted to the main body of the cylinder by 15 bolts, 0.63cm in diameter. This kind of seal has proved to be strong enough to hold a pressure of 16000 KPa in the cylinder.

Two 5.08cm diameter RCA- 8575 photomultipliers, bonded to the face of the acrylic windows with RTV-602 clear silicone rubber

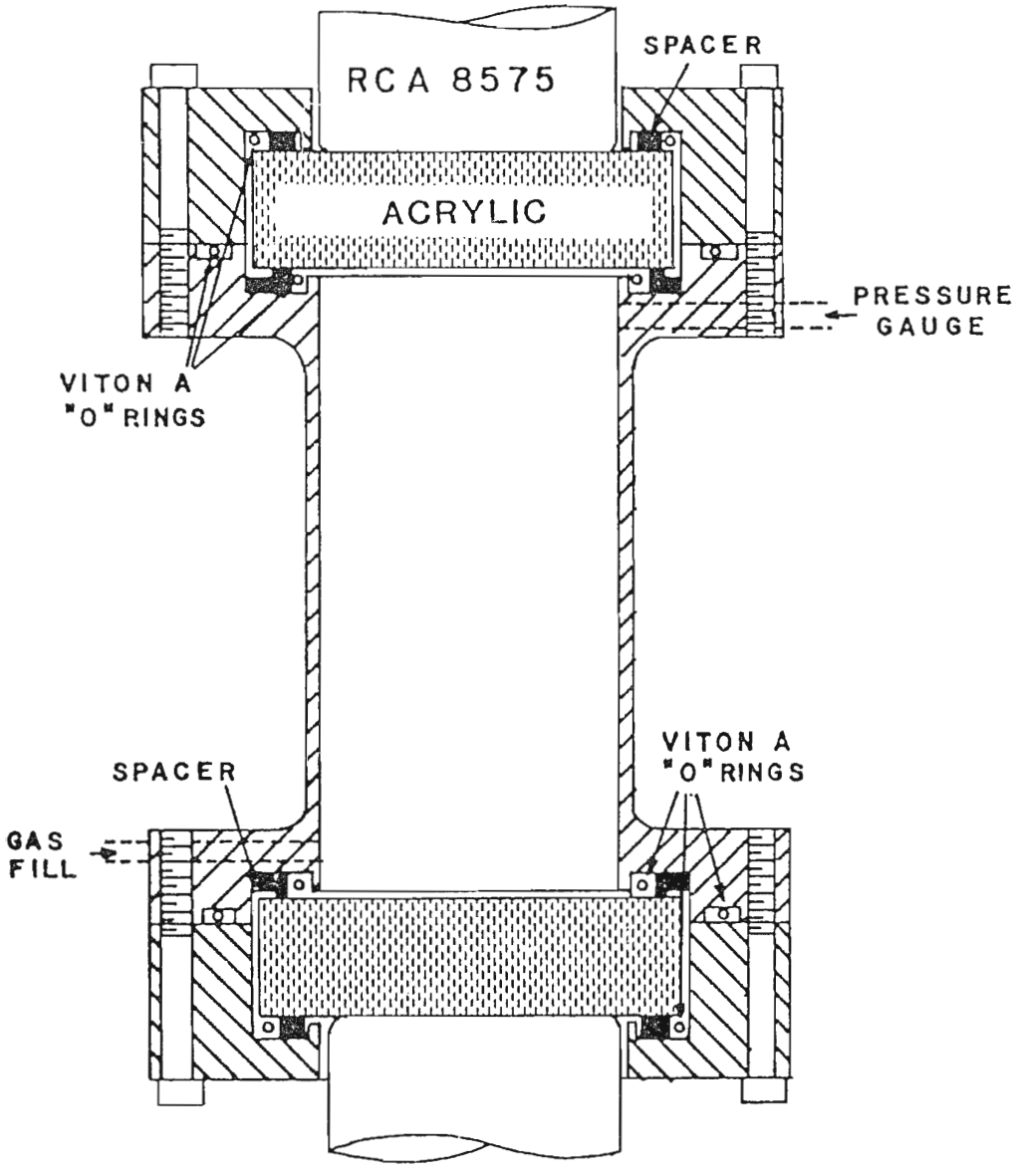

Fig. 2.20 Cross-Section of the Gas Polarimeter

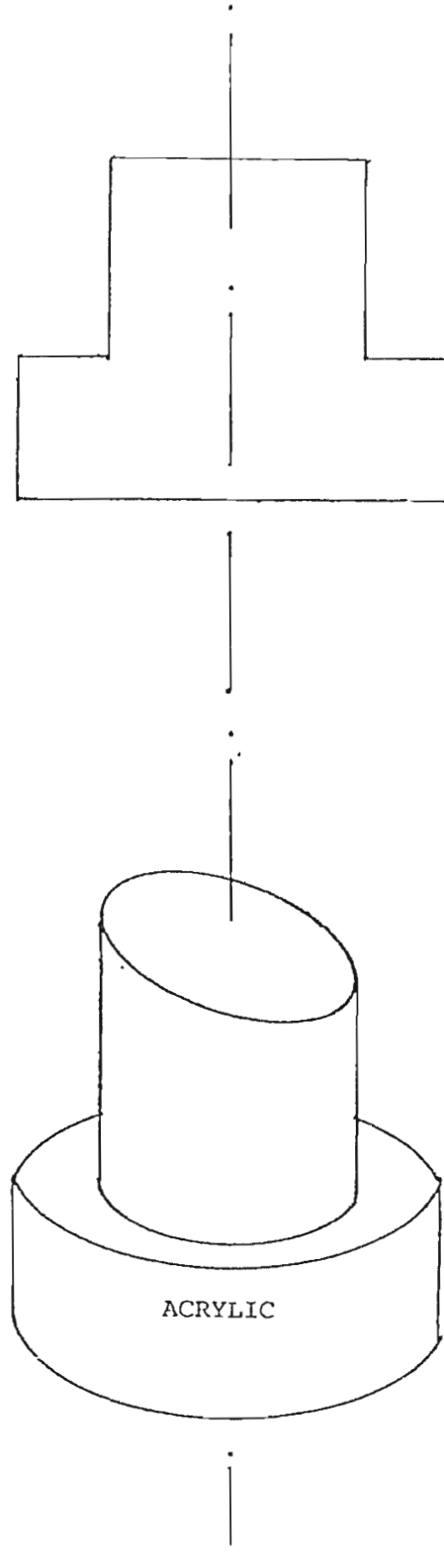

Fig. 2.21 Cross-Section of the Acrylic Window

potting compound, view the gas scintillations through the windows.

2.6.2.1 THE FILLING AND VENTING SYSTEM

Fig 2.22 is a diagram of the filling and venting lines. This system was constructed from 0.95cm OD stainless steel pipes and fittings. The fact that the cylinder can be raised to a high pressure imposes certain safety constraints on how the system should be handled. The filling and venting valves to the system are operated by remote control. Furthermore, after the cylinder has been pressurized it is isolated from the rest of the system to minimize the danger incurred by gas leaking through the bottle valve. This is achieved by inserting a third, remote controlled valve in the helium line, labelled "SV"(Safety Valve) in fig 2.22. The filling and venting of the system was done very slowly to avoid sudden stresses on the cylinder. The "SV" was provided with a fast electric motor so it could be closed very quickly if necessary. The xenon line was completely manually controlled. Xenon is added to the helium to improve light output. The amount of xenon was always 10% of the total amount of helium(No58), so that the xenon pressure was never higher than 3700 KPa. We considered there was no need for the use of remote controlled regulators in this case. To avoid any damage to the low pressure xenon regulator, an extra high pressure valve was installed in this line, so once the cylinder was filled with the required amount of xenon, this valve was closed. If for any reason it is not possible to close the helium valve from the

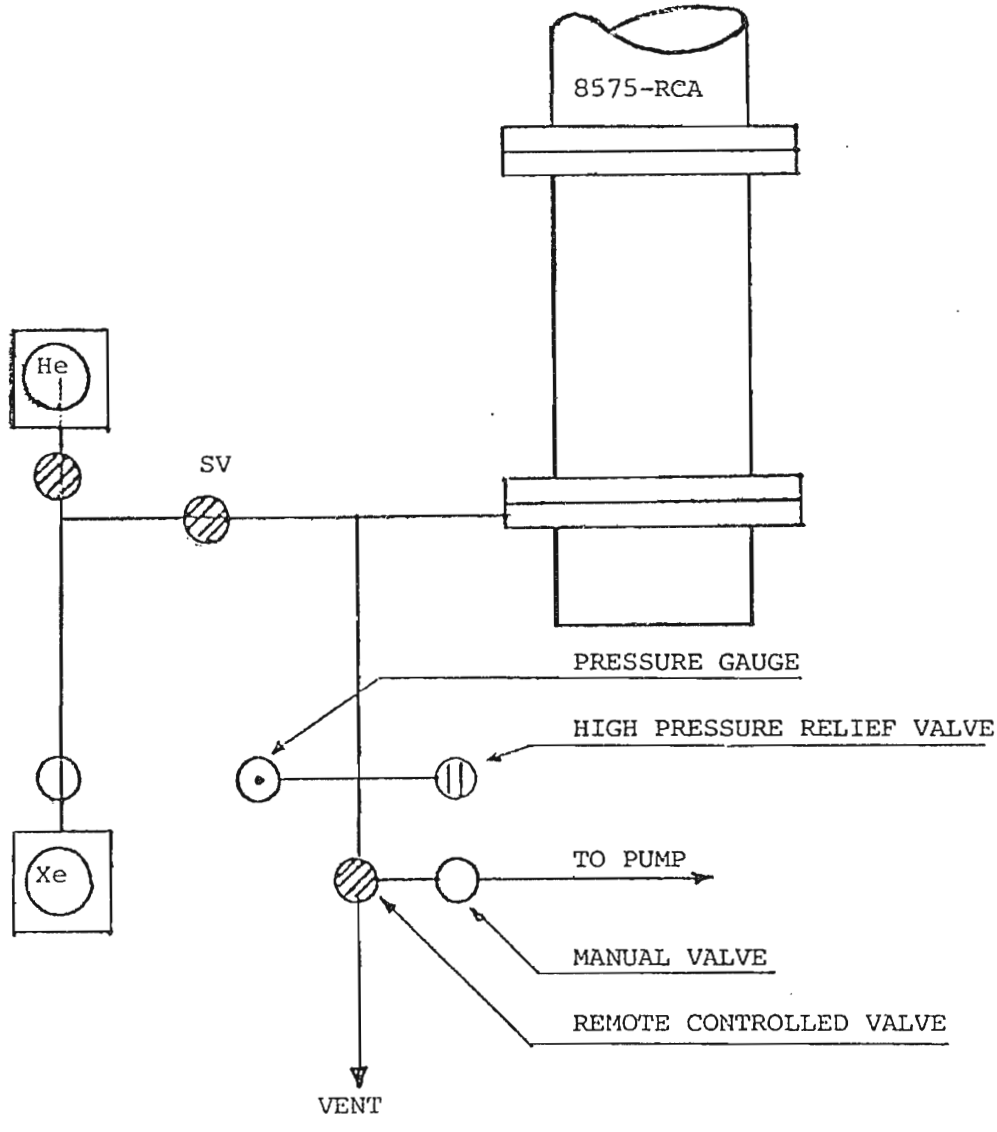

Fig. 2.22 Schematic diagram of the filling and venting system of the polarimeter.

tank when the pressure has reached the required value the system does not suffer any damage as an extra high pressure relief valve, set at the factory at 16400 KPa, has been installed in the helium line.

The pressure was monitored at all times by means of closed circuit television. Two TV cameras were used, one on top of the helium tank to check the pressure while the system was being filled, and the other in front of the pressure gauge located about ten centimeters from the gas chamber.

Since the amount of light from the He recoils is strongly dependent on the purity of the He-Xe mixture(No58), it is very important to have a xenon-helium mixture of high purity. This was achieved by connecting the system to roughing and diffusion pumps. The roughing pump evacuated the chamber to about 7.0 Pa (50militorr) and was then closed. Helium was admitted to about 1400 KPa (around 200psi) and allowed to settle for a few minutes before being let out to atmospheric pressure. The system was then roughed down to 7.0 Pa again and the procedure repeated. After three or four such flushings with helium, the diffusion pump was turned on and the system pumped down to a pressure of 3.0×10^{-6}KPa for a few days. This method of cleaning the gas chamber proved to be adequate. Whenever the gas chamber was filled without following this procedure, we simply could not observe scintillations in the polarimeter.

Once the gas chamber and the system was free of contaminants, the xenon gas was admitted to a pressure of 1030KPa, and then helium was added to bring the total pressure to 10300KPa. With

this method the gases were quite well mixed by the large flow of gas during the addition of the helium. If the order of filling had been reversed it would have required several hours to achieve a uniform He-Xe mixture in the gas chamber(Ha67). Since xenon comprises only 10% of the total, there will be a very small flow of gas into the chamber during the xenon addition and most of the Xe will remain near the bottom where the entrance to the chamber is located.

2.6.3 LIGHT COLLECTION

When an energetic He nucleus is stopped in the high pressure He-Xe gas chamber its energy goes into ionizing and exciting the atoms in the gas, and some of the kinetic energy of the He ends up as light. Since the statistical variation of the photomultiplier output depends on the number of photons incident on the photocathode, good light collection is necessary to obtain good resolution of the He recoil energy. The object of the light collection system is to get the maximum amount of such light to the two photomultipliers which view the gas scintillations through the acrylic windows. Helium in the gaseous state has been used as an analyzer for many years and in order to increase its stopping power different inert gases (Ne, Ar, Kr, Xe) have been added to the helium. The light output has been found to be a maximum for a mixture of 90% He and 10% Xe(N058). It is important to keep this in mind, otherwise one could be tempted to increase the amount of xenon in order to increase the stopping power of the mixture, or even use only xenon. However, there are two facts which should be

taken in account:

1. The analyzing power for the reaction $^4He(\vec{n},n)^4He$ is well known and the analyzing power for the reaction $Xe(\vec{n},n)Xe$ is not.

2. The energy transferred from a neutron to a ^4He nucleus is greater than the energy transferred from a neutron to a Xe nucleus(from kinematics, see table 2.7 below), so the pulse height for neutron scattering would be smaller for Xe.

Table 2.7

Energy Inc	Helium Gas		Xenon Gas	
Neutron MeV	E MeV	E MeV	E MeV	E MeV
19.38	8.81	10.49	18.93	0.44
22.85	10.46	12.38	22.32	0.53
27.31	12.48	14.82	26.67	0.63

This table has been calculated for a scattering angle from the polarimeter equal to 120^0.

An important element in obtaining good light collection is to make the walls of the chamber as reflective as possible. This is done by painting the inside walls of the cylinder with a diffuse reflector paint. On top of this paint the wavelength shifter is

deposited. The diffuse reflecting paint is, of course, essential, otherwise the size of the signal from the photomultiplier for equal scintillations in the cylinder will depend on position. Another consideration affecting this coat of reflecting paint is the rise time of the light pulse which stimulates the cathode of the photomultiplier. This should be as short as possible to reduce the background in the experiment. If the reflectivity of the cylinder were 100%, light could be reflected many times before entering the acrylic windows and then being transmitted to the photomultiplier, and this would adversely affect the rise-time of the pulse. Thus a compromise has to be reached between high reflectivity with good resolution and low reflectivity with good timing characteristics. The reflector paint, NE-560 has been found to be the most suitable for this purpose.

Since most of the light from the He-Xe scintillations is in the ultra-violet region, which has a greatly reduced transmission through the acrylic windows and the photomultiplier faces, it is necessary to convert this light to the visible region where the phototubes are sensitive. This is achieved by coating the walls of the chamber and the acrylic windows with an organic phosphor able to absorb the light produced in the ultraviolet region and reemit in the visible region. The organic phosphor chosen was pp'-diphenylstilbene (DPS). The walls of the chamber were coated with a 90 $\mu gm/cm^2$ layer of DPS vacuum evaporated and the windows were coated with a layer of about 45 $\mu gm/cm^2$ of DPS. These two quantities seem to be the optimum for evaporation. Another fact that helps to improve the resolution of the

system, by minimizing the effect of the noise, is the use of two photomultipliers in fast coincidence(To74). When doing this, the gains of the two phototubes are matched by adjusting the high voltage applied to each.

2.6.4 STRESSES IN THE POLARIMETER

It is very important to know how the different stresses are distributed in the cylinder under high pressure. The subject has been under investigation for a long time and the literature is very extensive. I will give a short description of the different stresses, and the reader is referred to B.B Muvdi(Mu80) for more details.

Numerous industrial applications require the use of cylindrical containers for either the storage or the transmission of gases and liquid. Examples include cylindrical tanks used for the storage of gaseous oxygen under high pressure and the piping used to deliver high pressure liquids to hydraulic machines.

Cylindrical containers are generally identified as thick-walled or thin-walled pressure vessels. The distinction between these two types of vessels is based upon the nature of the circumferential stress distribution over the thickness of the cylindrical vessel; if the variation of this stress over the thickness is such that it may be assumed approximately constant, the cylindrical vessel is referred to as "THIN-WALLED"; if not, it is known as "THICK WALLED". This leads to the following rule of thumb to determine the nature of the vessel. If the diameter of a vessel is twenty or more times the thickness of the vessel it may be assumed to be thin-walled. According to this criterion we may say that our polarimeter is thin walled.

The principal stresses defined in a thin-walled vessel

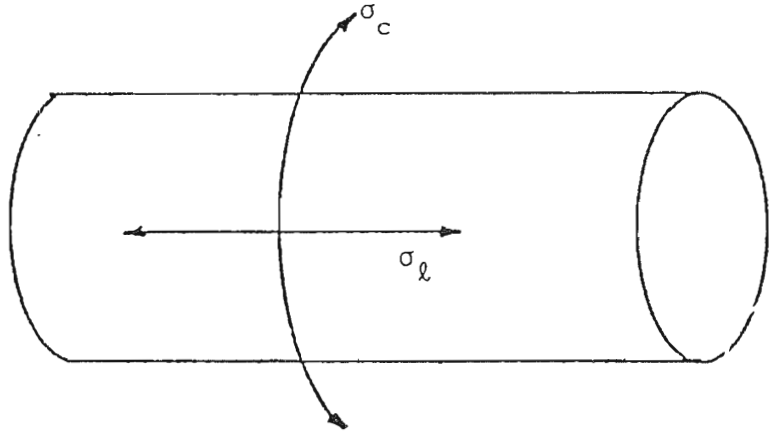

Fig. 2.23 Schematic diagram of the stresses in a thin-walled cylinder

are: longitudinal(σ_l), circumferential(σ_c), and radial(σ_r), see fig 2.23. In general, the radial stress, because of its relative magnitude, is not as significant a quantity as the circumferential stress in the case of thin walled cylinders. The longitudinal stress, and the circumferential stress when the thin-walled cylinder has closed ends, may be obtained by using expression 2.10, and 2.11.

$$\sigma_l = \frac{PD}{4t} \qquad 2.10$$

$$\sigma_c = \frac{PD}{2t} \qquad 2.11$$

D = Diameter of the vessel

t = Thickness of the vessel

Table 2.8 represents the value of the stresses calculated for different wall thickness.

TABLE 2.8

	WALL THICKNESS t = 2mm				
P	2000	2100	2200	2300	2400
σ_c	25006	26556	27506	28757	30007
σ_l	12503	13128	13753	14378	15003
σ_r	2000	2100	2200	2300	2400
	WALL THICKNESS t = 3mm				
σ_c	16663	17497	18330	19163	19998
σ_l	8333	8748	9165	9531	9998
σ_r	2000	2100	2200	2300	2400

Indeed it is not a problem to calculate the stresses in the cylinder, but the behaviour of the acrylic window under those stresses is very difficult to predict. We overcame this problem by testing windows of two different thicknesses, and materials (quartz and acrylic) to find

their failure pressure and then selected the most suitable for our purposes. The quartz windows have good optical properties. However, a 2cm thick and 7.5cm diameter quartz window shattered when the pressure was raised to a value close to 14480KPa(2100psi) and, a 3cm thick window shattered when the pressure was close to a value of 15860KPa(2300psi). The acrylic windows do not have as good optical properties as the quartz window. However they can stand a higher pressure which we feel is very important, and decided to use it in the final design of the polarimeter.

The scintillations from the polarimeter were calibrated using a 5.3 MeV alpha particles from polonium 210 located inside in the central zone of the polarimeter. Fig 2.24 shows the pulse height spectrum of the alpha source. The energy resolution of the system is 27% FWHM.

It is important to know how the pulse height depends on the gas mixture and the pressure. Experimentally we found the highest pulse height was obtained when there was pure xenon in the polarimeter. This can be seen from fig 2.25. The maximum value corresponds to 1380KPa of pure xenon. When we add helium, the pulse height decreases. Fig 2.25 summarizes these results.

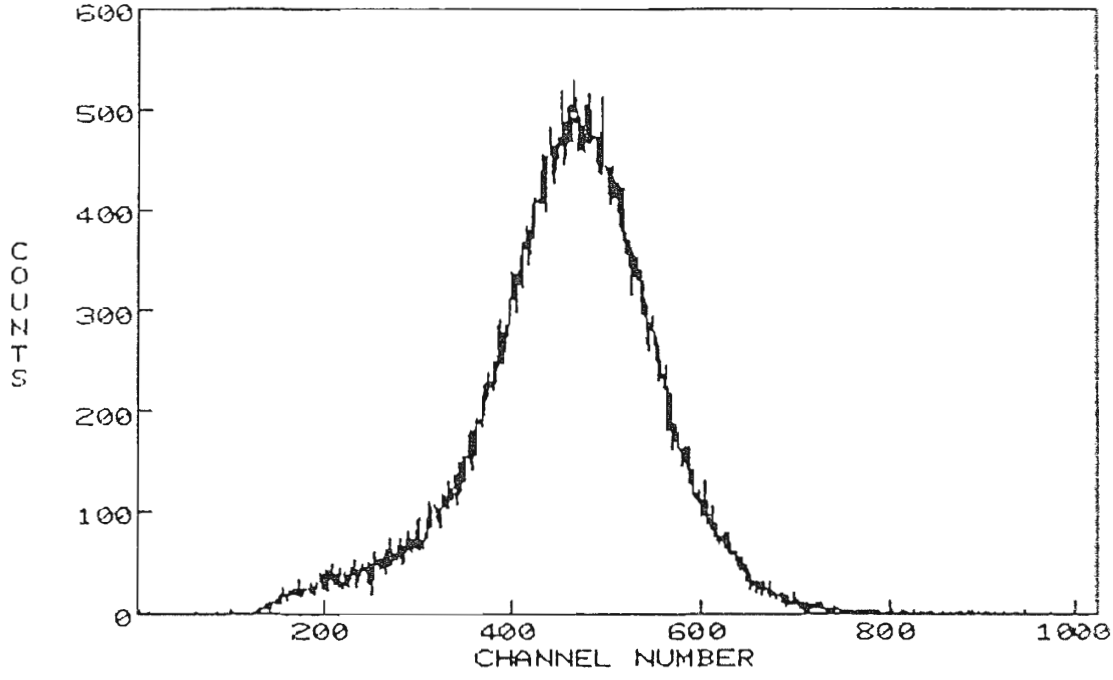

Fig 2.24 Pulse height of the alpha source in the Polarimeter.

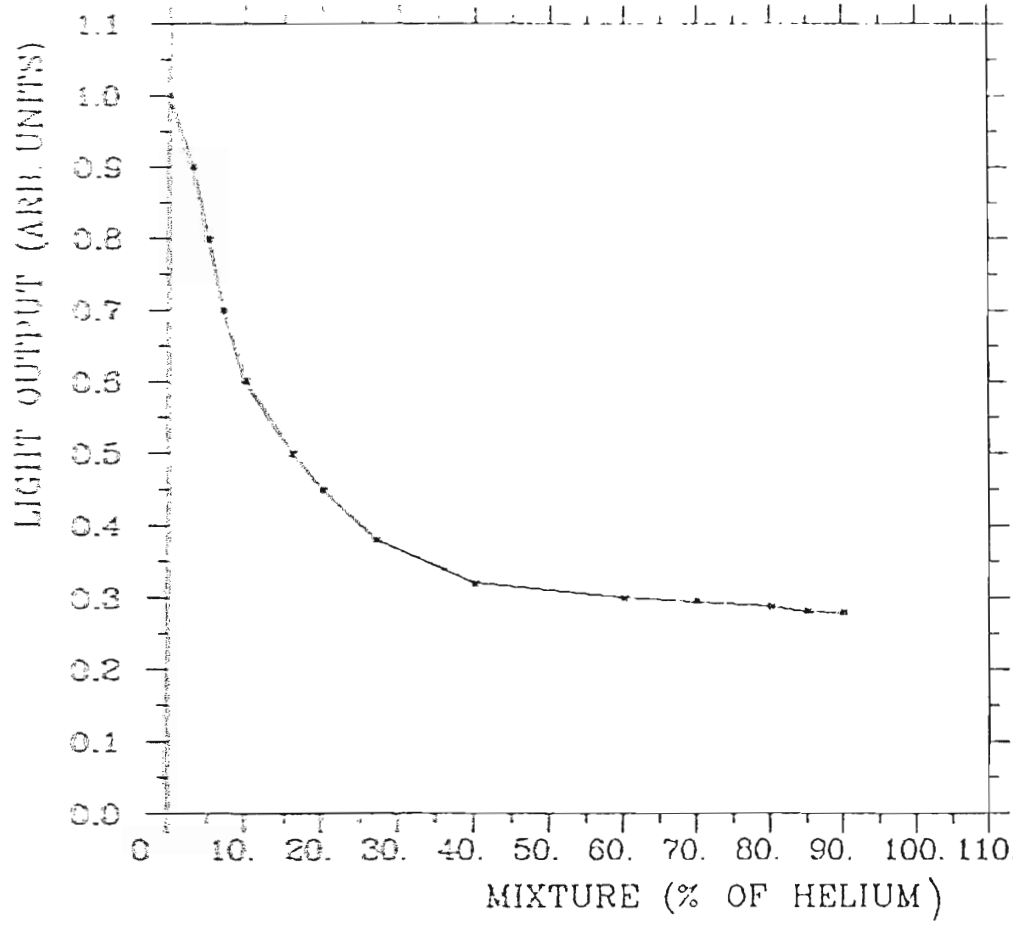

Fig. 2.25 Light output in the polarimeter as a function of the gas mixture (arbitrary units).

[illegible] SUPERCONDUCTING SOLENOID

[illegible]

The method of measuring asymmetries using two counters with and a spin precession solenoid is open to a number of criticisms associated with false asymmetries arising from the detectors having unequal detection efficiencies and being inaccurately positioned. The first criticism can be removed by interchanging the detectors and remeasuring the asymmetry, but this may introduce a further error due to inaccurate detector positioning. It is to overcome this error that the spin precession solenoid is used. The polarization direction of the beam is reversed, effectively interchanging the functions of the detectors; the "left" becomes the "right" and vice versa.

The spin precession solenoid produces a magnetic field whose axis is lined up with the neutron beam direction. In this way, the polarization vector is precessed in a plane perpendicular to the beam direction. The Larmor precession frequency of a neutron in the magnetic field is

$$\nu = g\mu_N H h^{-1}$$

where g = gyromagnetic ratio

μ = nuclear magneton

H = magnetic field

h = Planck's Constant

At a distance l from the centre of the solenoid along the axis the magnetic field is H(l). The relativistic expression for the angle of precession $\Delta\theta$ (measured as a fraction of a complete revolution) of a neutron with the velocity V in travelling through the solenoid is

$$\Delta\theta = \int_{-\infty}^{+\infty} H(l) g\mu_N h^{-1} dt$$

$$\Delta\theta = \int_{-\infty}^{+\infty} H(l) g\mu_N h^{-1} V^{-1} (1-\beta^2)^{\frac{1}{2}} dl \qquad 2.12$$

For a precession of 180^0 the line integral of the magnetic field required is

$$\int_{-\infty}^{+\infty} H(l) dl = hV/2g\mu_N (1-\beta^2)^{1/2}$$

A solenoid of length L with n turns/cm and current I amperes produces an integrated field.

$$\int_{-\infty}^{+\infty} H(l) dl = 4\pi nLI/10$$

Assuming that the neutrons start and end in low field regions, the current required to operate the solenoid is

$$I = 3hV/4\pi nL\gamma_N B(1-\beta^2)^{1/2} \qquad 2.13$$

Table 2.9 shows the values of the magnetic field(at the centre) and current needed to precess the neutron spin through different angles.

TABLE 2.9

		PRECESSION(degrees)			
		90		180	
ENERGY MeV	VELOCITY 10^7 m/s	B Tesla	I Amp	B Tesla	I Amp.
19.38	6.00	2.02	15.69	4.10	31.38
22.85	6.70	2.20	17.04	4.40	34.11
27.31	7.34	2.21	18.66	4.42	37.22

2.7.2 Depolarization due to Energy Spread

If the neutron beam is not monoenergetic, depolarization occurs. As shown by equation (2.12), due to neutrons of different velocities spending different lengths of time in the solenoid and being precessed by different amounts. This depolarization is estimated below for two different cases.

2.7.2.1 Gaussian Energy Distribution If we ignore the relativistic effect, the precession angle $\Delta\Theta$ is proportional to 1/v. Then

$$\frac{\Delta\Theta}{\Theta} = \frac{1}{2}\frac{\Delta E}{E}$$

And the average polarization can be written as

$$P = \frac{\int_{-\infty}^{+\infty} \mathrm{Cos}\Delta\Theta \exp[-\Delta\Theta^2/2\Delta\Theta_0^2 d\Delta\Theta]}{\int \exp[-\Delta\Theta^2/2\Delta\Theta_0^2 d\Delta\Theta]}$$

If $\Delta\Theta$ is small, then $\mathrm{Cos}\Delta\Theta = (1 - \mathrm{Sin}^2\Delta\Theta)^{\frac{1}{2}} \simeq (1 - \Delta\Theta^2/2)$

and $$P = -\frac{\int (\Delta\Theta^2/2) \exp(-\Delta\Theta^2/2\Delta\Theta_0^2) d\Delta\Theta}{\int \exp(-\Delta\Theta^2/2\Delta\Theta_0^2) d\Delta\Theta} + 1$$

If $$I = \Delta\theta^2 (\exp -\Delta\theta^2 / 2\theta_0^2) d\theta$$

then $$\Gamma = 1 - \tfrac{1}{2}\Delta\theta_0^2$$

For a precession angle $\theta = \pi$, and energy spread $\Delta E/E = 5\%$, $\Delta\theta_0 = 0.0785$ radians, and the average polarization is $p = 0.997$, so the depolarization in this case is estimated to be 0.3%. If the precession angle is $\theta = \frac{1}{2}\pi$, $\Delta\theta = 0.0393$ radians and the average polarization is $p = 0.999$, and the depolarization is estimated to be 0.1%.

2.7.2.2 Rectangular Energy Distribution

In this case the average polarization is given by the expression

$$P = \frac{\int_{-\Delta\theta}^{+\Delta\theta} \cos\Delta\theta \, d\Delta\theta}{\int d\Delta\theta} \qquad \frac{\int (1 - \Delta\theta^2/2) \, d\Delta\theta}{\int d\Delta\theta}$$

Then

$$P = 1 - \Delta\theta_0^2/6$$

For a precession angle $\theta = \pi$, and energy spread of 5%, = 0.0785, the

average polarization $p = 0.999$, and the estimate depolarization is 0.1%

Depolarization also occurs for neutrons travelling off the solenoid axis, since the magnetic field across the solenoid bore is not uniform, particularly at the ends of the solenoid where the magnetic field is not parallel with the solenoid axis, producing precession out of the correct plane.

Atkinson and Sherwood (At65) have calculated depolarizations resulting from this cause and find that the depolarization depends on the length to radius ratio of the solenoid. A solenoid for which this ratio is large produces less depolarization than one for which it is small. For a ratio of 10:1 the depolarization is calculated to be 1.1%. This figure is quoted for the situation in which the solenoid current has been adjusted to the value given by equation 2.13, in which neutrons travelling along the axis are precessed through 180^0. Those travelling off the axis are precessed by less than 180^0 and so the distribution of precession angle about 180^0 is asymmetric. The dependence of the depolarization on coil geometry (L/a) calculated by Atkinson and Sherwood was done for a particular trajectory defined by r=0.8a (a is the beam radius) and $\theta = \pi/2$ according to these calculations serious depolarization is confined to small values of L/a (less than 5; L-length of the solenoid). In the case of our solenoid the ratio L/a =10.8 and in consequence no serious depolarization occurs.

2.7.3 DESCRIPTION OF THE CRYOSTAT

The cryostat is of horizontal configuration having a two inch diameter room temperature bore concentric with the main body. The outer vacuum case is constructed from polished stainless steel with anodised duralumin end flanges in which the copper bore tube is located with shouldered flanges and sealed with "O" rings. Two stacks extend vertically above the main body. One contains the demountable current lead and the other the helium syphon entry and helium level probe connections (fig 2.26). Between these two are two smaller tubes, the nitrogen filler and vent tubes. The vent tube supports the electronics for the nitrogen level meter, and also has a 90^{0} elbow fixed to it to prevent damage to the leads connecting the level probe to the electronics.

The helium container is supported from two thin-walled stainless steel necks rising centrally to the top of the stacks. The helium container is enclosed by a gas cooled shield supported from the necks; it is wrapped in superinsulation 5cm thick over its diameter and ends. The helium can contains the magnet, syphon entry cone and two integral helium level probes, one being a spare. Electrical connections to the magnet i.e current leads and superconducting switch heater leads, are made via a connector located at the base of the stack A (fig 2.26). The plugs are mounted on the lower end of a thin walled stainless steel tube which forms the demountable lead. This can be removed once the magnet has been energised and hence reduce the helium

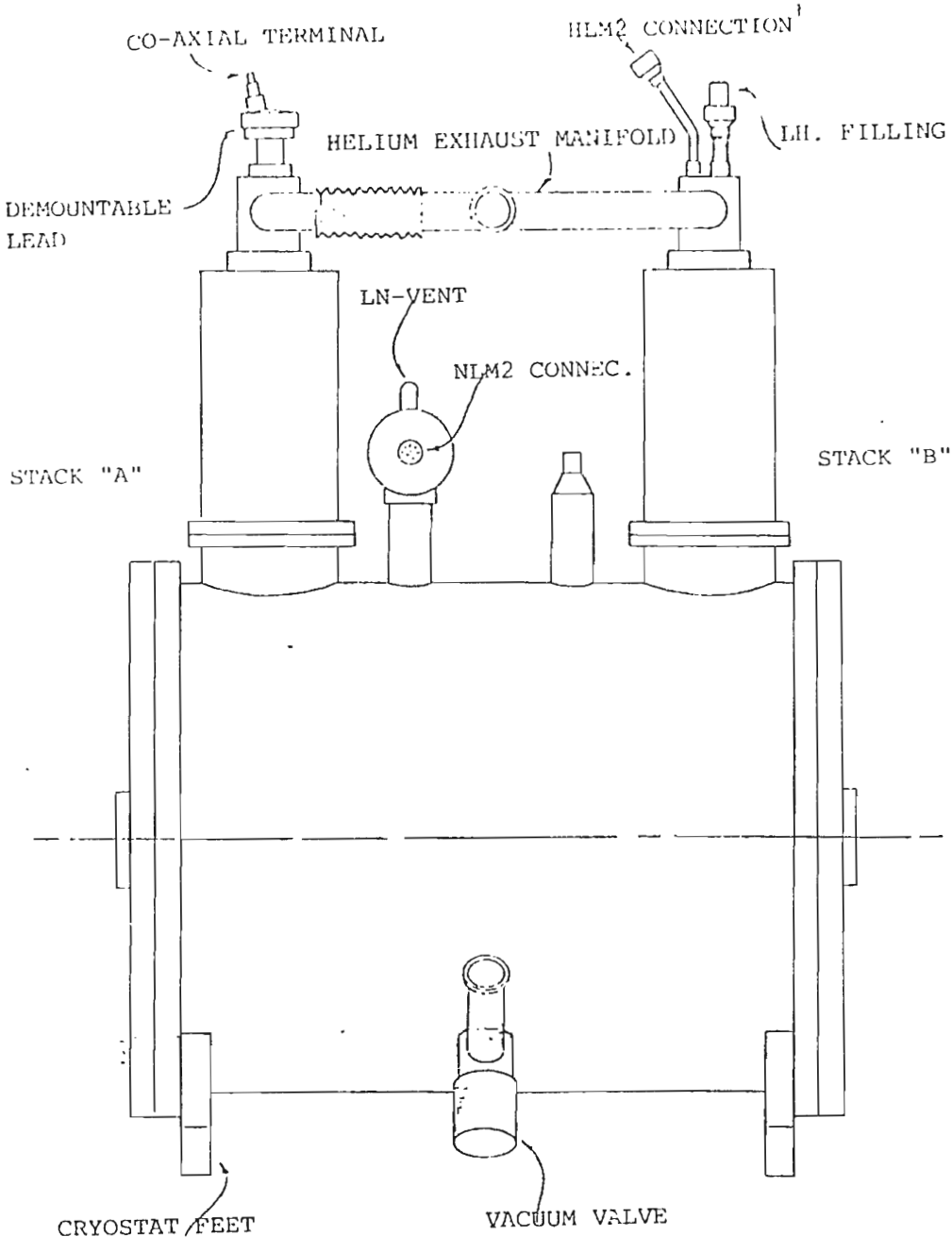

Fig. 2.26 Cross sectional view of the Cryostat.

boil-off. At the top of this lead there is a ten pin connector, with the connections to the switch heater, and a 60 amp co-axial terminal for connection of the current lead. Helium filling/removal and nitrogen precooling are aided by the addition of an entry cone located at the base of the stack B.

2.7.3.1 MAGNET

The solenoid is wound from multifilamentary niobium-titanium superconductor, comprising a full length coil section with a large fixed compensating coil at each end giving a long flat profile on axis. The magnet is designed to operate with a minimum helium level of one third of the container diameter i.e 7.60 cm (corresponding to 30% on the helium level probe). This is achieved by having all the joints and switch below this minimum level; conduction through the magnet former and superconductor maintains the temperature at 4.2K. A superconducting switch is supplied and connected across the magnet to allow persistent mode operation at any field value up to 7 tesla.

The magnet is fully protected from quench damage by 6 1/2 ohm x 60 watt resistors- one across each uninterrupted winding section. These resistors are mounted as high as possible inside the helium can and will be out of the liquid for the major part of the hold time being gas cooled during a quench.

Fig 2.27 is a profile of a calculated magnetic field along the axis of the solenoid.

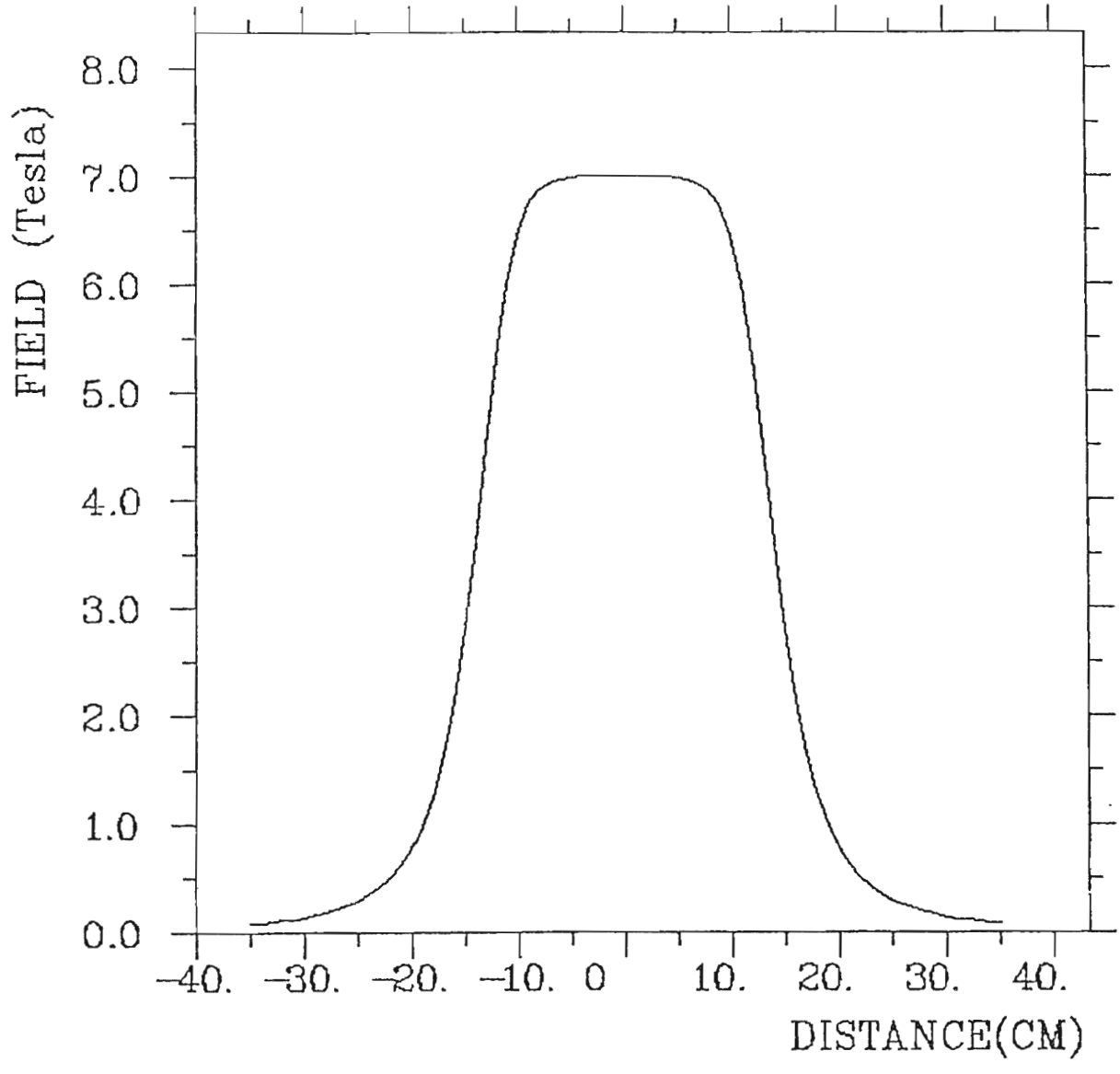

Fig. 2.27 Profile of the magnetic field produced by the superconducting solenoid.

7.7.3.1 MAGNET SPECIFICATIONS

TABLE 7.1a

CRYOSTAT	
Max overall length	682mm
Max diameter	488mm
Max overall height	970 mm
room temp bore tube diam	50.8mm
Max helium volume	15.8 litres
useful helium volume	8.5 litres
max/useful nitro. volume	10.4 litres
*Helium boil-off	40 ± 5 cc/hr
Nitro. boil-off	150 cc/hr
*Helium hold time	7.8- 10.1 days
Nitro. hold time	2.8 days
Helium boil-off with lead inserted	<300 cc/hr
Helium boil-off with full current in lead	<700 cc/hr

TABLE 2.11

MAGNET	
Max central field	7.0 tesla
Current for max	
Central field	54.8 Amps
**Homogeneity	± 5%
Amp/tesla	7.83
Tesla/amp	0.128
Stored energy at	
full field	35 Kjoules
10.4 litres	
Switch heater current	50-60 mA
Switch heater	
resistance	100 ohms

* Static boil-off with demountable lead removed

** 5% of central field over 18 cm axis (-9cm +9cm)

CHAPTER 3

ANALYSIS OF THE EXPERIMENT

3.1 ANALYSIS AND RESULTS

The collection and online analysis of data during the experiment was performed using the data acquisition and analysis system "XSYS", acquired from Triangle Universities Nuclear Laboratory(TUNL). This acquisition system was written for the Vax 11/750 computer and now is routinely used in our laboratory. Some of the capabilities of the current "XSYS" commands are briefly described below.

1. Allocate memory for data storage

2. Sort data during the experiment

3. Write data areas from memory to disk or tape files for storage purposes

4. Allows addition, subtraction or transfer of different data areas

5. Compute background in spectra

6. Create one dimensional graphic display of data areas

7. Defines regions of interest in the data areas by setting different gates

8. Transfer data between VAX/VMS files and XSYS data areas

9. Read data areas from disk or tape files to memory

10. Calculate area, centroid, and variance of gates in a specified data area

11. Create a graphic display of two-dimensional data

12. Allocate and manipulate gates for two-dimensional data areas

13. Transfer one data area into another

The sorting algorithm for each subprocess is determined by the EVAL-code written for each experiment

3.1.1 EVENT ANALYSIS LANGUAGE (EVAL)

EVAL is an event analysis routine for sorting data from online ADC or from event-by-event disk or tape files. Sorting multi-parameter data consists of many repetitions of a simple sorting algorithm. This algorithm normally consists of some sequence of numeric manipulations with various spectra being incremented according to the results of the test. EVAL provides a language which is broad enough to allow these algorithms to be easily specified. It is also simple enough to allow the compiler to generate code which executes quite quickly. EVAL provides a mechanism for interfacing with the XSYS data structures which contain the appropriate spectrum and gate arrays. A series of windows can be set from within the EVAL-routine. The object of these windows is to select from the incoming events only those lying within

the window to generate new spectra. The ability to call a Fortran subroutine from within EVAL is also provided.

During the experiment spectra are displayed on a VT100 retro-graphics terminal using two different programs DISPLAY, and TDD (Two Dimensional Display). Display has provisions for fitting backgrounds, computing areas and setting gates for one dimensional spectra. TDD contains similar functions for operating on two dimensional spectra. Gates for the EVAL Routine can be set from these programs.

The electronic set-up produces a set of 8 raw spectra during the experiment. Table 3.1 is a summary of all these spectra

TABLE 3.1

AREA	SPECTRUM	
1	RF-TAC	Time of Flight from the neutron production target to the gas Polarimeter
2	HPH	He-Pulse height in the gas Polarimeter
3	TAC-LEFT	Gamma and Neutron Time of Flight from the Polarimeter to the left Detector
4	TAC-RIGHT	Same as above in the right channel
5	LPH	Pulse Height left Detector
6	RPH	Pulse Height right Detector
7	LPSD	Pulse Shape discrimination in the left Detector
8	RPSD	Pulse Shape discrimination in the right channel

3.1.1.2 The Structure of the EVAL-routine

In terms of the EVAL language, an event consists of eight words. Each

of the spectra of table 3.1 represents a word. The Eval-routine then reads these words, stores them on tape and performs different tests on words and increments spectra if the words fulfill the requirements of the Eval-routine. The number of tests imposed is similar for the neutron and gamma events and is performed in the left and right channels. In order to be selected the neutron events must satisfy the following tests:

1. Left or right PSD v/s pulse height window test

2. The left events must be within the window set in the left Tac, Left PSD and left pulse height

3. The events must be within the window set in the RF-Tac spectrum

The same number of tests is performed in the right channel. The gamma events are treated in the same fashion.

We now will consider some of the most important spectra obtained during the experiment, some of them produced by the electronics set-up and, some produced by the Eval-routine.

3.2. TIME OF FLIGHT SPECTRA

3.2.1 TIME OF FLIGHT FROM THE TARGET TO THE POLARIMETER

Fig 3.1 Ilustrates the time of flight from the ^{13}C target to the neutron polarimeter. Time increases from right to left, because we started the TAC on the signal from the He polarimeter and

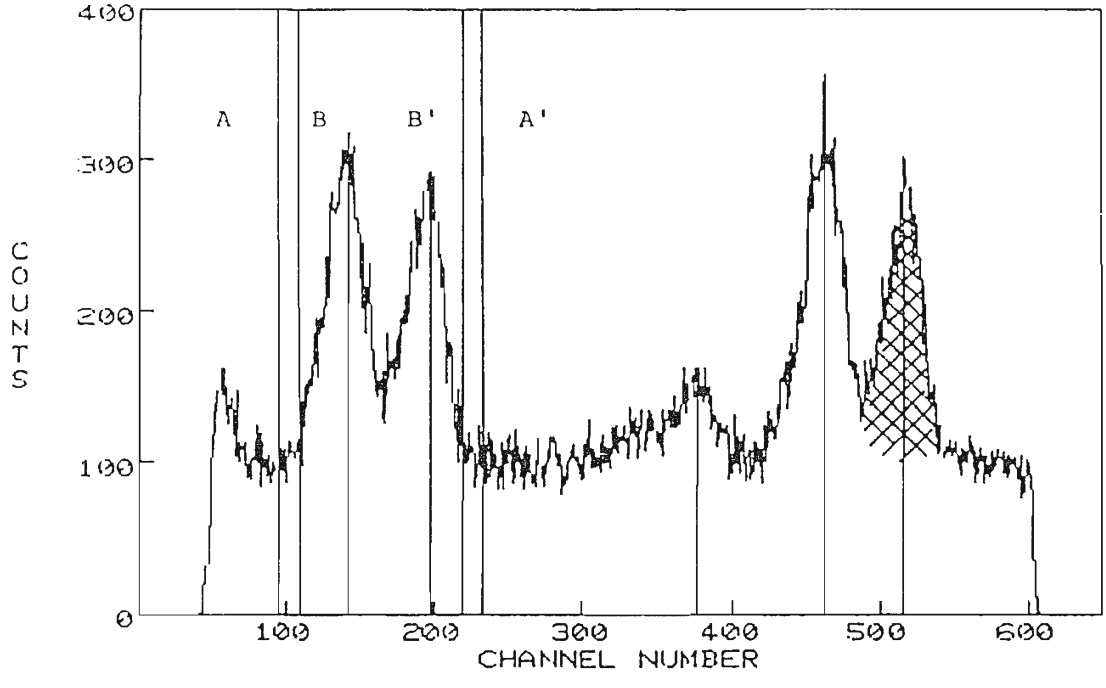

Fig. 3.1 Time of Flight from the target to the Polarimeter. The spectrum includes two beam bursts.

stopped on the signal coming from the R.F. The background is periodic with a period of 35.11 ns. This is because the beam arrives from the cyclotron in bursts at the rate of once every 35.11 ns. The peaks overlap due to the complex structure of the beam. The shaded peak centred in channel 517 corresponds to the neutrons leaving ^{13}N in its ground state (isobaric analog state of ^{13}C). The next peak to the left corresponds to the 3.51-3.55 excited states. The small peak centred in channel 376 is a gamma peak. The timing resolution in this case is 1.03ns FWHM. A stop pulse is applied only every other R.F cycle, so that the time of flight spectrum includes two beam bursts.

AA` and BB` correspond to the neutron and gamma gates set in this region. By setting these gates, we impose the condition that only the events within the gate will be analyzed. The energy resolution calculated for this time of flight spectrum in the best case is equal to 600KeV FWHM, and in the worst case is equal to 1.6MeV, and is typically 1MeV.

3.2.2 TIME OF FLIGHT FROM THE POLARIMETER TO THE SIDE DETECTORS

Fig 3.2. ilustrates the time of flight from the helium gas polarimeter to the side detectors. Zero on the time axis corresponds to those scintillations occurring simultaneously in the polarimeter and side detector. To the left are those occurring later in the detector and to the right, earlier. The peak to the right of the neutron group corresponds to gammas from the same beam burst. We see two "true coincidence" peaks superimposed on a background of

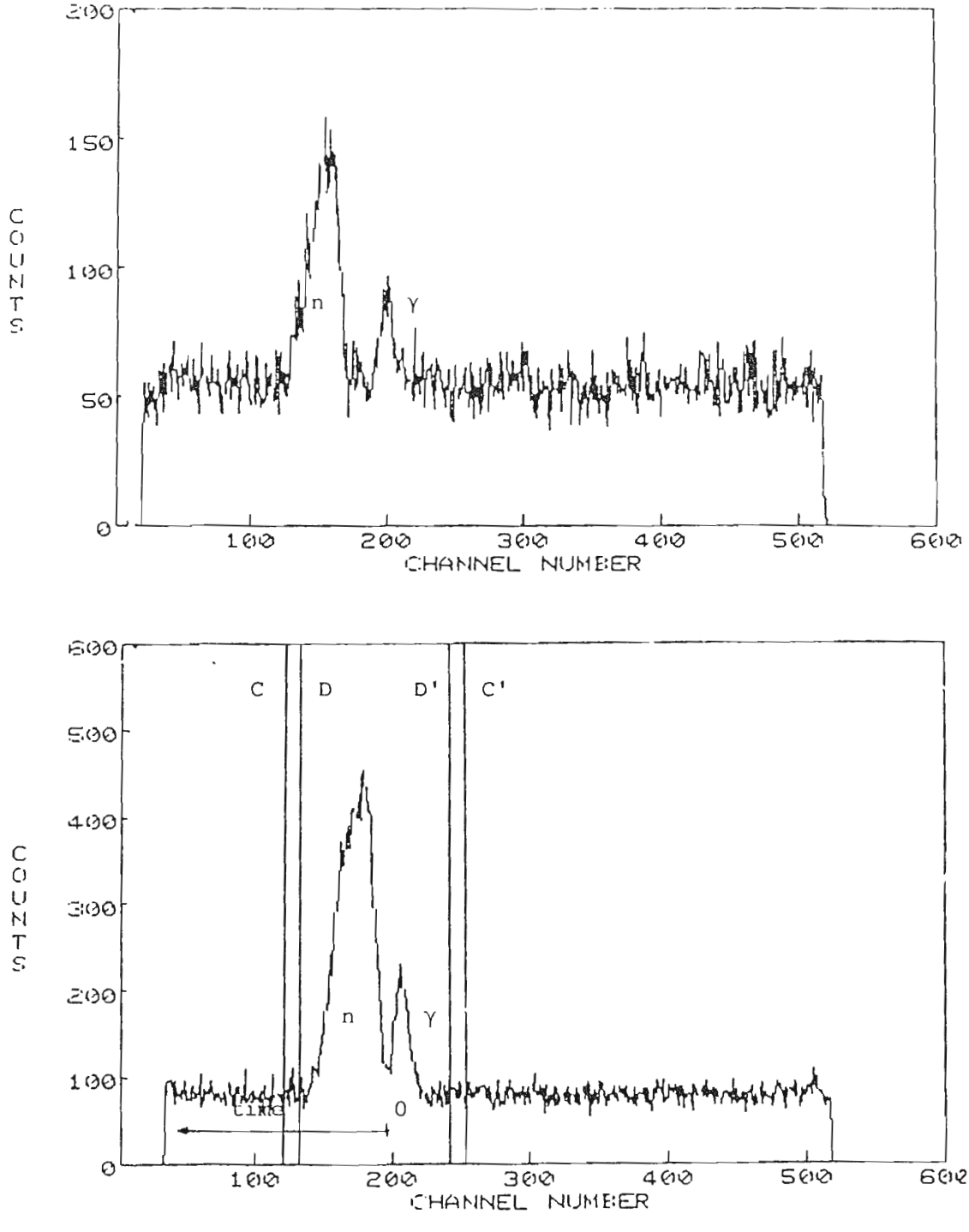

Fig. 3.7 Time of flight from the polarimeter to the side detector. Top fig corresponds to the left detector Botom fig. corresponds to the right detector. In the lower fig. the neutron and gamma gates have been included.

"random coincidences". The rate of true coincidences varies directly as the beam current but the rate of random coincidences varies as the square of the beam current. The maximum beam current which can be tolerated, and hence the running time required, is determined by the rate of random coincidences. In consequence one should reduce the random coincidences electronically as much as possible. This will result in minimum running time for a given statistical accuracy. The rate N_R, of random coincidences appearing in a time window τ of the TAC3 spectrum is given by:

$$N_R = 2\tau N_{pol} N_{det}$$

where N_{pol} is the effective count rate of the polarimeter and N_{det} is the effective counting rate of the detectors. N_{det} is reduced by the use of the puls shape discrimination technique and by the shielding. N_{pol} can be reduced by means of pulse height discrimination and time of flight information from the carbon target to the polarimeter. Since the time of arrival of neutrons at the polarimeter always bears a fixed time relation to the machine R.F, placing a window on the appropriate peak in the TAC4 spectrum (using TSCA1,in fig 2.12) permits the use of the polarimeter pulses which occur at the time of arrival of neutrons alone. This technique should discriminate against gammas from the production target. The fact we still have gammas in the TOF means that those gammas have been produced in the polarimeter. CC′ and DD′ are the neutron and gamma window set in this area to further reduce the number of unwanted events. i.e

those events that do not contribute to the yield of neutrons necessary to calculate the left- right asymmetry. The timing resolution in this case is 1.06ns. The energy resolution calculated for this time of flight spectrum in the best case is equal to 700KeV, and in the worst case is equal to 2MeV, typically being 1.4MeV.

In constructing the rest of the time of flight spectra we have imposed some conditions on the two dimensional displays that have to be fulfilled in order to have only real events included in the time of flight spectrum. For this reason we will now analyze some of those spectra.

3.3 PULSE HEIGHT INFORMATION

3.3.1 PULSE HEIGHT IN THE POLARIMETER

Fig.3.3 shows the pulse height distribution in the helium gas polarimeter. A monoenergetic beam of neutrons will produce a continuous distribution of pulse heights ranging from zero to some maximum value corresponding to the maximum recoil energy for that energy of neutron. A pulse height threshold has been set at channel 199 and pulses of lower amplitude than this do not appear. AA' corresponds to the neutron gate set in this region to cut the low pulse height neutrons. The resolution of the polarimeter was measured using a 5.3MeV alpha source(Fig 3.4) and is equal to 27%. This corresponds to an energy resolution of 5.23MeV for 19.40MeV neutrons incident on the polarimeter and scattered at 120^{0}. The range of the pulse height

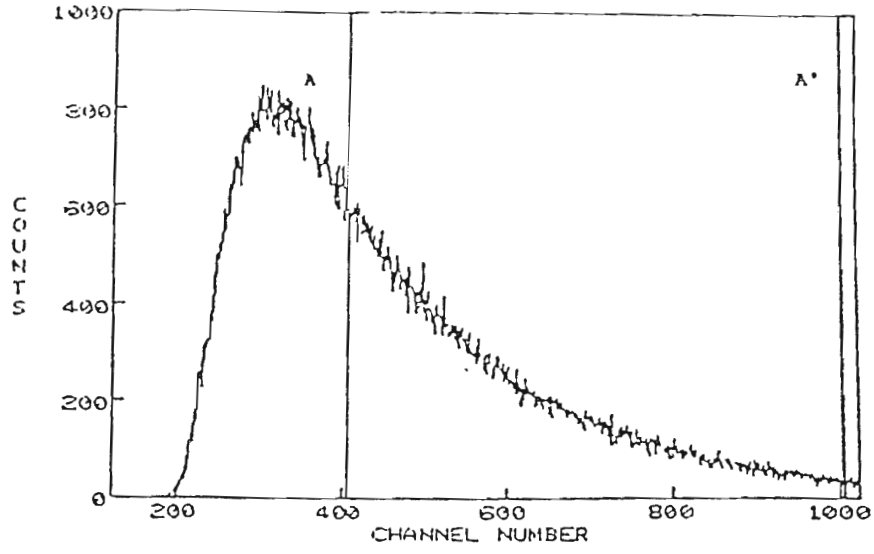

Fig. 3.3 Pulse Height distribution in the helium gas polarimeter. AA' corresponds to the neutron gate set in this region.

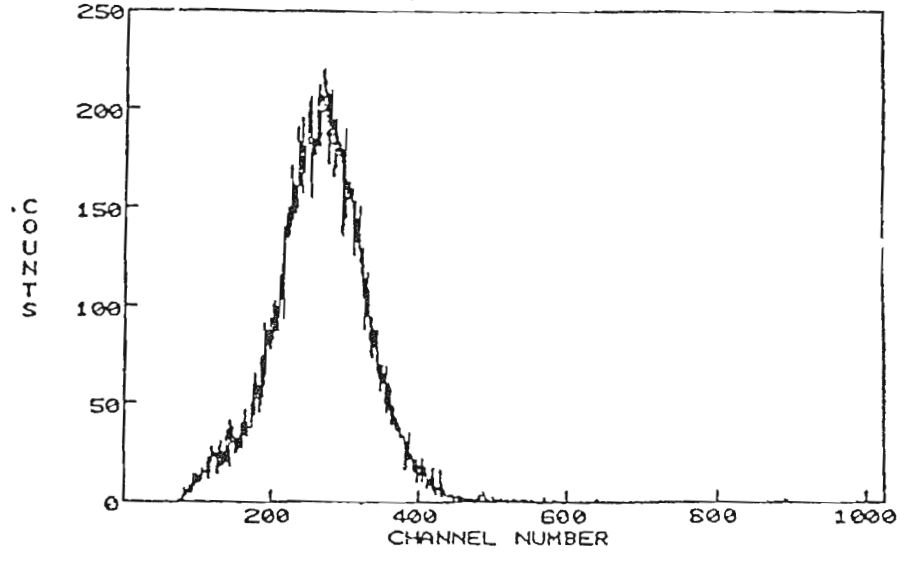

Fig. 3.4 Pulse Height from the 5.3MeV alpha source used as a calibration. This peak is eliminated by the coincidence criteria from fig 3.3

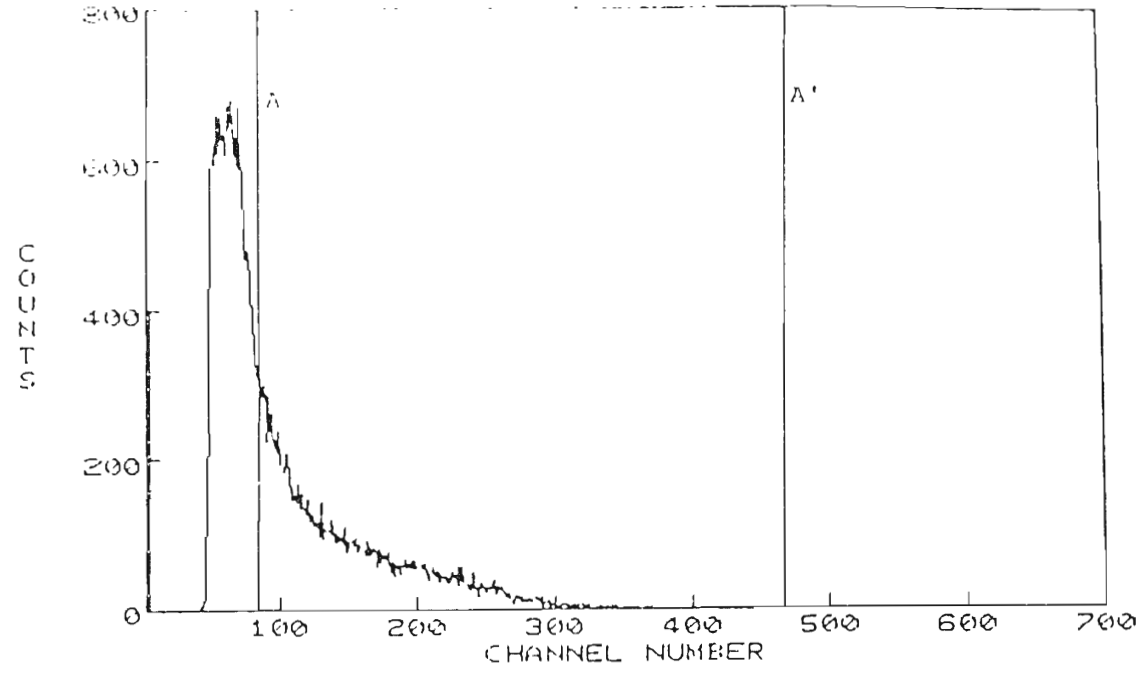

Fig. 3.5a Pulse Height in the left detector

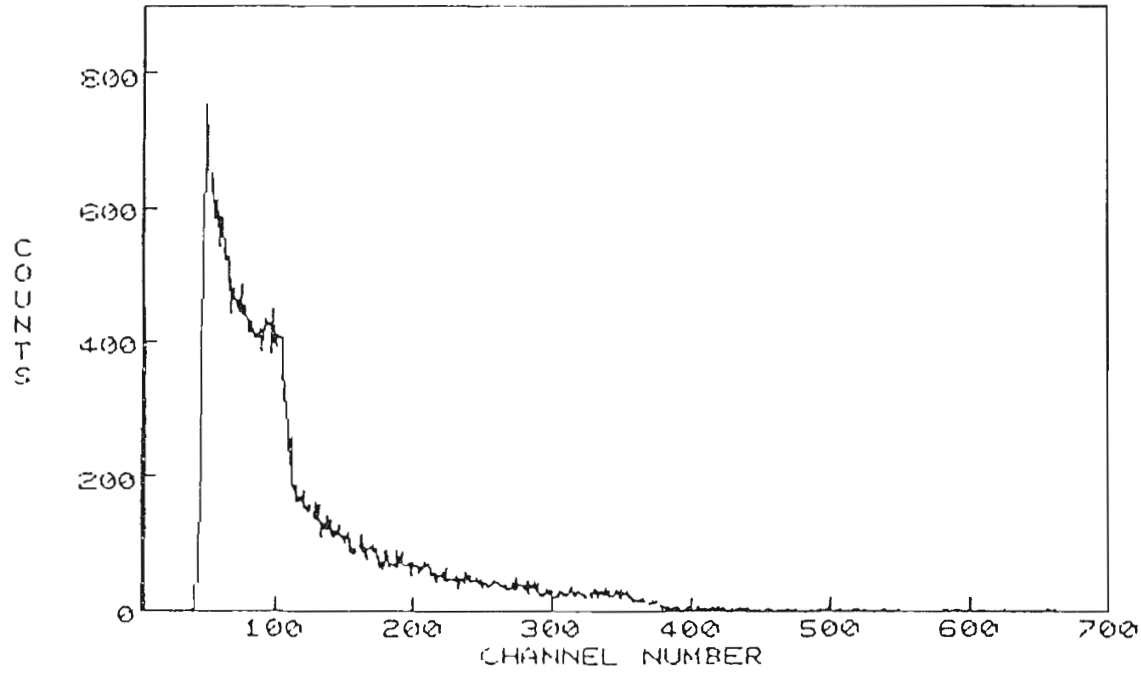

Fig. 3.5b Pulse Height in the right detector

of the scattered recoil alpha particles in the polarimeter goes from 17MeV at backward angles to 1MeV in the forward direction(for 27MeV incident neutrons on the polarimeter), and is in the range of 10MeV and 15MeV at 120^{0} for the three different incident proton energies.

3.3.1.1 PULSE HEIGHT SPECTRUM IN THE SIDE DETECTORS

Fig 3.5 illustrates the pulse height spectrum in the left and right detectors. The pulse height threshold has been set at the Compton edge of a ^{60}Co(1.1 MeV) source(this corresponds to channel 44). It is very important to set the pulse height threshold in the proper range. If, for example, the PH threshold is set below channel 44 then more events appear to the left of the ground state in the time of flight spectrum(fig 3.1). If the threshold is too low, low energy neutrons will overlap the ground state of the adjacent cycle. This situation is referred to as "wrap-around" and corresponds to slower neutrons from one beam burst arriving at the detector at the same time as the faster ground state group from the following beam burst. The detector pulse height threshold must be set just high enough to reduce the detection efficiency to zero for neutrons slow enough to wrap around. Our setting eliminates wrap-around and gives a good detection efficiency for the ground state group. To produce a good clean lower cutoff, the pulse height threshold was set by means of the TSCAI (fig 2.12). AA′ is the neutron gate set in this region to include only the highest energy neutron group.

3.4 TWO DIMENSIONAL SPECTRA

Fig 3.6 is a two dimensional representation of helium pulse height versus RF-TAC signal. The structure is the same as the singles spectrum for the time of flight from the carbon target to the polarimeter. By setting a two dimensional kinematic locus as indicated on the graph it is possible to discriminate against the events not included in this kinematic locus.

Fig 3.7 illustrates a two dimensional representation of helium pulse height versus time of flight to the side detectors. The kinematic locus this time is drawn around the peak so as to include only those events in a further analysis.

Fig 3.8 is a comparison of time of flight spectra The upper curve shows the raw data, while the lower curve results when neutron events in the side detector are selected. The peak near channel 200 in the upper curve is due to gamma-ray events and is barely seen in the lower curve. Note that time of flight increases to the left in this diagram. From these spectra it is easy to see the effectiveness of the kinematic and PSD cuts on the data.

Fig 3.9 illustrates the neutron time of flight from the gas polarimeter to the side detectors after neutron events are selected.

Fig 3.10 illustrates the pulse height spectrum in the side detectors after the gates of fig 3.3 have been applied.

Fig 3.11 illustrates the neutron time of flight from the

Fig. 3.6 Two dimensional representation of pulse height versus RF-TAC

Fig. 3.7 Two dimensional representation of pulse height versus time of flight to the side detector (lower fig.)

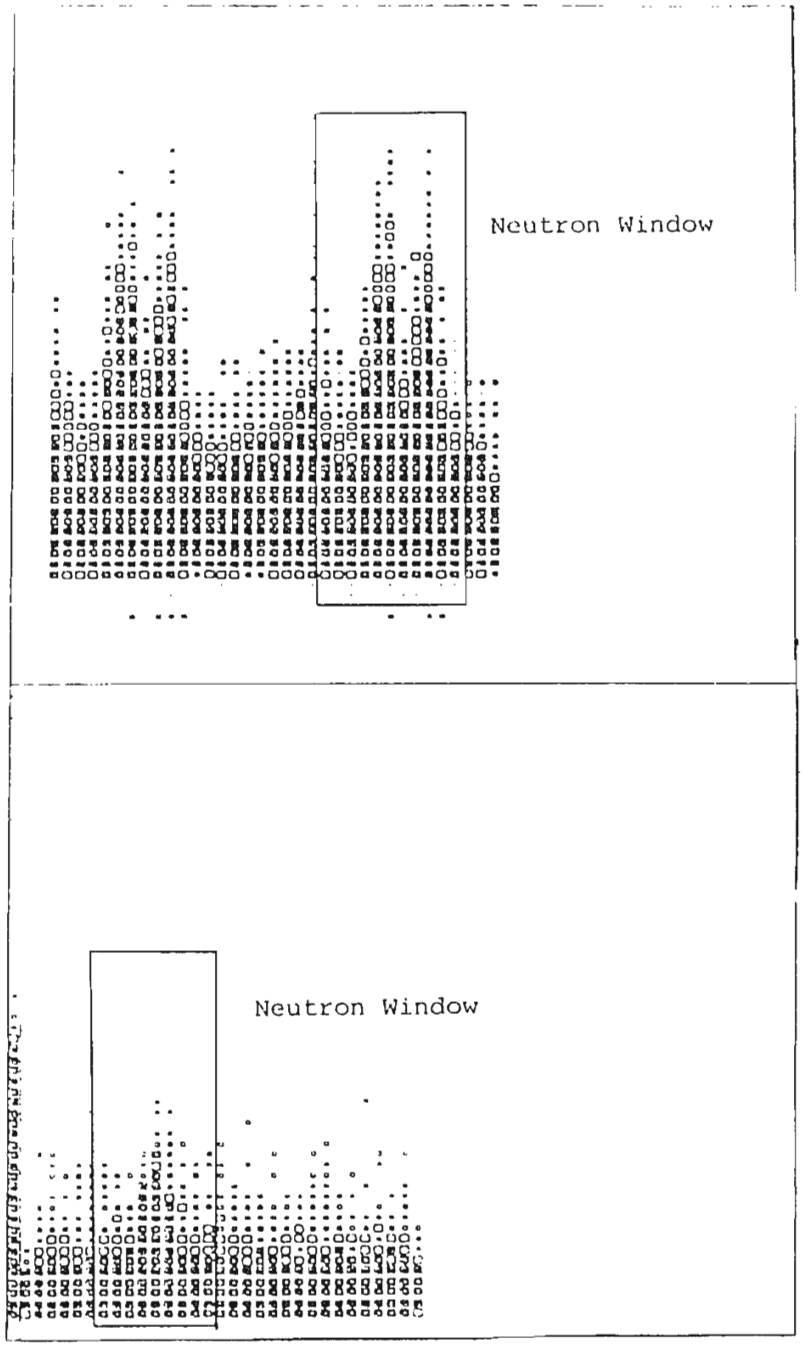
Neutron Window
Neutron Window

gas polarimeter to the side detector after imposing all cuts and selecting neutron events. The shaded peak corresponds to the neutron ground state of ^{13}N, the next to the left to the first and second excited states.

3.5 BACKGROUND

The shield used during the experiment is very effective in eliminating the background of neutrons and gammas coming to the side detectors directly from the carbon 13 target. There are however, some unavoidable sources of background. One of these is the contamination of the neutron beam by neutrons and gamma-rays created by interaction of the primary beam with the walls of the polarimeter. Another is caused by the presence in the experimental area of an ambient flux of neutrons and gamma-rays arising from interaction of neutrons in the walls and floor of the experimental area and from the interactions of the neutrons with the shield itself. The time correlation of this flux with the beam bursts is essentially random. The effect of this flux is to cause some accidental coincidences within the opening of the coincidence window which must be corrected for.

3.6 THE OFFLINE ANALYSIS

The offline analysis consisted mainly in playing the tapes back, re-sorting all the events, checking the gain of the phototubes by analysing pulse-height spectra and setting once again the gates and

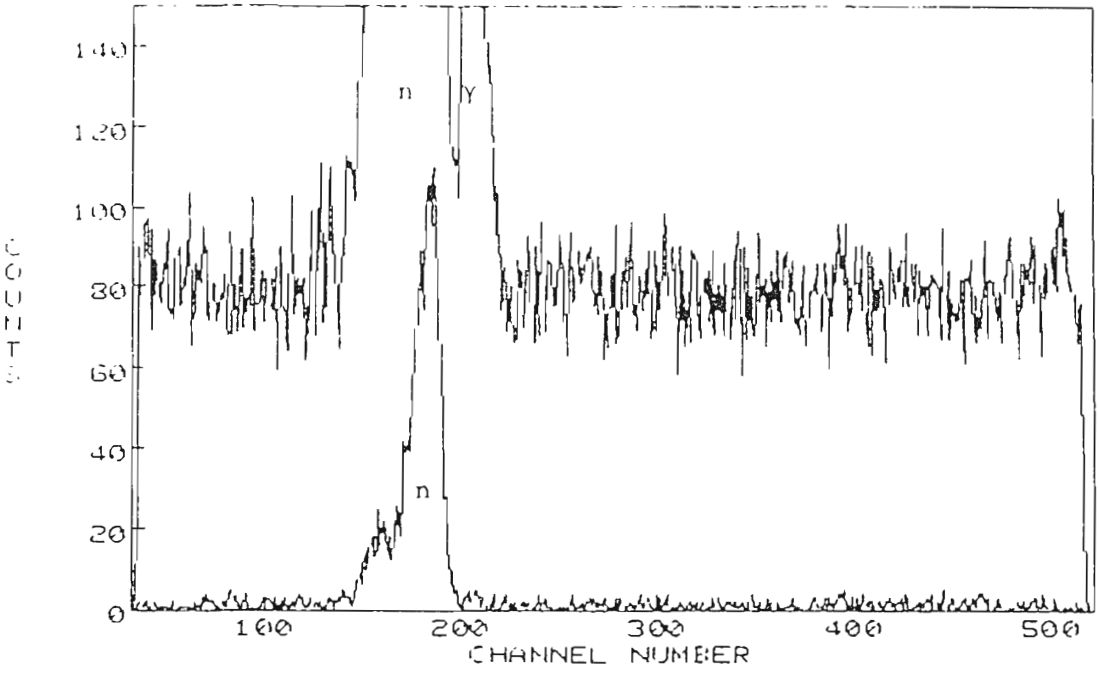

Fig. 3.8 Comparison of time of flight spectra. The upper curve shows the raw data, while the lower curve results when neutron events in the side detector are selected.

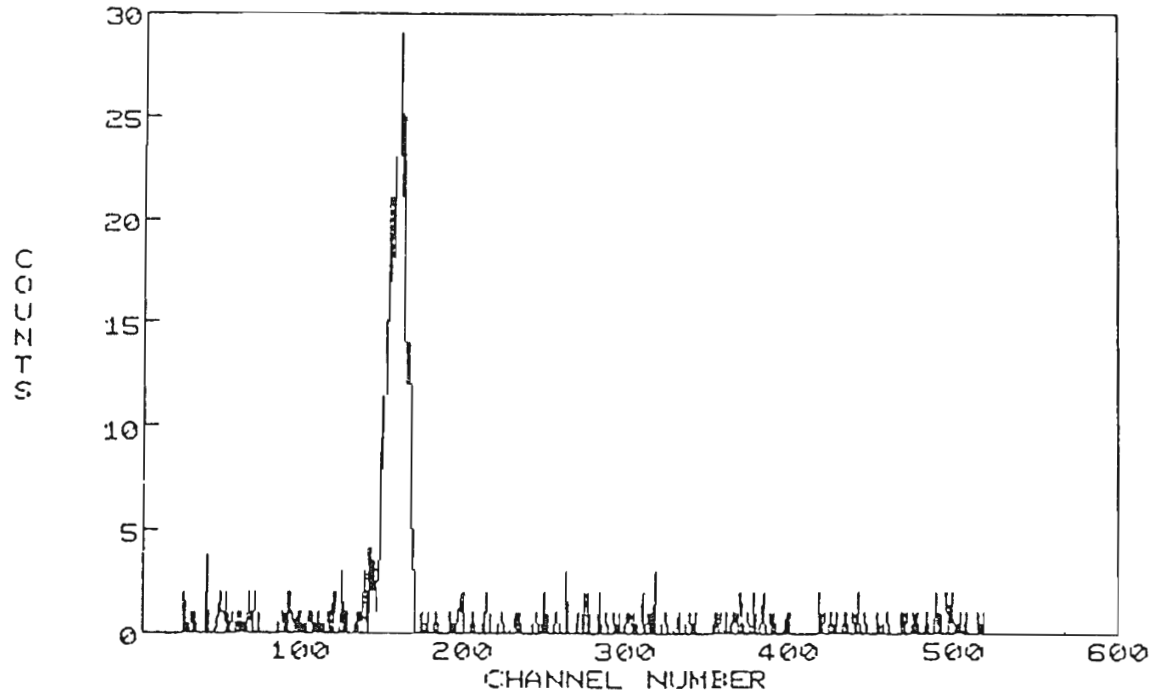

Fig. 3.9 Time of Flight from the Polarimeter to the side detector after the neutron events are selected.

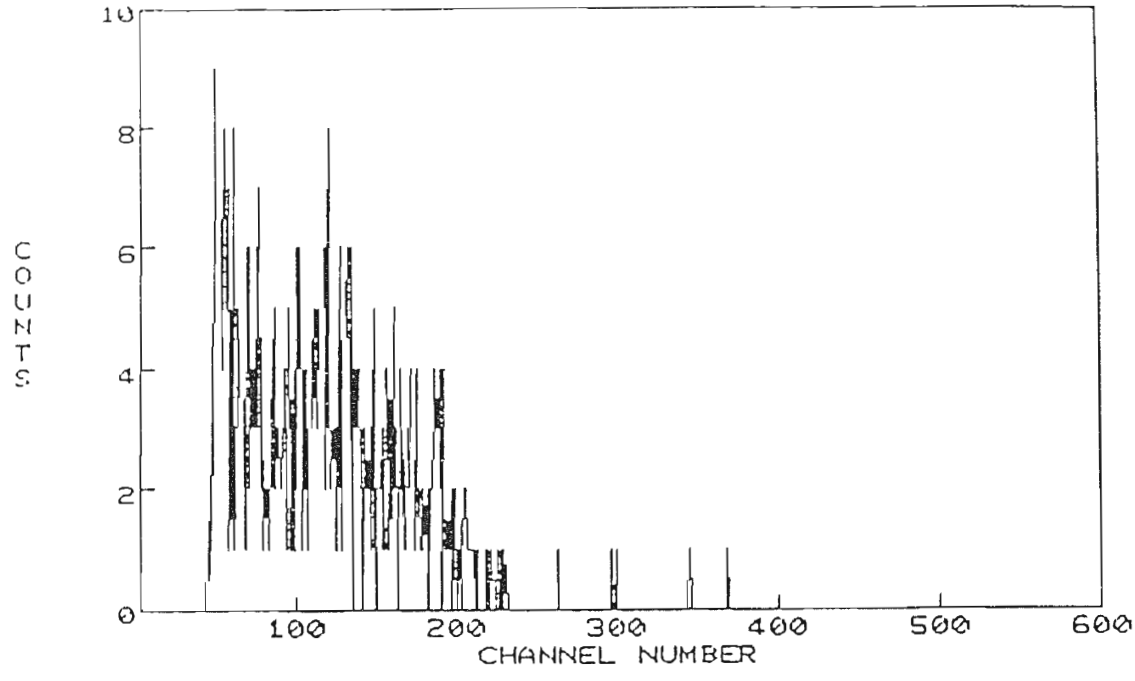

Fig. 3.10 Pulse Height in the side detector after the gates of fig 3.3 have been applied.

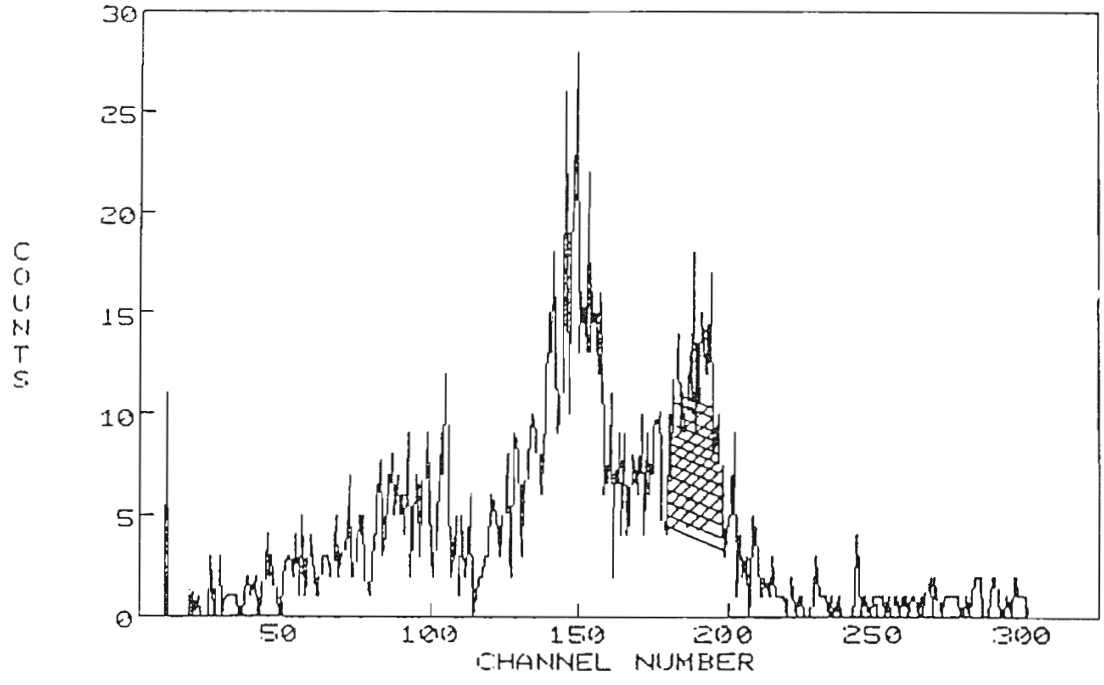

Fig. 3.11 Time of Flight from the Polarimeter to the side detector after imposing all the cuts and selecting neutrons events.

kinematic loci to further check the data collected during the experiment.

3.7 EXTRACTING NEUTRON YIELDS

The neutron yield from (p,n) reactions to the isobaric analog state is determined by integrating the IAS peak in the neutron time of flight from the polarimeter to the side detectors after all the cuts have been placed and only neutron events have been selected (Figs 3.11). This was done by using a computer code which allowed us to fit one, two or three Gaussian distributions to the spectrum after background subtraction (if required), using the method of non-linear least squares. This was generally straightforward.

3.8 NEUTRON DETECTION EFFICIENCY

The calculation of the efficiency of the neutron detectors is generally done using a Monte Carlo computer code. We obtained the latest version of this code from Kent State University. The program has been described by Cecil(Ce79). A particular application of this code was the calculation of the efficiency of a cylindrical NE-213 detector carried out by Ramsay(Ra80). In our experiment, we have used the same NE-213 cylindrical neutron detector of Ramsay(Ra80), so we decided to calculate the efficiency of these detectors using the same parameters.

Because neutrons are uncharged, they are not detected directly, but rather by means of the charged particles produced when they interact with hydrogen and carbon in the organic scintillator.

Knowing the composition of the scintillator and the light produced in it by the various charged particles, it is possible to calculate the fraction of incident neutrons that will produce a pulse height above threshold and hence be detected. When a neutron enters the detector a number of things can happen.

1. The neutron can pass through the detector without interaction.

2. It can scatter from a hydrogen atom.

3. It can scatter elastically from a carbon atom.

4. It can scatter inelastically from a carbon atom.

In case (1) the neutron remains undetected. In case (2) the kinetic energy E_p transferred from the neutron to the proton depends on the angle of recoil, θ_p of the proton through

$$E_p = E_n \cos^2 \theta_p$$

where E_n is the initial neutron energy. The scattered neutron may interact with a second atom or leave the detector directly. The recoil proton is slowed down as it moves through the detector by multiple coulomb scattering from atoms and atomic electrons. Some of the atomic and molecular excitations produced by the stopping of the recoil proton give rise to scintillations which are detected by the phototube. It is found that the light output of the scintillator depends in a non-linear way on the energy of the proton. This is because the higher the

density of ionisation produced around the proton path in the scintillator, the more is the scintillation light quenched by transfer of excitation energy to non-light emitting excitations. Light output is often specified by quoting the energy E_e of an electron which would give the same light output as the proton. Light output for electrons is much more closely proportional to energy than is the case for protons because of the relatively low density of ionisation produced by them. The light output of NE-213 for protons is closely fitted in terms of equivalent energy E_e by (Ce79)

$$E_e = a_1[\ 1 - \exp(a_2 E_p a_3)] + a_4 E_p \qquad 3$$

where a_1, a_2, a_3, and a_4 are constants (-2.83, -0.25, 0.93, and 0.83 respectively, when energies are in MeV). If the proton does not stop in the detector, but leaves it with kinetic energy E'_p, then the light output corresponding to a proton of energy E'_p is lost. If case (3) above occurs, that is, the initial neutron scatters elastically from a carbon atom in the detector, the light output is much lower than in case (2). This is so first, because the maximum energy transferrable from a neutron to a carbon atom is only about 14% of the energy of the neutron. Second, the recoil carbon atom causes a very high density of ionisation quenching. The light output of NE-213 for a carbon atom of 1 MeV, for example, is less than 19% of that of a proton of the same energy, which in turn has about 20% of the output of a 1 MeV electron.

3.9 THE PROGRAM

The program calculates the probability of a given neutron being detected in the NE-213 detector by simulating the neutron detection process. It follows each neutron (and its products) scatter by scatter until they are lost or fall to a negligible energy. Seven interaction channnels are provided, the n-p channel and six n-carbon channels, namely (n,n), (n,np), (n,2n), (n,γ), (n,3α) and (n,α). The technique used is a Monte Carlo or random walk calculation. In the simulation neutrons of energy E_n are required to be incident at a random point on a face of the detector. The point r at which a given neutron interacts in some way with the detector is chosen by the Monte Carlo relation:

$$r = -\ln q/[N_C\ \sigma^C_{tot}(E_n) + N_H\ \sigma^H_{tot}(E_n)]$$

where q is a random number between 0 and 1, N_C and N_H are the numbers of carbon and hydrogen nuclei per unit volume of the detector, and σ^C_{tot} and σ^H_{tot} are the total cross-sections for interaction of neutrons of energy E_n with carbon and hydrogen. If the point r lies outside the detector, the neutron is deemed to be undetected. If the neutron interacts inside the scintillator, the type of nucleus (C or H) it interacts with is chosen randomly, but always taking account of the carbon and hydrogen total cross-sections. If the reaction is with carbon, the reaction channel is chosen randomly, weighted by the individual reaction channel cross-sections. The direction of recoil of

an ion resulting from the interaction is chosen randomly based on the differential cross-section for the interaction concerned. The kinetic energy of the recoil is computed from kinematics and the range of the ion in the detector material deduced from polynomial fits to stopping power data. A geometrical subroutine determines whether the ion stops inside the detector and the light output of the ion is then given by equation (3) with appropriate coefficients. This procedure is repeated until typically 100,000 neutron paths have been simulated. The result is a pulse height distribution, the area under the curve being proportional to the probability of detection of neutrons of energy E_n. Comparison of the output of this code with experimental data (C-79) has shown excellent agreement. Fig 3.12 shows computed neutron detection efficiencies of the above detector for neutrons of energies between 12 and 35 MeV. The curves are labelled by the pulse height threshold (below which level scintillation light is not recorded) in units of electron equivalent energy, MeVee.

Because of finite pulse height resolution the pulse height spectrum is somewhat more smeared than the theoretical light intensity spectrum. To simulate the resolution smearing, the program translates the energy deposited by a monoenergetic charged particle into a Gaussian pulse height distribution, the width of the distribution being determined by the number of photoelectrons released. This number depends on such things as the state of the reflector paint in the scintillator, the coupling to the phototube and the photocathode itself. The more electrons released by the monoenergetic particle, the

better defined will be the corresponding pulse height. The efficiency of the detector has been calculated to be around 12% during the experiment.

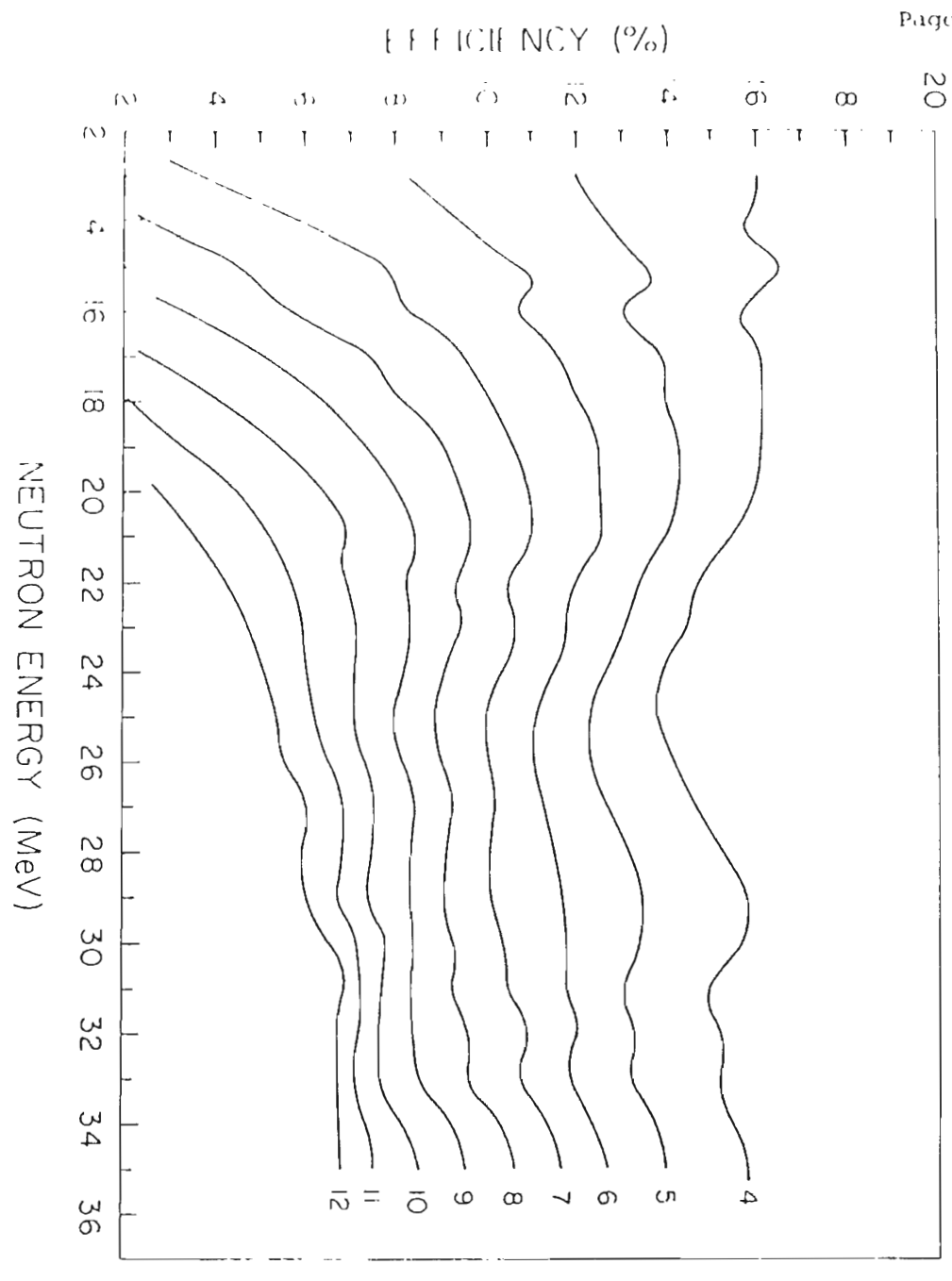

Fig. 3.12 Calculated efficiency for the NE-213 neutron detector.

3.10 ASYMMETRY CALCULATION

The asymmetry was calculated using the method described by Ohlsen and Keaton (Oh73). The essentials of this method and its advantages are presently summarized.

A beam of polarized neutrons incident upon a helium target will, in general, exhibit an elastic scattering differential cross section which is dependent, not only on the angle of deflection (θ), but also on the azimuthal angle (ϕ). This cross section is defined as follows:

$$\sigma(\theta,\phi) = \sigma_u(\theta)[\ 1 + P_y A_y(\theta)\ n] \qquad 3.1$$

where

1. σ_u = differential cross-section for unpolarized beam,
2. $\vec{P}_y$ = vector polarization of the incident neutron beam,
3. $\hat{n} = \hat{K}x\hat{K}'/|\hat{K}x\hat{K}'|$ = unit vector normal to the scattering plane,
4. $\hat{K}$ = unit vector in direction of the incoming beam,
5. $\hat{K}'$ = unit vector in direction of the outgoing beam,
6. $A(\theta,E)$ = analyzing power of helium like,

In a polarization experiment, two detectors are symmetrically placed at the same polar scattering angle so that the beam and the centroids of

the two detectors form a plane. The azimuthal angle between the two detectors is then 180^{0}. One detector is conveniently designated as the "right detector", the other, as the "left detector". If we neglect the finite size of the detector and also the possibility of multiple scattering, equation (3.1) leads to the following relation:

$$P\,A(\theta) = \frac{\sigma_l - \sigma_r}{\sigma_l + \sigma_r} = \frac{N(-\theta)/N(+\theta) - 1}{N(-\theta)/N(+\theta) + 1} = \frac{r - 1}{r + 1}$$

where

1. σ_r = differential cross section appropriate to right detector,

2. σ_l = differential cross section appropriate to left detector,

3. $N_r(+\theta)$ = number of counts in right detector,

4. $N_l(-\theta)$ = number of counts in left detector,

5. $r = \sigma_r/\sigma_l = N(+\theta)/N(-\theta)$

6. ϵ = asymmetry.

Thus under idealized conditions, if one knows the analyzing power $A_y(\theta)$, one can readily determine the component of the incident polarization in the direction n and vice versa.

The actual number of counts recorded in a detector, $N(\theta, \phi)$, may be written as follows

$$N(\theta,\phi) = nN_A\Delta\Omega E\sigma(\theta,\phi) \qquad 3.2$$

Here n, is the number of particles incident on the target. N_A is the number of target nuclei per square centimeter, $\Delta\Omega$ is the solid angle subtended by the detector and E is the efficiency for detection.

If two dissimilar detectors are used, or if there are slight differences in the pulse height requirements which are set for the two detection channels, expression 3.2 becomes

$$N_1(\theta,0) = L_1 = nN\Omega_1 E_1\sigma_0[1 + PA_y(\theta)]$$

$$N_2(\theta,\pi) = R_2 = nN\Omega_2 E_2\sigma_0[1 - PA_y(\theta)]$$

If we now "flip" the polarization, i,e let $\vec{p} \rightarrow -\vec{p}$

$$N_1(\theta,\pi) = R_1 = n'N'\Omega_1 E_1\sigma_0[1 - PA_y(\theta)]$$

$N_3(\theta,\phi) = L_2 = n'N'\Omega_2 E_2 \sigma_0[\ 1 + PA_y(\theta)]$ where the primes are used to indicate that the integrated charge and the effective target thickness may not be the same for the two runs. If we form the geometric means

$$L = \sqrt{L_1 L_2} = [nn'NN'\Omega_1\Omega_2 E_1 E_2]^{1/2}\sigma_0(\ 1 + PA_y)$$

$$R = \sqrt{R_1 R_2} = [nn'NN'\Omega\ \Omega\ E_1 E_2]^{1/2}\sigma_0(\ 1 - PA_y)$$

and solve for $pA_y(\theta)$ we find the left-right asymmetry ε to be

$$\varepsilon = \frac{L - R}{L + R} = PA_y(\theta)$$

which is independent of relative detector efficiencies and solid angles, of relative integrated charge, and of target thickness variations.

Those quantities commom to the two channels, i.e n and N, are averaged over the data accumulation period so that time fluctuations in the beam current or target density are of no consequence. On the other hand, those quantities which are different in the two channels, E and Ω, must not vary with time. Dead time in the counting equipment may be either common to the two channels or not, depending on the equipment used (dead time during the experiment was around 5%). If it is not common a correction is required. If we define the geometric mean of the number of particles detected by

detector 1 or 2 in the two intervals as N_1 or N_2 we have

$$N_1 \quad \overline{L_1 R_1} = \{nn'NN'[\ 1 - (pA_y)^2\ ]\}^{\frac{1}{2}} \Omega_1 \sigma_0 E_1$$

$$N_2 \quad \overline{L_2 R_2} = \{nn'NN'[\ 1 - (pA_y)^2\ ]\}\ \Omega_2 \sigma_0 E_2$$

The ratio of these is

$$\frac{N_1}{N_2} = \frac{\Omega E_1}{\Omega E_2}$$

That is, monitoring this ratio provides a check on the performance of the apparatus, this quantity is used to check the stability and to make software adjustment of the gain of the photomultipliers in offline analysis. and is required to be constant in time if the asymmetry determination is to be accurate.

3.11 STATISTICAL ERROR

The statistical error associated with a measurement of the asymmetry is given by

$$A = \frac{1}{p\sqrt{L + R}}\sqrt{[\ (1 - \varepsilon)^2(\Delta L)^2 \ + \ (1 + \varepsilon)^2(\Delta R)^2\ ]}$$

If $\Delta L = L$ and $\Delta R = R$ as for a single counting interval, the above

expression reduces to

$$\Delta = \sqrt{\frac{1 - \epsilon^2}{L + R}}$$

For the geometric mean $L = \sqrt{L_1 L_2}$ the error is given by

$$\Delta L = \tfrac{1}{2} L \sqrt{\frac{1}{L_1} + \frac{1}{L_2}}$$

and for the geometric mean $R = \sqrt{R_1 R_2}$ The error is given by

$$\Delta R = \tfrac{1}{2} R \sqrt{\frac{1}{R_1} + \frac{1}{R_2}}$$

Thus, the more general error expression of eq 3.3 is required if geometric means are to be used.

In measuring the asymmetry care has to be taken of the error produced by false asymmetry. By false asymmetry we mean that asymmetry which would still be observed in the apparatus if the beam polarization were to vanish. This type of error can be eliminated exactly by a "proper flip", In this case we assume that the polarization of the beam is reversed or that the analyzer is rotated through 180 degrees in such a way that the beam direction and position

...cell invariant with respect to each of the detectors. Experimentally, such a flip is carried out by using the superconducting solenoid. If detector 1 is at the left and detector 2 is at the right, the yields may be written

$$L_1 = N_1(\theta + \Delta\theta_1, 0) = nNE_1\Omega_1(\Delta r_1, \Delta\theta_1)\sigma_0(\theta + \Delta\theta_1)[1 + PA_y(\theta + \Delta\theta_1)]$$

$$R_2 = N_2(\theta + \Delta\theta_2, \pi) = nNE_2\Omega_2(\Delta r_2, \Delta\theta_2)\sigma_0(\theta + \Delta\theta_2)[1 - PA_y(\theta + \Delta\theta_2)]$$

where $\Delta\theta_1, \Delta\theta_2, \Delta r_1, \Delta r_2$ denote total error quantities. If a proper flip is executed, yields in detectors 1 and 2 become

$$R_1 = N_1(\theta + \Delta\theta_1, \pi) = n'N'E_1\Omega_1(\Delta r_1, \Delta\theta_1)\sigma_0(\theta + \Delta\theta_1)[1 - PA_y(\theta + \Delta\theta_1)]$$

$$L_2 = N_2(\theta + \Delta\theta_2, 0) = n'N'E_2\Omega_2(\Delta r_2, \Delta\theta_2)\sigma_0(\theta + \Delta\theta_2)[1 + PA_y(\theta + \Delta\theta_2)]$$

The important part of this assumption is that the errors in r and θ are correlated with the physical detectors and not with their position in space. Forming the appropriate geometric means, we have

$$L_{1,2} = \{nn'NN'E_1E_2\Omega_1(\Delta r_1,\Delta\theta_1)\Omega_2(\Delta r_2,\Delta\theta_2)\sigma_0(\theta_1+\Delta\theta_1)\sigma_0(\theta_2+\Delta\theta)\times$$

$$[1 + PA_y(\theta_1+\Delta\theta_1)][1 + PA_y(\theta_2+\Delta\theta_2)]\}^{\frac{1}{2}}$$

$$R_{1,2} = \{nn'NN'E_1E_2\Omega_1(\Delta r_1, \Delta\theta_1)\Omega_2(\Delta r_2,\Delta\theta_2)\sigma_0(\theta_1+\Delta\theta_1)\sigma_0(\theta_2+\Delta\theta)\times$$

$$[1 - PA_y(\theta_1+\Delta\theta_1)][1 - PA_y(\theta_2+\Delta\theta_2)]\}^{\frac{1}{2}}$$

If we assume for the moment that A_y is independent of scattering angle in the range $\theta + \Delta\theta_1$ to $\theta + \Delta\theta_2$ we have

$$\varepsilon = PA_y = \frac{L - R}{L + R}$$

i.e there is exact cancellation of false asymmetry effects. Since the form of Ω was not specified in the argument, it applies to both solid and to gas target geometries. Since $\Delta\theta_1$, $\Delta\theta_2$, Δr_1, and Δr_2 were each arbitrary, one does not even require symmetry in the analyzer. Table 3.2 summarises the results of the calculations of the asymmetries for the different energies using the method described above.

TABLE 3.2

ENERGY MeV	ASYMMETRY	POLARIZATION	ΔE ASYMMETRY	ANALYZING POWER	N_1/N_2
19.40	0.334	0.367	0.034	0.91	0.541
22.85	0.340	0.400	0.035	0.85	0.595
27.31	0.232	0.283	0.012	0.82	0.457

3.12 CORRECTION FOR FINITE GEOMETRY

Because of intensity reasons fast neutron polarization experiments are usually performed with relatively large scattering samples and side detectors. This broad geometry, however, makes necessary corrections to the measured asymmetry to account for the finite geometry of the detectors and the occurrence of multiple scattering in the polarimeter. These corrections are generally performed using a Monte Carlo computer code*.

In the following pages a summary of the papers of Miller(Mi70), and Tornow(To75,77) describing the computer code P.M.S., widely used to calculate the corrections to the experimental asymmetry due to these two factors, will be given.

The program simulates the actual geometry of the experiment, traces the scattering histories of thousands of neutrons

step by step. The paths are chosen randomly and each neutron is weighted according to the probability of its path and, from the histories, gives an estimated multiple-scattering asymmetry for an incident neutron beam of arbitrary polarization.

-------- *The computer code used in this work was acquired from Karlsruhe by courtesy of Hans Klages

The program takes a first estimate of the neutron polarization and, using it, estimates by Monte Carlo method the resulting scattering asymmetry. It then compares this asymmetry with the experimentally measured one and produces a new estimate of neutron polarization:

$$(P_{est})_2 = (P_{est})_1 \frac{\epsilon_{ex}}{\epsilon_{Monte\ Carlo}}$$

If ϵ_{exp} and $\epsilon_{Monte\ Carlo}$ agree within 2%, the process stops, data and graphs are plotted, otherwise $(P_{est})_2$ is used as a new estimate $(P_{est})_2$ of neutron polarization for a new iteration of the calculation, gives $(P_{est})_3$ and new $\epsilon_{Monte\ Carlo}$

For dealing with the multiple scattering correction, we need a relation for the polarization vector P′ of the scattered neutron in terms of the polarization of the incident neutron and relevant scattering parameters. In general, the polarization changes its direction and magnitude with each scattering according to the following relation

$$\sigma\vec{P}' = \sigma_u\{(\vec{P} + \vec{P}_1\cdot\hat{n})\hat{n} + (1 - P^2)D_n(\beta)[\vec{P}_1 - (\hat{n}\cdot P_1)\hat{n}]\}$$

where

1. $\vec{P}_i$ = vector polarization of the incident neutron beam,

2. P = Analizing power of helium

3. P' = polarization vector of outgoing neutron beam,

4. β = so-called "spin rotation parameter" of the helium,

5. $D_n(\phi)$ = a rotation operator which rotates the vector operand about the axis n through an angle ϕ.

Since eq.(3.1) gives σ in term of σ_u. The above equation may be used in the Monte Carlo program to trace the evolution of the polarization vector through a multiple scattering theory. This is necessary since the cross section of scattering toward the left or right detector at any particular collision is dependent upon the scalar product (for that particular collision) of the incident polarization vector with the unit vector normal to the scattering plane. To implement the Monte Carlo program, one needs the unpolarized cross section of helium σ_u, the analyzing power λ, and the rotation parameter β, all as functions of incident energy and scattering angle. The set of phase shifts used in the program corresponds to values of the incident neutron orbital angular momentum of $L = 0,1,2,3,4,5$ and total angular momentum of $J = L+1/2$. The scattering cross section is then calculated by the following expression

$$\sigma(\theta) = |g|^2 + |h|^2$$

where

$$g = \frac{1}{ik}\sum_{l=0}^{\infty} P_l(\cos\theta)\{(l+1)\sin\delta_{l+}\exp(i\delta_{l-}) + l\sin\delta_{l-}\exp(i\delta_{l+})\}$$

and

$$h = \frac{1}{ik}\sum_{l=1}^{\infty} P_l^1(\cos\theta)\sin(\delta_{l+} - \delta_{l-})\exp\{i(\delta_{l+} + \delta_{l-})\}$$

The phase shifts δ_{l+} for $J = l + 1/2$ and δ_{l-} for $J = -1/2$ are functions of energy. The coefficients $P_l(\cos\theta)$ and $P_l^1(\cos\theta)$ are the Legendre and the associated Legendre polynomials, respectively.

The scattering asymmetry of the helium is a function of energy and is defined by the relation given by Lepore(Le50):

$$A(\theta) = \frac{gh^* + hg^*}{gg^* + hh^*}$$

The rotational parameter ρ is determined by

$$\cos\rho = \frac{g^*g - h^*h}{(g^*g + h^*h)\sqrt{1 - P^2}}$$

$$\sin\rho = \frac{\mathrm{Im}(gh^*)}{(gg^* + h^*h)\sqrt{1 - P^2}}$$

The collision density of the neutrons in the helium scatterer is solved by the Monte Carlo method. The integral equation for the density

$\psi(r,E,\Omega)$ of particles emerging from a collision in direction interval $d\Omega$ around Ω is given by the expression

$$\psi(r, E, \Omega) = \iiint \psi(r', E', \Omega') T(r', r; E', \Omega') C(E', \Omega', E, \Omega, r) dr' dE' d\Omega' + S(r, E, \Omega)$$

where

$$T(r', r, E', \Omega) = \Sigma_t(r, E) \exp\left[-\int_0^{r - r'} \Sigma(S', E) dS'\right.$$

$$C(E', \Omega', E, \Omega, r) = \frac{\Sigma_s(r, E)\ P(E', \Omega', E, \Omega, r)}{\Sigma_t(r, E')}$$

1. $P(E', \Omega'; E, \Omega, r)$ = probability density that a neutron having energy E' and direction Ω just prior to undergoing scattering at r will after scattering have an energy E and a direction

2. $\Sigma_t(r, E')$ = macroscopic scattering cross section for neutron of energy E' at point r,

3. $S(r, E, \Omega)$ = the density at r of the source of neutrons of energy E and direction Ω no matter whether they come from the external source or result from the scattering of other neutrons,

4. S' = distance from r' to arbitrary point along path from r' to r.

At each collision point the probability of a neutron reaching each of the two detectors on subsequent flights is calculated. The product of the weight of the neutron and its probability of reaching the detector in the next flight form an estimate of the flux at the detector. This estimate is referred to as the "uncollided flux estimator".

The neutron flux at the point r in the detector resulting from a collision at r' in the helium is given by

$$\psi(r,E) = W_0 G(E' \rightarrow E, \Omega' \rightarrow \Omega) \Delta\Omega \exp\left[-\int_0^{r-r'} \Sigma(S',E)dS'\right]$$

where

1. W_0 = the statistical weight of the neutron after the collision at r',

2. $G(E' \rightarrow E, \Omega' \rightarrow \Omega)$ = the neutron scattering probability per steradian for changing the energy and direction E', Ω' into an energy and direction E, Ω,

3. s' = distance from r′ to arbitrary point along path from r′ to r

4. Y = the noncollision probability for the neutron to leak from the scatterer in one flight.

$$Y = \int_0^{r - r'} \Sigma(s',E)ds'$$

The solid angle $\Delta\Omega$ subtended by the detector at the collision point in the scatterer is calculated from the expression

$$\Delta\Omega = 4\sin^{-1}\frac{(a/2)(b/2)}{\sqrt{[(a/2)^2 + d]\,(b/2)^2 + d}}$$

This expression assumes the cylindrical surface of the detectors is rectangular with dimensions a and b located a distance d from the collision point in the scatterer.

The energy of the neutron scattered to the detector is determined from the neutron energy before the collision and the cosine of the scattering angle. The cosine of the polar scattering angle is determined from

$$\mu = \frac{V \cdot \Omega}{|V|} -$$

where

V = velocity of the neutron before the collision at r′ and

Ω′ = the unit vector in the direction from the collision point r′ to the detector r.

The cosine of the scattering angle is transformed to center of mass coordinates for the calculation of the neutron energy after the collision. In the center of mass system the cosine of the scattering angle is

$$\mu' = [(\mu^2 - 1) + \mu(A^2 - 1 + \mu^2)^{\frac{1}{2}}]/A$$

where A is the mass of the scatterer. The energy of the neutron in the lab system after the collision in then given by

$$E = E'[1 - \{2A/(A+1)^2\}(1-\mu')]$$

The scattering kernel $G(E' \rightarrow E, \Omega' \rightarrow \Omega)$ involves both an energy and angle change. However, the two quantities E and Ω are not independent because at the given energy E′ the selection of the scattering angle, (to hit the detector), also determines the neutron energy E after the collision. Thus

$$G(E' \rightarrow E, \Omega' \rightarrow \Omega) = E'[\{1-(2A/(A+1)^2\}(1-\mu')]g(\Omega' \rightarrow \Omega),$$

where $g(\quad \rightarrow \quad)$, the probability of scattering through the angle Ω is the following:

$$g(\quad \rightarrow \Omega) = \sigma(\theta,\phi) \Big/ \int_0^{2\pi} \int_0^{\pi} \sigma(\theta,\phi)\, d\theta\, d\phi$$

3.13 THE RESULTS

The program yields the following results:

1. Number of neutrons detected in each side detector after single, double and triple scattering in the scatterer along with the corresponding asymmetry values and statistical uncertainties.

2. plot of the spectrum of the energy of the recoil alpha particles in the polarimeter as a function of the incident neutron energies.

3. same spectrum as above but this time projected onto the x-axis.

4. plot of the two dimensional spectra time of flight between target and polarimeter versus helium recoil energy in the polarimeter.

5. plot of a projection of the same spectrum onto the x-axis

6. plot of a time of flight spectrum between the polarimeter and side detectors versus helium recoil energy in the polarimeter.

7. plot of a projection of the same spectrum onto the x-axis

8. plot of time of flight from target to the polarimeter versus time of flight from the polarimeter to the side detectors.

Preliminary calculations showed that triple-scattering events are of negligible probability therefore only single and double scattering are considered.

Table 3.3 represents the number of counts in both detectors when one and two collisions are considered. The standard deviation is also calculated.

TABLE 3.3

ENERGY	NUMBER OF	NUMBER OF COUNTS		STAN. DEV	
MeV	COLLISIONS	L.DETECTOR	R.DETECTOR	L.DET.	R.DET.
	1	0.8127E-05	0.4055E-05	0.6716E-08	0.1613E-08
19.40	2	0.1001E-06	0.8255E-07	0.2078E-09	0.6464E-09
	SUM	0.8227E-05	0.4138E-05		
	1	0.4759E-05	0.2586E-05	0.2281E-08	0.1232E-05
22.85	2	0.5386E-07	0.4542E-07	0.4078E-09	0.1650E-09
	SUM	0.4813E-05	0.2631E-05		
	1	0.2516E-05	0.1578E-05	0.1544E-08	0.4657E-09
27.31	2	0.1960E-07	0.1764E-07	0.1912E-09	0.1582E-09
	SUM	0.2536E-05	0.1596E-05		

The results of the set of calculations after the first iteration are presented in table 3.4

TABLE 3.4

ENERGY	NUMBER OF	ASYMMETRY				
MeV	COLLISIONS	CALCUL.	AVERAGE	ERROR E-03	EXPERI.	ERROR
19.40	1	0.3342	0.3306	+0.3558	0.3337	+0.0341
	2	0.3306				
	1	0.2959	0.2931	+0.3398	0.3404	+0.0350
22.85	2	0.2931				
	1	0.2291	0.2275	+0.5124	0.2317	+0.0123
27.31	2	0.2275				

The values in the first set of calculations are not within the 2" required, in consequence the program calculates a new set of values, these are presented in table 3.5 and 3.6

TABLE 3.5

ENERGY	NUMBER OF	NUMBER OF COUNTS		STAN. DEV	
MeV	COLLISIONS	L.DETECTOR	R.DETECTOR	L.DET.	R.DET.
—					
	1	0.8112E-05	0.4047E-05	0.1277E-07	0.6452E-08
19.40	2	0.9965E-07	0.8333E-07	0.6143E-09	0.8835E-09
	SUM	0.8212E-05	0.4130E-05		
	1	0.4909E-05	0.2401E-05	0.7333E-08	0.8065E-09
22.85	2	0.5404E-07	0.4430E-07	0.2577E-09	0.9203E-10
	SUM	0.4963E-05	0.2445E-05		
	1	0.2506E-05	0.1576E-05	0.5568E-08	0.2593E-08
27.85	2	0.1919E-07	0.1729E-07	0.4366E-10	0.3432E-10
	SUM	0.2525E-05	0.1593E-05		

TABLE 3.6

ENERGY MeV	NUMBER OF COLLISIONS	ASYMMETRY CALCUL	AVERAGE	ERROR E-03
19.40	1	0.3343	0.3307	±0.1930
	2	0.3307		
	1	0.3426	0.3399	±0.7595
22.85	2	0.3399		
	1	0.2278	0.2263	±0.5996
27.31	2	0.2263		

Table 3.7 is a comparison between the experimental and the calculated values of the asymmetry. From the table we can see that the consideration of the multiple scattering and finite geometry produce small reduction in the value of the experimental asymmetry, less than 1% for 19.40 MeV and 22.85 MeV, and around 2.3% for 27.31 MeV. The error in the calculations are smaller than the error calculated in the experimental case, because of the large number of neutrons used for the Monte Carlo calculation (40,000 neutrons).

TABLE 3.7

ENERGY	ASYMMETRY		ERROR	
MeV	CALCUL.	EXPERIMEN.	CALCUL*E-03	EXPER*E-01
19.40	0.3307	0.3337	+0.1930	+0.3416
22.85	0.3399	0.3404	+0.7525	+0.3504
27.31	0.2263	0.2317	+0.5996	+0.1239

Figs 3.13 to 3.17, represent all the spectra produced by the program. The different neutrons groups have been identified by using kinematic calculations.

3.14 MORE CORRECTIONS

The asymmetry has been measured and its value corrected for finite geometry and multiple scattering in helium, however, other corrections are necessary. For example:

1. Scattering from helium and xenon.

2. Scattering from xenon only

3. Scattering from helium and the iron cylinder

4. Scattering from iron flanges, including the window

Of all these corrections, it is not necessary to calculate the single scattering from xenon because the recoil xenon nuclei do not generate enough light in the scintillator to be detected (the fluorescence yield produced in n-Xe is negligible).

The contribution of neutrons scattered via the cylinder to the glass window or vice versa is negligible. These events require triple scattering in the scatterer in order to be detected and in consequence can be neglected(triple scattering events are of negligible probability).

We still have the contribution of the following double scattering processes.

1) He-Xe

2) Xe-He

3) Fe-He

4) He-Fe

We have estimated the contribution of these double scattering events to the asymmetry calculated using only single scattering events. This contribution is around 4% for each of the double scattering events.

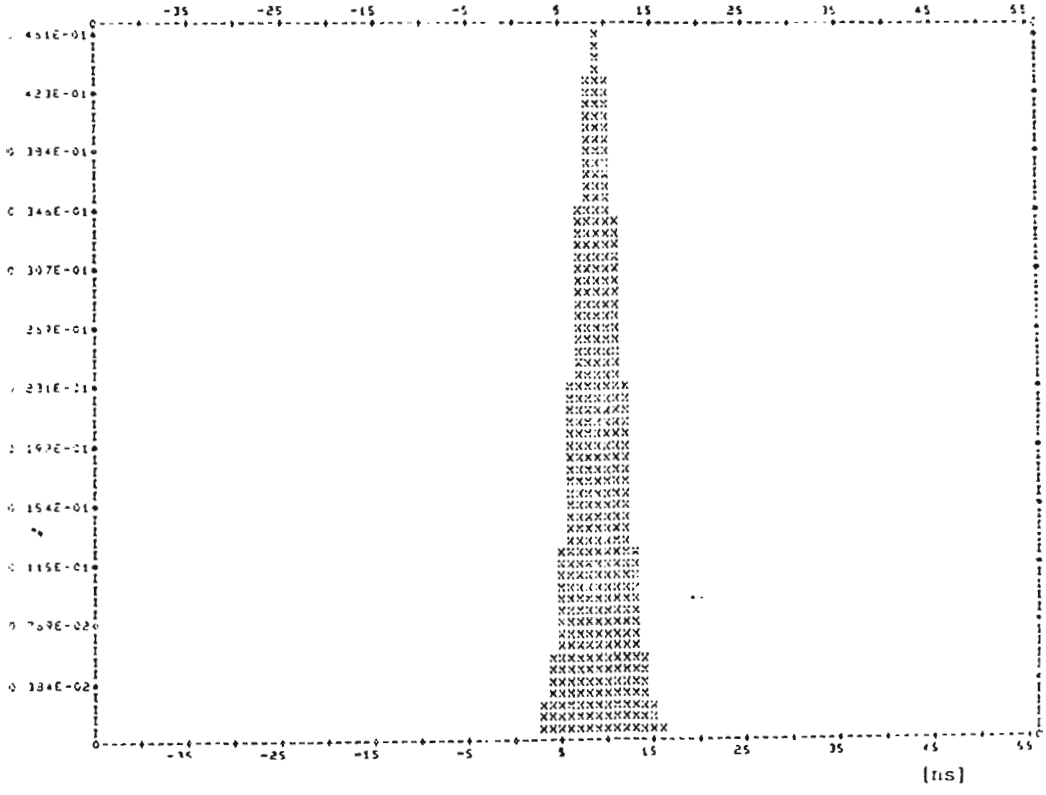

Fig. 3.13 Time of Flight from the target to the Polarimeter.

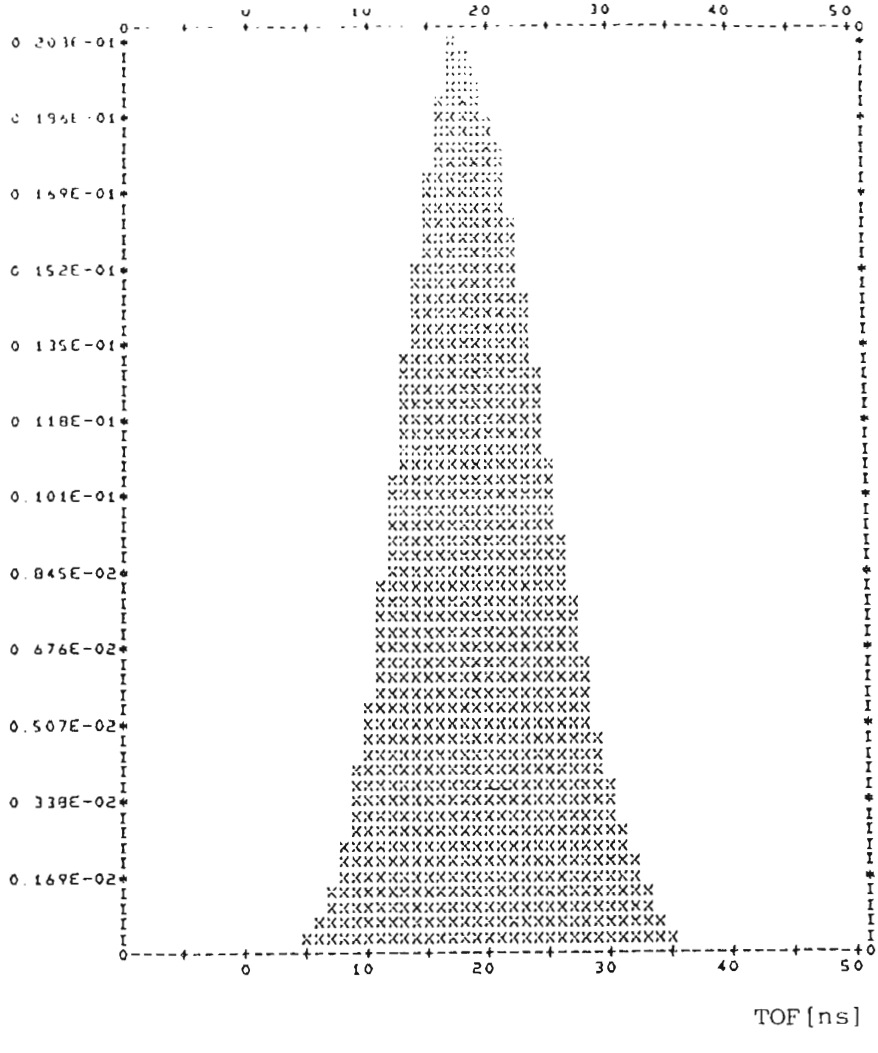

Fig. 3.14 Time of Flight from the Polarimeter to the side detector as calculated by the program.

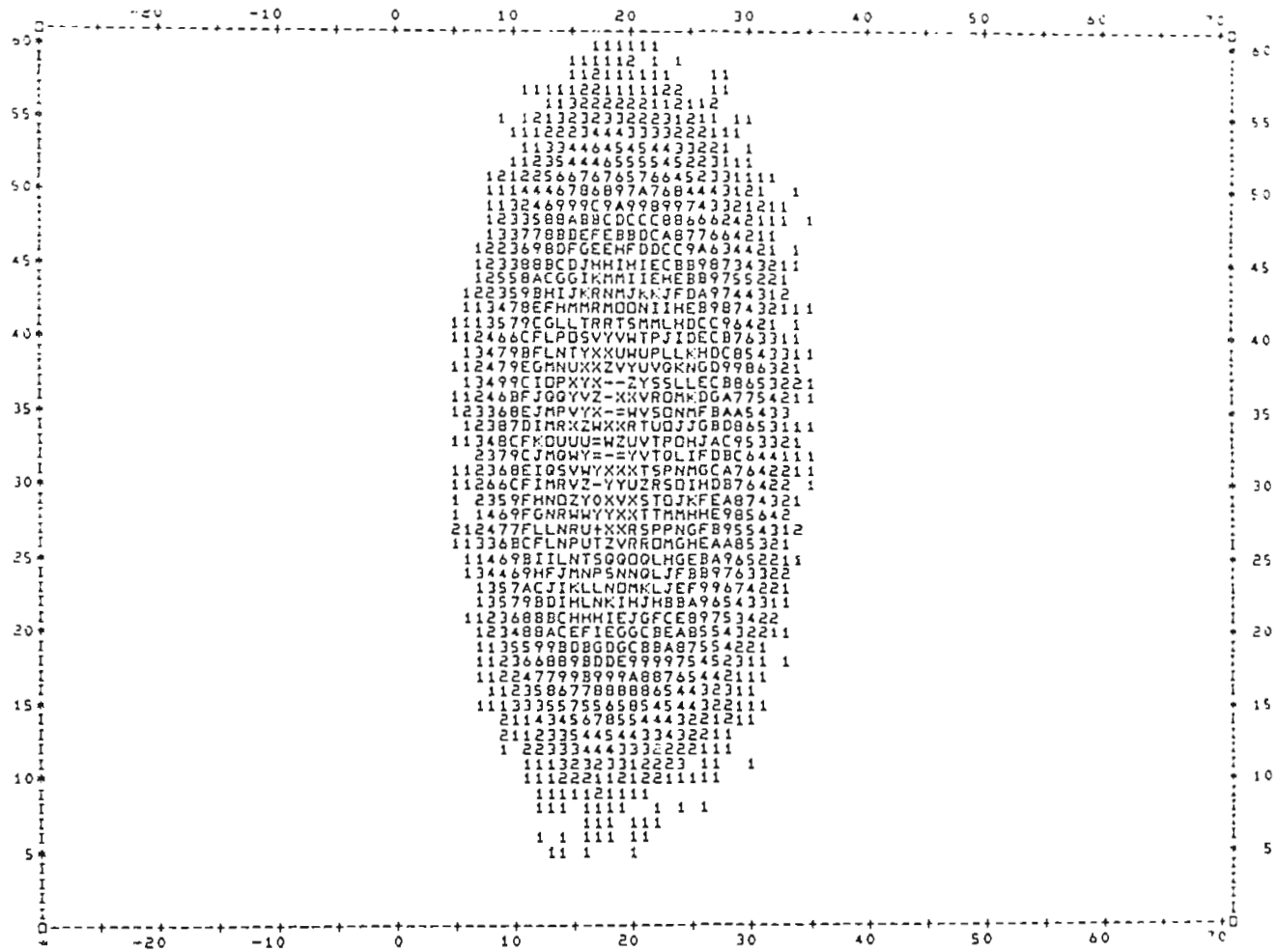

Fig. 3.15 Energy of recoil alpha particles versus time of flight from the polarimeter to the side detector calculated by the program

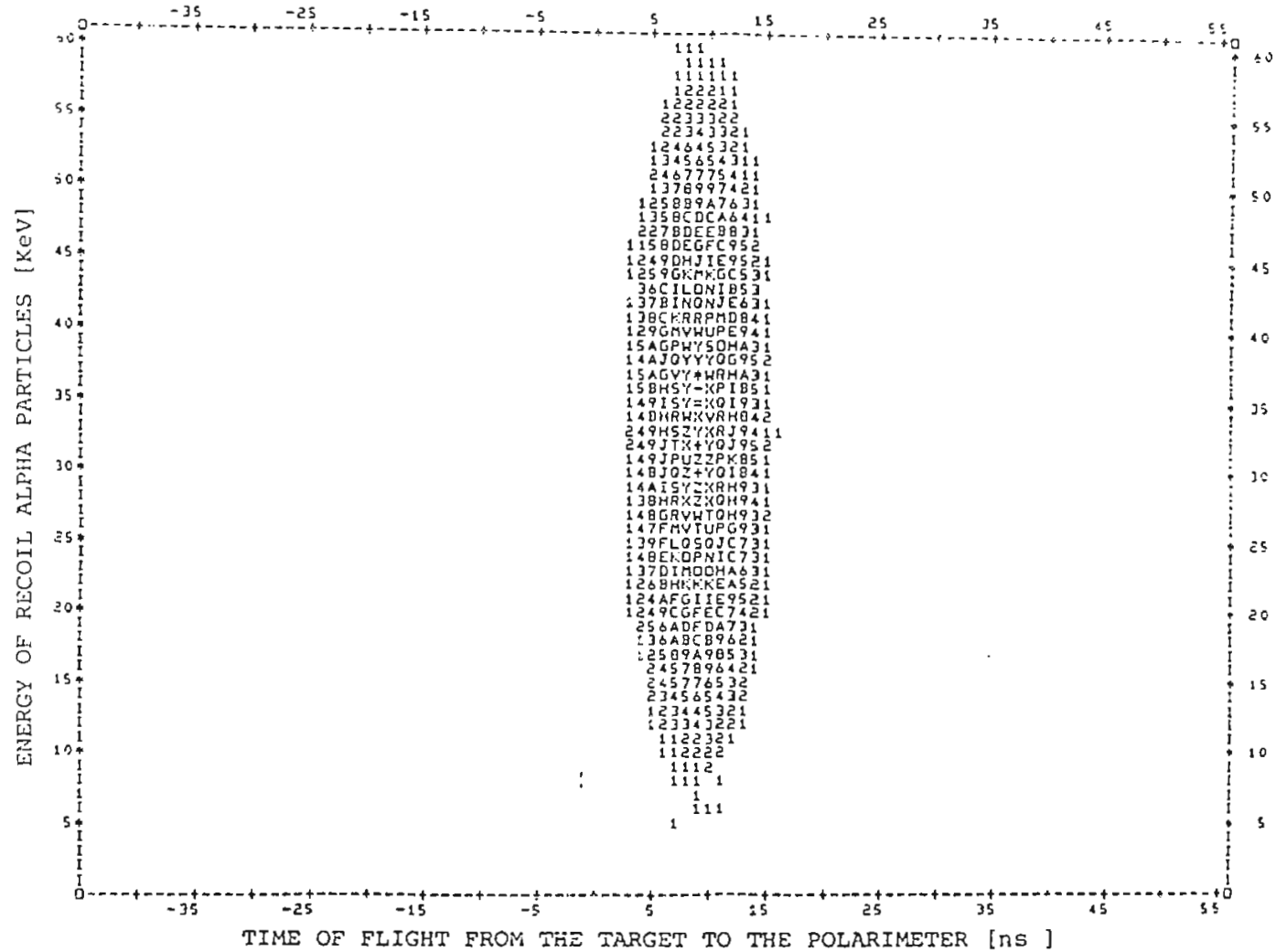

Fig. 3.16 Energy of recoil alpha particles versus time of flight from the target to the polarimeter

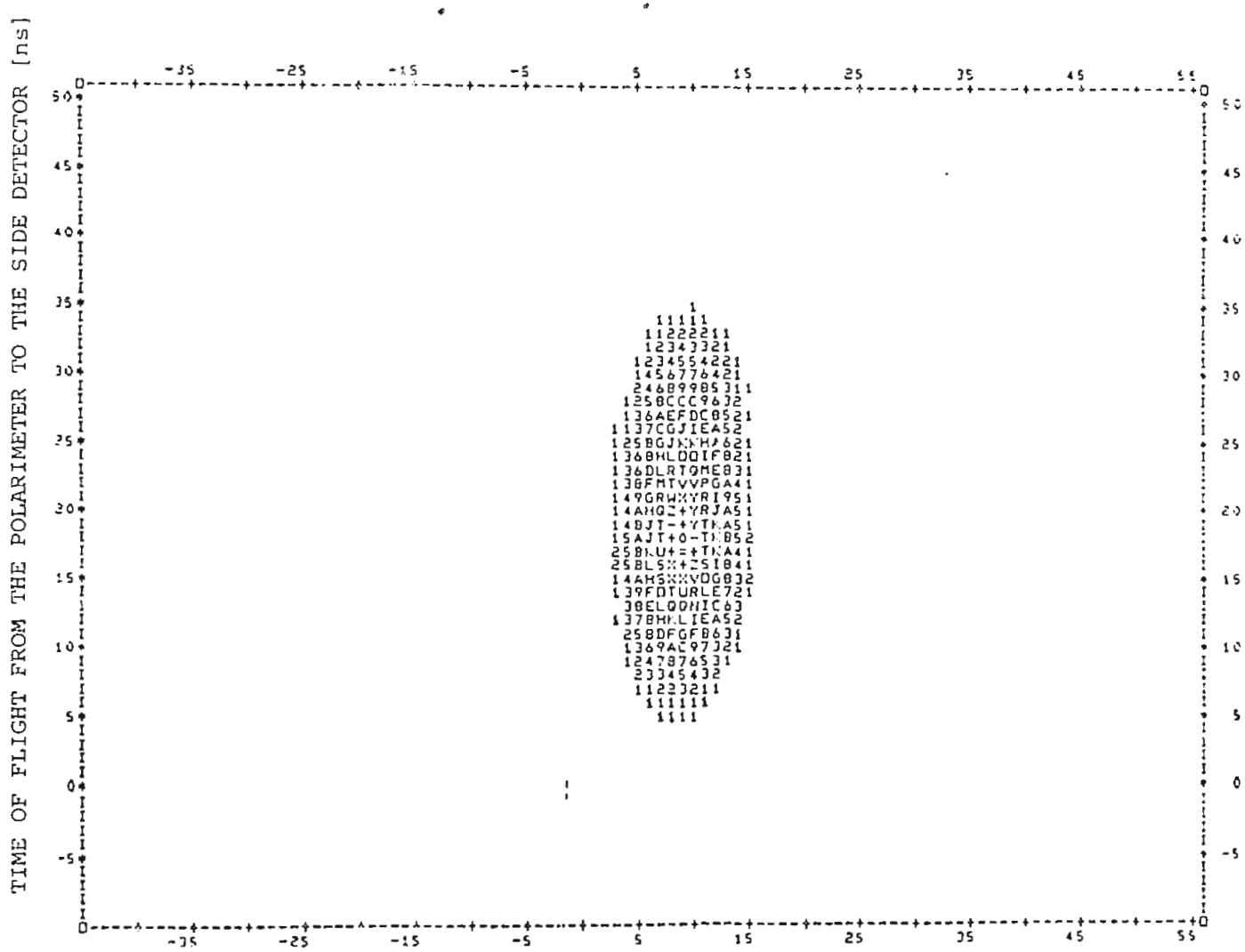

Fig. 3.17 time of flight from the polarimeter to the side detector versus time of flight from the target to the polarimeter calculated by the program.

CHAPTER 4

THE LIQUID POLARIMETER

4.1 THE LIQUID POLARIMETER

4.1.1 INTRODUCTION

Liquid helium has been used for many years in the measurement of neutron polarization (Si61), (Be65), (Pi65), (Mi66), (La68), (Bi68). The known advantage of a large analyzing power, which is relatively flat over a wide range of angles and energies, makes helium particularly suited to this purpose. The high energy of the first excited state of helium, in addition to the fact that the liquid scintillates under bombardment, completes the evidence for the desirability of liquid helium as a neutron polarization analyzer.

Scintillations generated by neutron scattering in liquid helium consist of recombination light following the production of recoiling alpha-particles by neutron bombardment. These scintillations have wavelengths in the far ultraviolet and are converted to the visible region by means of a wavelength shifter; a fluorescent material which is deposited on the inner surface of the vessel containing the liquid helium.

Since neutron scattering experiments involve a double scattering (the first in the production of the neutrons and the second in the actual scattering), they necessarily lead to low count rates and high backgrounds. The signal to background ratio can be improved only slightly by the use of shielding so an alternative means for improvement must be ed. This is achieved using the time of flight

technique where the scintillations from the liquid helium due to (n, α) interactions provide the start pulse. The stop pulse for a time to amplitude converter is provided by the signal produced by the detection of the neutron in the side detectors. From this information the neutron flight time is obtained and hence the neutron energy. This technique reduces considerably the background problem, but is only feasible if high detection efficiency and good timing resolution from the scintillations are obtained.

The liquid helium to be used as analyzer is stored in a cryostat, which must fulfill a number of requirements.

1. It should maintain an adequate level of liquid helium to allow several hours of continuous running. This is important not only from the economic point of view, but also because the low count rates in neutron experiments imply long running periods.

2. To obtain adequate neutron detection efficiency a compromise must be made between increasing the size of the liquid scintillation volume to obtain a higher count rate and decreasing the volume so as to decrease the spread in light collection times. In addition, some care has to be taken to keep to a minimum the amount of material surrounding the helium cell, so that there is a relatively low probability of scattering before the neutron reaches the scintillator.

3. The scintillation light should be collected in the most efficient manner. This is by far the most important problem. The ideal situation would be to have the photomultiplier close to the liquid helium, but because of the likelihood of mechanical damage to the photomultiplier and the fact that there is a decrease in pulse height with decrease in temperature (Bi66), this is not desirable. It is necessary to place the photomultiplier some distance away from the helium and to convey the scintillation to the photomultiplier by means of a suitable light pipe. Further, the material of the light pipe must be chosen so that the wavelength shifted light is conveyed efficiently to the phototube.

An existing liquid polarimeter commissioned originally by J.Birchall(Bi68) fulfills the requirement of having a high light collection efficiency, however, the helium boil-off rate is too high. For this reason we decided to redesign the polarimeter to lower the boil-off rate. It was clear that the main design of the polarimeter should stay the same. However, in order to reduce the temperature gradient of the light-pipe, the light-pipe should be longer and a thermal clamp between the light-pipe and the stainless-steel tube supporting the light-pipe should be made to cool the pipe to liquid nitrogen temperature at a reasonable distance from the liquid helium. This thermal clamp and the addition of a scintillation volume of a unique design built by Ramsay(Ra80) would make the liquid polarimeter more efficient.

4.1.2 THE LIQUID POLARIMETER

The polarimeter is shown in fig 4.1. In this design the viewing photomultiplier is coupled to the upper end of a 5.08cm diameter and 76.2cm long quartz pipe, which stands vertically with its lower end immersed in the liquid helium. No windows are located between the liquid and the photomultiplier, and therefore no problems concerning the matching of refractive indices arise in this case, except at the liquid helium-quartz interface. The photomultiplier and liquid helium are contained within the one vessel, the helium being at 4K while the photomultiplier remains at around room temperature. The 5.08cm diameter light pipe is supported at its lower end by a stainless steel cradle which comes into contact with the quartz over a small area of the end face. This fractionally reduces the effective diameter of the cylinder but avoids the impairment of the optical properties of the quartz inherent in alternative methods of support. At its upper end the quartz is optically coupled to the photomultiplier by means of silicone rubber potting compound (RTV-602). Spring loading of the photomultiplier enables this coupling to be permanently preserved, and allows for thermal contraction and expansion of the light guide and support. The lower end of the light pipe is coated with a layer of $30\mu g/cm^2$ diphenylstilbene (DPS).

Any light entering the pipe from the helium at an angle θ_i will be totally internally reflected at the side wall at an angle θ_c as shown in fig 4.2 if

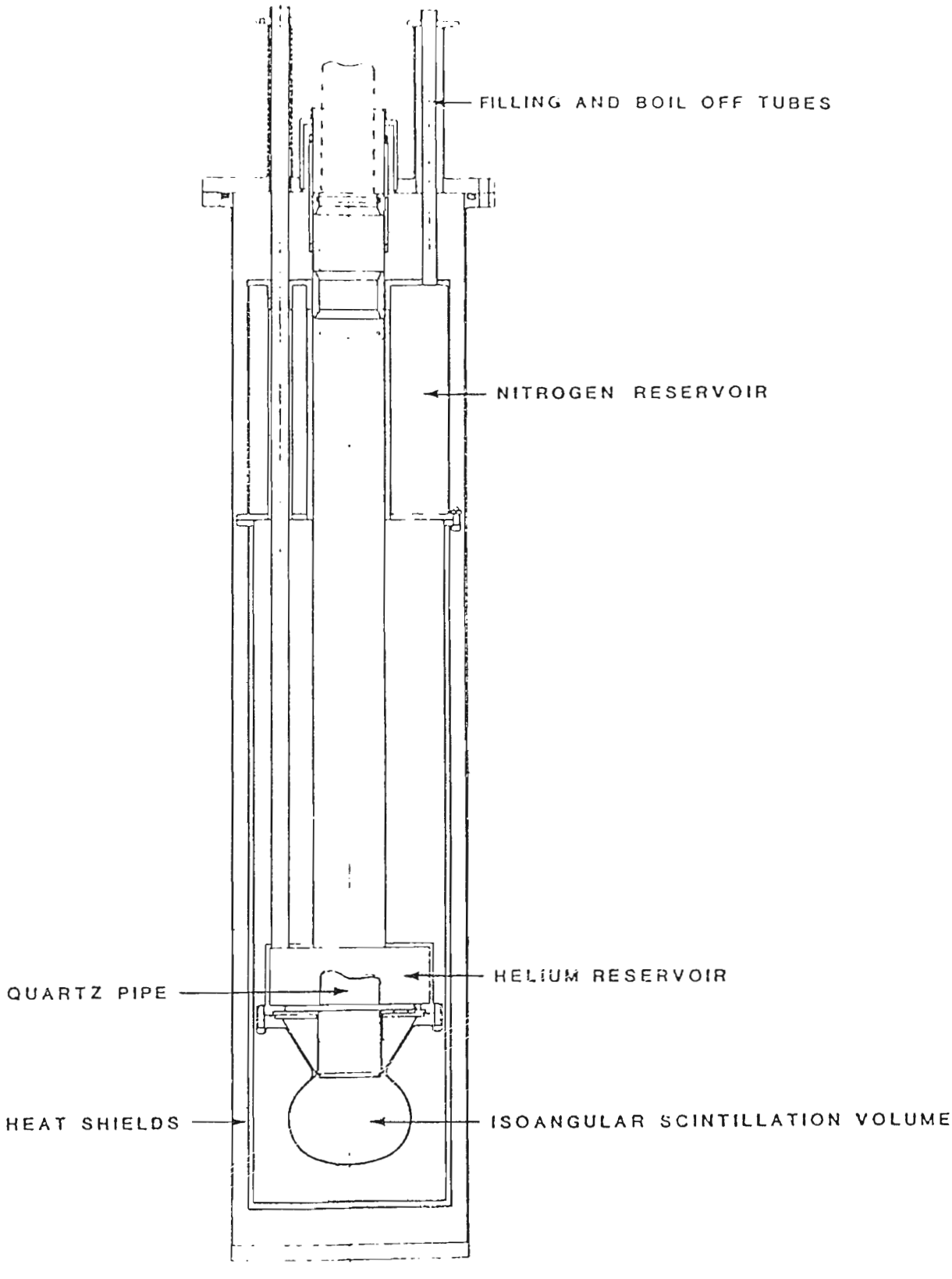

Fig. 4.1 Cross-sectional view of the liquid polarimeter.

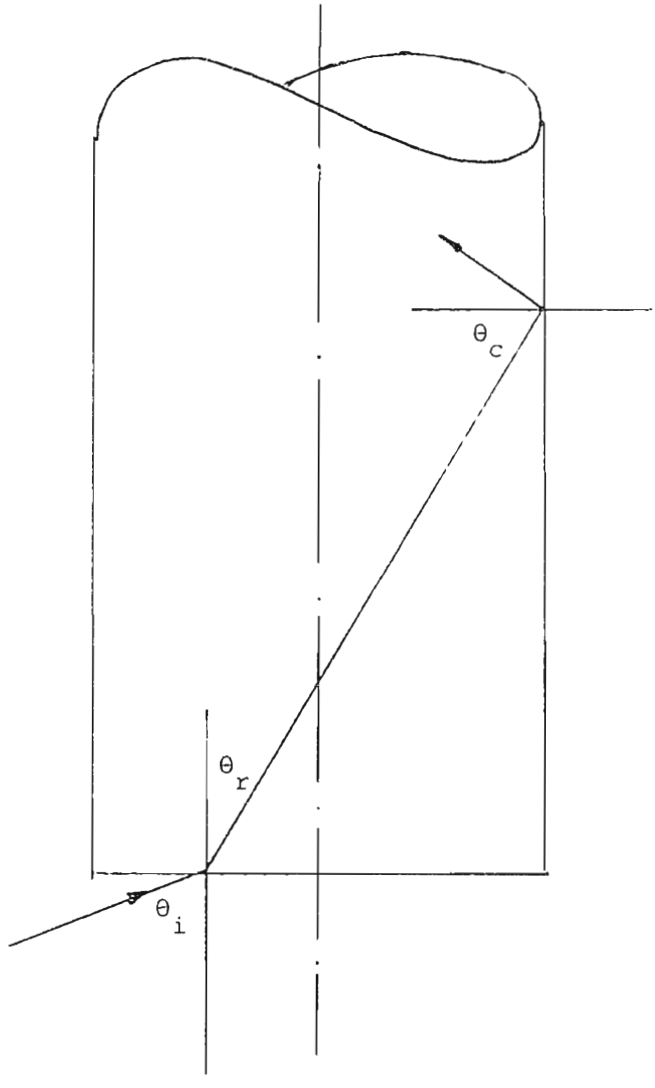

Fig 4.2 Total internal reflection in the light-pipe

$$\sin\theta_c \leq 1/n$$

Therefore

$$\frac{\sin\theta_i}{\sin(90 - \theta_c)} = n$$

$$\sin\theta_i = n\cos\theta_c$$

$$\sin\theta_i \leq (n^2 - 1)^{1/2},$$

where n is the refractive index of the light guide. A refractive index greater than or equal to 1.414 ensures total internal reflection. It is an interesting fact that any light entering the light guide through the side walls cannot leave through the ends if the total internal reflection condition (4.1) is satisfied. This light can only leave through the side walls. This is also valid for the light entering the quartz pipe from the helium. In this case this light must leave the quartz pipe by the other end if the walls of the light pipe are clean and not in contact with anything. However, in order to prevent the helium gas from escaping the light-pipe is sealed with an "O" ring near the top of the pipe. This total internal reflection condition is also lost when the light pipe is coated at one end with a wavelength shifter as is this case.

The liquid helium reservoir is contained in a vacuum chamber, and is surrounded by two highly polished copper heat shields maintained at liquid nitrogen temperature (77K) to cut down thermal radiation into the helium reservoir. The tubes entering the cryostat

are for helium and nitrogen filling and boil-off. They are 1.6cm diameter to avoid the high boil-off produced by thermal oscillations.

The scintillation volume is bolted to the liquid helium reservoir and a helium-vacuum seal between the helium reservoir and the scintillation volume is provided with a special "O" ring made from indium wire.

A narrow rod passes through a rubber "O" ring in the top flange of the cryostat and into the helium reservoir. On the end of the rod is fitted a ^{210}Po alpha source. The source can be positioned below the light guide or be moved away from the guide, allowing a direct calibration of the scintillation spectra. Two carbon resistors are used to measure the temperature. One of them is located almost at the top of the helium tank and the other on the lower part of the helium reservoir. When these two resistors are immersed in liquid helium the resistance increases from 200 and 300 to around 2KΩ and 3KΩ respectively. The change in the value of the resistance provides information about the liquid level, acting as a level indicator rather than as a temperature gauge.

4.2 HEAT LEAKS

In general heat may be transferred by conduction, convection and radiation. In most low-temperature applications, thermal isolation is assisted by partial evacuation of gas from the interior of the cryostat so that convection is eliminated. Then the effective heat transfer takes place by conduction through the residual low-pressure gas,

conduction through the solids that interconnect the various parts of the cryostat and by radiation. Of these three major processes responsible for heat conduction at low temperatures, that due to conduction by solids can be estimated generally with a fair degree of accuracy; low pressure gas conduction and radiation transfer may be estimated with rather less accuracy, the uncertainty depending on our lack of knowledge of the accommodation coefficient and emissivity respectively.

The main sources of heat-leaks in the polarimeter are the following

1. Conduction down the light guide
2. Conduction down the helium gas around the light guide
3. Conduction down the filling and boil-off tubes
4. Conduction down the central tube
5. Thermal Radiation

In the present design the heat leaks have been reduced considerably by

1. doubling the length of the light-pipe (76.2cm)
2. placing a liquid nitrogen thermal clamp 10cm from the top of the light-pipe to ensure a low temperature gradient below the clamp

3. increasing the length of the helium filling and boil-off tubes (80.7cm)

4. reducing the number of helium filling and boil-off tubes from three to two

4.3 HEAT TRANSFER BY CONDUCTION

The heat transfer by conduction is calculated using the following considerations.

The heat flow $\dot{Q}$ through a solid of cross-section A cm^2 under a temperature gradient $\frac{\partial T}{\partial x}$ is given by

$$\dot{Q} = \lambda(T) A \frac{\partial T}{\partial x}$$

$\lambda(T)$ is the temperature-dependent thermal conductivity of the solid.

Thus, if the ends of a solid bar of uniform cross-section are at temperature T_1 and T_2 and there is no heat gain or loss through the sides of the bar,

$$\int_{L_1}^{L_2} \frac{dQ}{dt}\, dx = A \int_{T_1}^{T_2} \lambda(T)\, dT$$

$$\frac{dQ}{dt} = \frac{A}{L}\int_{T_1}^{T_2} \lambda(T)dT$$

To calculate expression 4.1 one should know the thermal conductivity $\lambda(T)$ which depends on the material. Fig 4.3 is a plot of the integral of thermal conductivity from 4K to temperature T as a function of T for stainless steel and fused silica. It is clear that there are two quantities which can be varied in order to achieve a low temperature gradient along the quartz pipe, the length of the light-pipe and the limits on the integral of $\lambda(T)dT$. The idea is to make a thermal clamp somewhere along the quartz pipe to produce a small region of the quartz-pipe readily at liquid nitrogen temperature(77K). In this fashion a low temperature gradient between liquid nitrogen and liquid helium(4.2K) will be produced. If one can ensure the thermal clamp will effectively produce such a temperature gradient then one can be sure the boil-off rate of liquid helium will be considerably reduced. However, from the point of view of light transmission it is not simple to make a mechanical thermal clamp. We already know that anything in contact with the walls of the light-pipe will reduce light transmission of the pipe. Taking into account all these considerations we concluded that a thermal clamp of the form depicted in fig 4.4 will be suitable. This thermal clamp is a cooled helium gas clamp in a region of 2.54cm along the quartz-pipe. The distance between the quartz pipe and the supporting stainless steel tube is 0.5mm. The next question to be

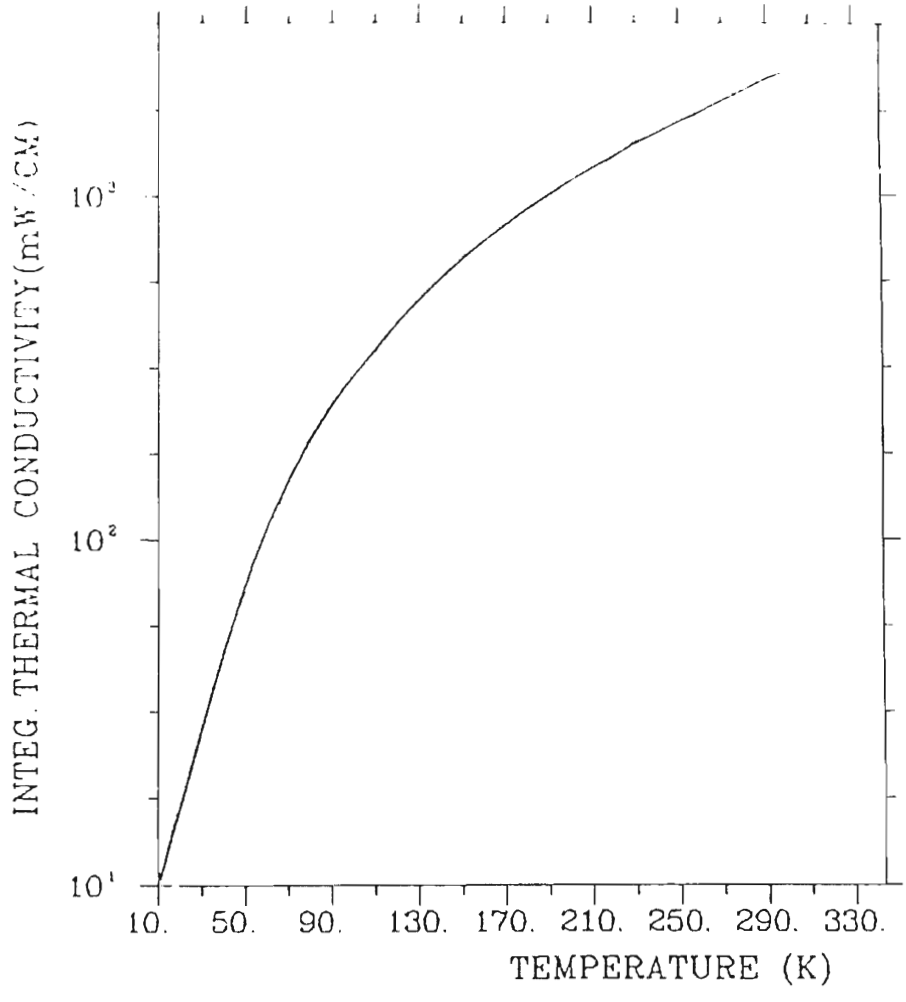

Fig. 4.3a Integral of thermal conductivity for Fused Silica.

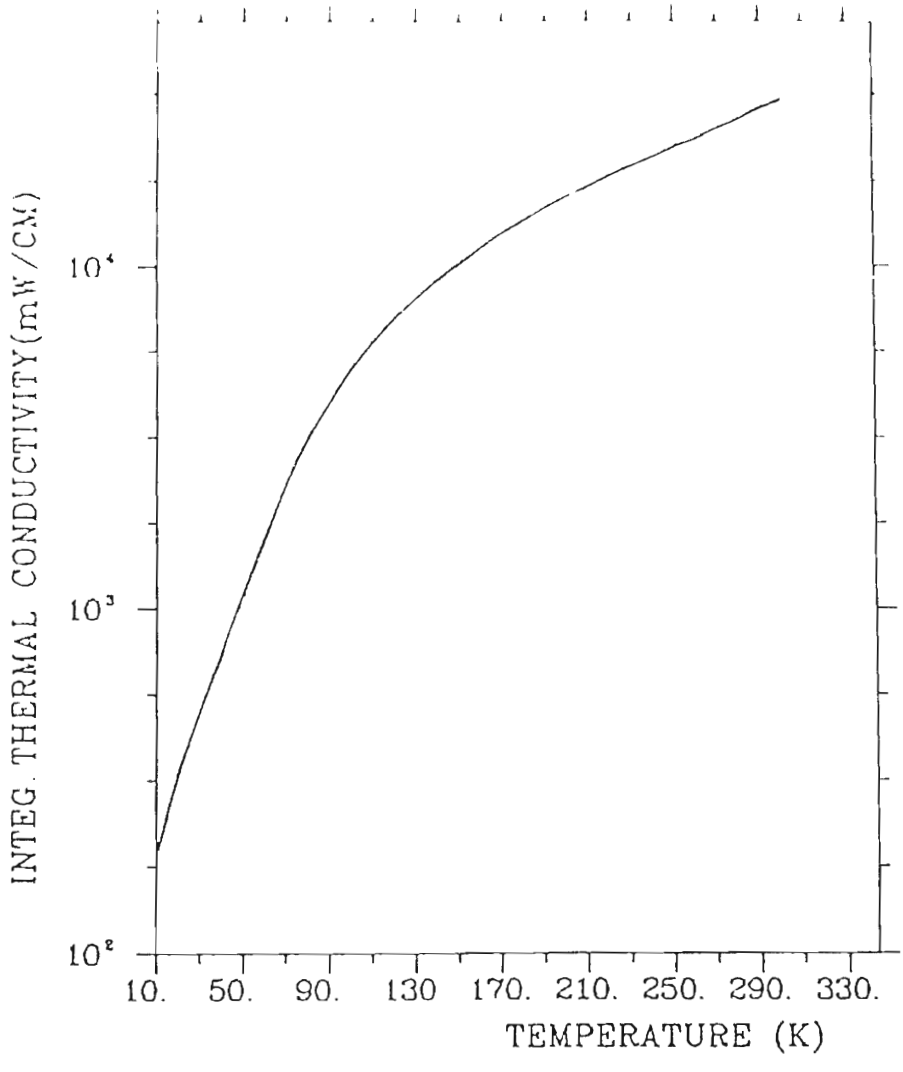

Fig. 4.3b Integral of thermal conductivity for stainless-steel.

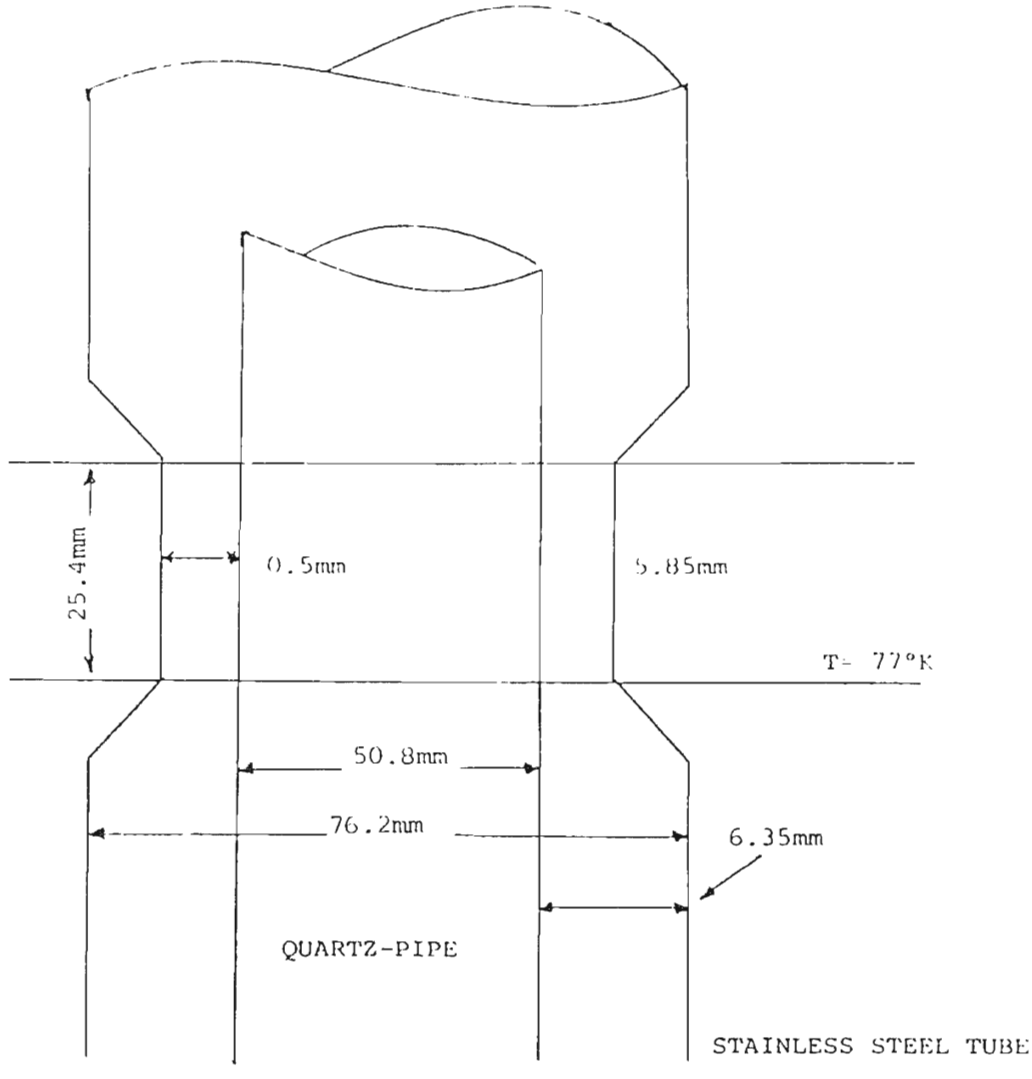

Fig 4.4 View of the thermal clamp used in the liquid polarimeter

answered is how far from the liquid helium this clamp should be located (or how far from the top of the quartz pipe). Calculations done using the above formulation are summarized in table 4.1 (these calculations take into account only the quartz pipe whose length is 76cm). Two different values of the boil-off rate are presented in the table, one for the liquid helium reservoir full and another for the helium reservoir empty. This is so because of the particular design of the polarimeter, part of the quartz pipe is immersed in liquid helium when the helium reservoir is full. It is clear from the table that a clamp located 10cm from the top of the quartz-pipe is preferable.

TABLE 4.1 Heat leak for different clamps

CLAMP AT 20cm FROM THE TOP			
Liquid Helium Reservoir	Heat leak (mw)	L* (cm)	Boil-off Rate(cc/h)
Full	94	44	123
Empty	74	56	98
CLAMP AT 10cm FROM THE TOP			
Full	77	54	101
Empty	63	66	83

* L- Length of the pipe from the clamp to the top of the liquid helium

Table 4.2 shows the results of calculation of heat conduction through the tubes to the liquid helium for the old polarimeter. Table 4.3 are the same calculations for the new polarimeter. In these calculations three cases have been considered.

1. No clamp at all

2. Clamp located 20cm below top of pipe

3. Clamp located 10cm below top of pipe

TABLE 4.2 Heat Leak to liquid helium(mw)

Quartz pipe	Helium gas	2 Filling tubes	Centre tube	Total with quartz pipe	Total without quartz pipe	***
1230	153	119	356	1705	628	NC
680	101	82	246	1008	429	C1, RF
229	34	28	83	340	145	C1, RE
258	38	31	93	382	162	C2, RF
148	22	18	53	219	93	C2, RE

***

NC = No Clamp

C1 = Clamp 1, located 20cm from top of the quartz pipe

C2 = Clamp 2, located 10cm from top of the quartz pipe

RF = Reservoir of liquid helium full

RE = Reservoir of liquid helium empty

TABLE 4.3 Heat leak to liquid helium(mw)

Quartz pipe	Helium gas	2 Filling tubes	Centre tube	Total with quartz pipe	Total without quartz pipe	***
615	77	60	188	853	314	NC
94	14	11	34	139	59	C1, RF
74	11	9	27	110	47	C1, RE
77	11	9	28	113	48	C2, RF
63	9	8	22	93	39	C2, RE

4.4 HEAT TRANSFER BY RADIATION

A perfect black body may be defined as one which absorbs all radiation falling upon it. For such a body the absorptivity "a" and emissivity ε are unity, and so its reflectivity is zero.

$$R = 1-\varepsilon = 1- a$$

For a black body at a temperature T the total radiant energy emitted per second per unit area is given by

$$E = \sigma T^4$$

and emissivities ε_1 and ε_2 at respective temperatures T_1 and T_2, the heat transfer by radiation per unit time is.

$$Q = \sigma A(T_1^4 - T_2^4) \frac{\varepsilon_1 \varepsilon_2}{\varepsilon_1 - \varepsilon_1 \varepsilon_2 + \varepsilon_2}$$

This expression has been used to calculate the thermal radiation.

Because of the design of this polarimeter, the boil-off of liquid helium in the system will depend on whether the helium reservoir is full or empty. The minimum boil-off is obtained when the helium reservoir is empty and the helium is contained only in the scintillation volume. The total heat leak is the sum of the heat leaks due to thermal conduction and the heat leak due to radiation (32.7 mw). The boil-off rate calculated taking in account these two components is 193cc per hour(when the liquid helium reservoir is full) and 165cc per hour when the reservoir is empty this boil-off rate will allow the polarimeter to run around 6 hours whithout being refilled.

4.5 THE SCINTILLATION VOLUME

The scintillation volume in which the liquid helium is contained is traditionally either spherical or cylindrical in shape. A consequence of this is that the scintillation intensity as seen by the phototube for a constant energy deposition in the helium is dependent on the point at which the scintillation originates. This can be appreciated by considering that the visible light is produced by a film of wavelength shifter deposited on the walls of the scintillation

volume and on the end of the light guide. The amount of visible light which is transported to the phototube then depends on the solid angle subtended by the end of the light guide at the point on the film of wavelength shifter producing the light. As this solid angle varies with position on the wall of the scintillation volume, the light transmission to the phototube can be expected to be position dependent. Scintillation volumes are usually coated with a diffuse white reflector, on top of which the wavelength shifter is deposited, to both decrease this position-dependence and increase light yield at the phototube. We have tested a so-called "isoangular" scintillation volume(Vi82) designed by Ramsay(Ra80), in which the solid angle subtended by the end of the light pipe at all points on the inner surface of the volume is a constant in order to decrease the position-dependence further. The prescription of Gardner and Carnesale(Ga69) was used by Ramsay(Ra80) to calculate the solid angle subtended by the end of the light guide.

The isoangular volume was tested with a ^{210}Po alpha-source (E =5.3 MeV) immersed in liquid argon. The technique used in the preparation of liquid argon is the one given by Ramsay(Ra80). Argon is condensed by passing it through 2m of 1.27 cm OD copper tubing arranged in a coil and immersed in liquid nitrogen. A flow rate of two STP gaseous litres per second (estimated from the rate of pressure drop in the argon cylinder) is found to be adequate to prevent freeze-up (at one atmosphere the boiling point of argon is 87.4K and the freezing point 83.8 K, so that in liquid nitrogen at 77K the condensing coil can

easily freeze up) but not so high as to result in feed-through of uncondensed gas. The liquid argon flows directly into the scintillating volume of the polarimeter.

The wavelength shifter used was diphenylstilbene(DPS), 100 $\mu g/cm^2$ on the surface of the scintillation volume and 35 $\mu g/cm^2$ on the end of the light-pipe (this amount of DPS is estimated to be around the optimum quantity to be evaporated in the scintillation volume as well at the end of the light-pipe), evaporated onto a layer of TiO_2 diffuse reflecting paint. The alpha source was attached to a wire which could be moved in a vertical plane across the scintillation volume as indicated in fig 4.5. A pulse height spectrum of the scintillation produced by the alpha source inside the isoangular volume is depicted in fig 4.6. The peak centroid of the scintillation intensity is plotted as a function of alpha source position in fig 4.7 for both a spherical and an isoangular scintillation volume. It is seen that the pulse-height response of the isoangular volume is practically independent of the alpha source position. From these results one can see that the isoangular volume is distinctly superior to a spherical one, improving the pulse height resolution of the polarimeter.

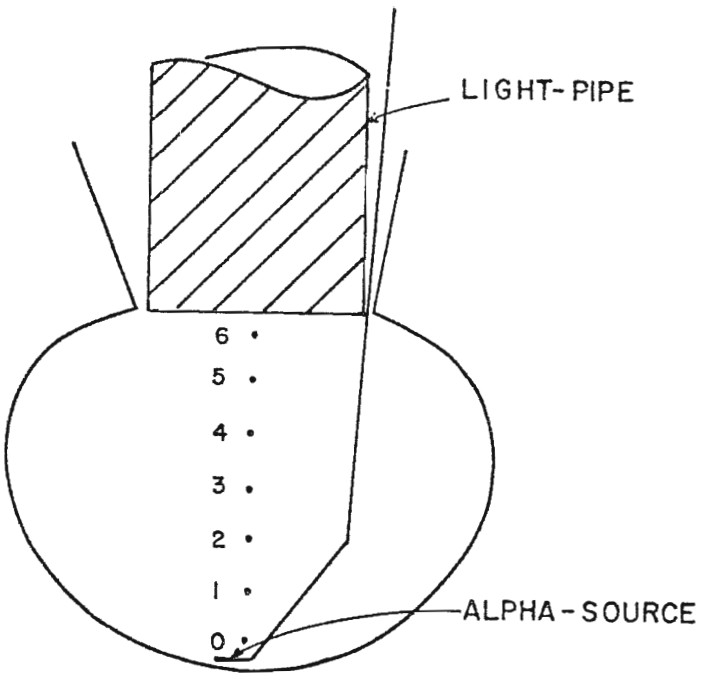

Fig. 4.5 Cross-sectional view of the Isoangular volume.

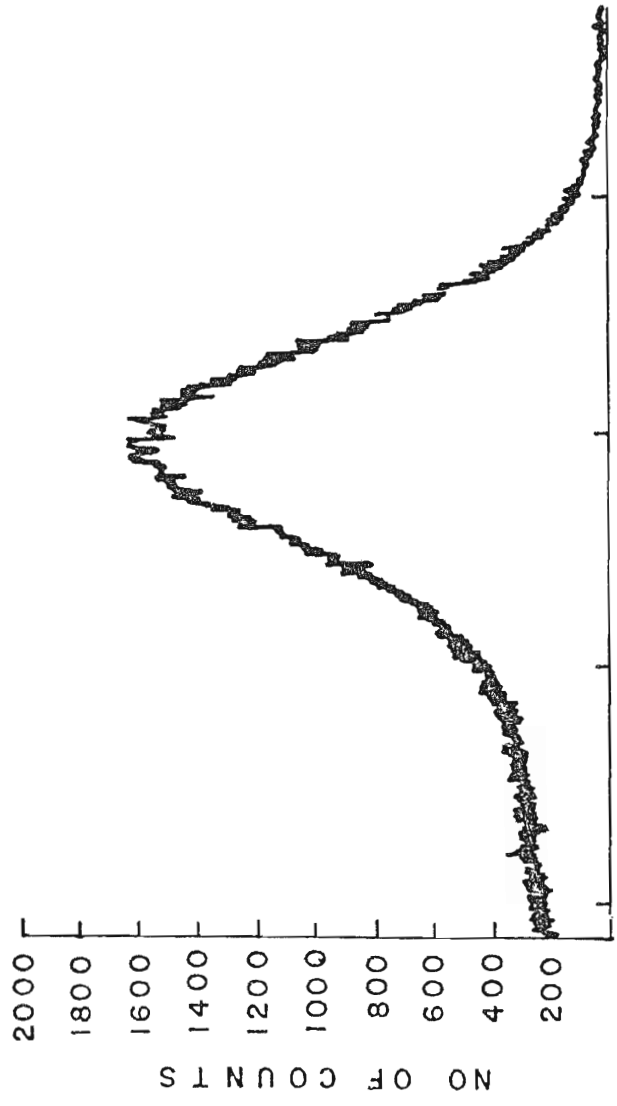

Fig. 4.6 Alpha-source spectrum in the liquid polarimeter.

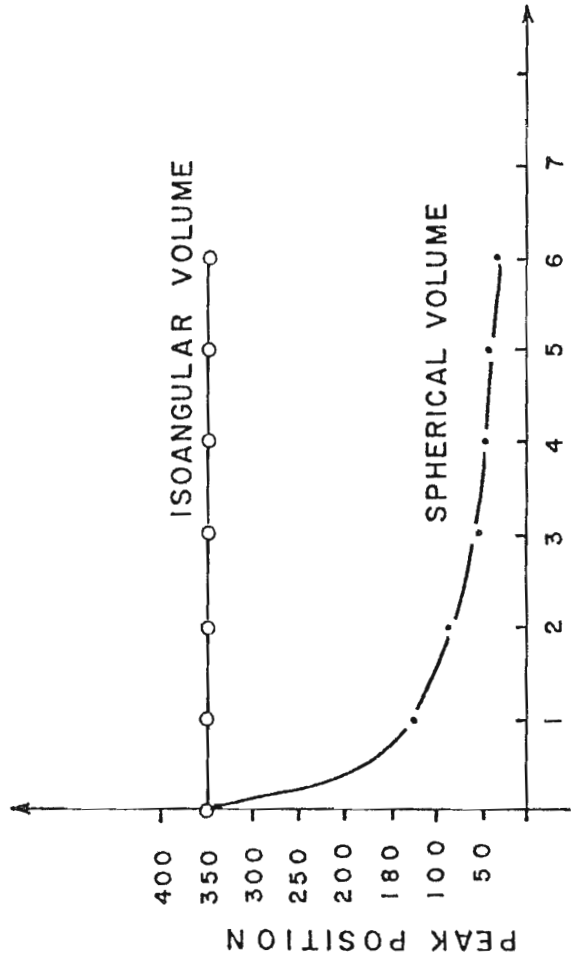

Fig. 4.7 Peak centroid as function of alpha-source position
The line joining the points is to guide the eye.

CONCLUSIONS

A high pressure helium gas polarimeter with remote controlled filling and venting sytems has been built, tested and used during the experiment and is now readily available to be used on a routine basis. The biggest advantage of the gas pol..rimeter over the liquid helium polarimeter is the fact that it can be filled with gas and stored for a long period of time.

A liquid helium polarimeter has been redesigned and at the time of writing these conclusions is already built and being tested.

It is important to have the liquid helium as a second alternative in order to complete the study of the (p,n) reaction in the range of 20 to 50 MeV. At higher energies around 50 MeV there is a decrease in n-He scattering cross section and an increase of He-recoil range, and that calls for a maximum target density, and the density of liquid-helium is roughly 5.5 times that of gaseous helium at 150 atm. In the case of the elastic scattering at 50 MeV the range of a maximum energy He-recoil would be 0.55 cm in liquid helium but 3.0 cm in the high-pressure gas cell. Edge effects arising from the finite target cell size could be excessive with a high-pressure gas cell.

A very reliable Superconducting solenoid (max field 7 tesla) has been tested and used during the experiment.

The asymmetry in the reaction $^{4}He(n,n)^{4}He$ has been measured at 120^{0} for three different energies. The value of the

asymmetry has been corrected for finite geometry and multiple scattering in the target. This is the first set of asymmetry measurements and more experiments are necessary in the range from 20 to 50MeV. However, the aim of the project has been fulfilled, and the initial objective attained. The polarization of neutrons produced in the $^{13}C(p,n)^{13}N$ reaction has been measured by scattering from ^{4}He at 120^{0}.

REFERENCES

(Ar77) Arnold L.G Bull.Am.Phys.Soc.22(1977)588

(At65) Atkinson J and Sherwood J.E Nucl.Instr.and Meth. 34(1965)137

(Ba60) Baicker J.A, and Jones K.W, Nucl Physics 17(1960)424

(Be65) Benenson R.E, Lightbody D.B, Sayres.A Nucl.Insr.and Meth 37(1965)340

(Be53) Bethe H.A Phys.Rev.89(1953)1256

(Bi59) Biedenharn L.C,Nucl.Phys.10(1959)620

(Bi68) Birchall J, Kenny M.J, McKee J.S.C and Reece B.L
Nucl.Instr.and Meth 65(1968)117

(Bi81) Birchall J,McKee J.S.C, Phys.Rev.Lett46(1981)957

(Bl52) Blin-Stoyle R.J, Proc.Phys.Soc,A65(1952)452

(Bo54) Boicourt G.P and Brolley J.E. Rev. Sci. Inst.25(1954)1218

(Br59) Brooks F.D Nucl.Instr. and Meth. 4(1959)1

(By83) Byrd R.C, Floyd C.E, Guss P.P, Murphy K, and Walter R.L,
Nucl.Phys.A399(1983)94

(By81) Byrd R.C, Floyd C.E, Murphy K, Guss P.P, Walter R.L and Cotanch S.R,
Nucl.Phys.A351(1981)189

(By83b) Byrd R.C, Lisowski P.W, Tornow W, and Walter R.L,
Nucl.Phys.A404(1983)29

(Ce79) Cecil R.A, Anderson B.D and Madey R. Nucl.Instr.and Meth.161(1979)439

(Co51) Coester F.C, Phys.rev.84(1951)1259;89(1952)619

(Co60) Connor R.D,and Husain M.K, Nucl.Instr.and Meth, 6(1960)337

(Co74) Conzett H.E,Phys.lett.51B(1974)445

(Da71) Davie H and Galloway R.B Nucl.Instr.and Meth.92(1971)547

(Dr79) Drigo L and Tornielli G, Nucl.Instr.and Meth.166(1979)261

(Du59) Dubbeldam P.S, Jonker C.C and Heemskerk F.J
Nucl.Instr.and Meth.4(1959)23

(Eg54) Eggler C, and Huddleston C.M Phys. Rev.95a(1954)600;
Nucleonic 14(1956)34

(Fo56) Forte M, Nuovo Cim.3(1956)1443

(Ga69) Gardner R.P and Carnesale A, Nucl. Instr. and Meth 73(1969)22

(Gr51) Grun. A.E and Schopper. E.Z, Naturforsch 6a(1951)698 and 9a(1954)13

(Ha67) Hanser F.A Ph.D Thesis Massachusetts Institute of Tecnology(1967)

(He67) Hentschel G, Mack G, and Tornow W Nucl.Instr. and Meth.57(1967)257

(Hi56) Hillman P, Stafford G.H and Whitehead C, Nuovo Cimento 49(1956)67

(Ho61) Hoare F.E, Jackson L.C, Kurti N, Experimental Cryophysics
(Butterworth London)(1961)155

(Ja66) Janni F. Joseph, Technical Report AFWL-TR-65-150 Sept. 1966 Air Force
Weapons Lab. New Mexico

(Ka63) Kane J.K, Siegel R.T, and Suzuki A, Rev.Sci.Instr.34(1963)817

(Ko58) Koch L, Nucl. Electr. Proc. Symp. Paris 1(1958)151

(Ko58b) Koch L and Lesueur R, J.Phys. Radium 19(1958)103

(Ku64) Kurz R.J, UCRL-1139 (March 1964)

(La68) Lam S.T, Gedcke D.A, Stinson G.M, Tang S.M and Sample J.T
Nucl.Instr and Meth. 62(1968)117

(Le66) Lee T.D, Physics Today.19(march.1966)23

(Le50) Lepore J.V, Phys. Rev.79(1950)137

(Ma69) Manduchi C, Moschini G, Tornielli, and Zannoni G,
Nucl.Instr.and Meth.67(1969)267

(Ma67) Marion J.B and Zimmerman B.A Nucl. Instr.and Meth.51(1967)93

(Mc74) McNaughton. M.W, Brady F.P, Broste W.B, Sagle A.L, and Johnson, Nucl.Instr.and Meth.116(1974)25

(Mi66) Miller T.G, Nucl.Instr and Meth. 40(1966)93

(Mi70) Miller T.G, and Morrison F.P Nucl. Instr. and Meth.80(1970)325

(Mo47) Moliere G, Z.Naturforch 2(1947)33

(Mo68) Morgan G.L, and Walter R.L Nucl. Instr. and Meth.58(1968)277

(Mo66) Moss F and Hereford F,Phys Rev 141(1966)141

(Mu81) Murphy K, Byrd R.C, Guss P.P, Floyd C.E, Walter R.L, S.A.Wender and Clegg T.B, AIP Conf.Proc.89(1981)p.1472

(Mu80) Muvdi B.B, and McNabb J.W, Engineering Mechanics of Materials Macmillan publishing Co.,Inc 649(1980)

(Ni59) Nigan B.P,Sundaresan M.K, and Ta-You-Wu Phys.Rev.115(1959)49

(No55) Nobles R.A, Rev. Sci. Instr.27(1956)280

(No55b) Nobles R.A, Henkel R.L and Smith R.K, Phys.Rev.99(1955)616

(No56) Northrop J.A, and Nobles R.A, Nucleonic,14(1956)36

(Oh73) Ohlsen G.G, and Keaton P.W, Nucl.Instr.and Meth.109(1973)41

(Pa56) Palevsky J, Zimmerman R.L, and Larson K.R Rev Sci.Instr.27(1956)323

(Pi65) Piffaretti J, Rossel J, and Weber J,Second Polarization Symp.(152) Karlsruche,1965

(Pl61) Platzman R.L, Inter. J. Appl.Radn.Isotopes 10(1961)116

(RA80) Ramsay D.W, Ph.D. Thesis, University of Manitoba (1980),unpublished

(SA58) Satchler G.R, Nucl.Phys.8(1958)65

(SA57) Sayres A and Wu C.S, Rev. Sci. Instr.28(1957)758

(SE53) Segre E and Wiegand C, Univ. California Radn Lab Rpt. UCRL 2152(1953)

(SI61) Simmons J.E and Perkins R.B, Rev.Sci.Instr. 32(1961)1173

(St71) Stanton R.N, Ohio State University High Energy Physics Laboratory Report.COO-1545-92 (february 1971)

(To74) Tornow W, Z. Physik.266(1974)357

(To75) Tornow W, Spiegelhauer H, and Gunther M, Nucl.Instr.and Meth.125(1975)373

(To77) Tornow W, and Mertens G, Nucl.Instr.and Meth.146(1977)545

(To81) Tornow W, Byrd R.C, Lisowski P.W, Walter R.L, and Donoghue T.R, Nucl.Phys.A371(1981)235

(Vi82) Videla N, Birchall J, McKee J.S.C and Ramsay W, Nucl.Instr.and Meth. 192(1982)61

(Vi55) Villaire A.E and Wouters L.F, Phys.Rev.98(1955)280

(Wa79) Watson J.W,Wilson F.J,Miller C.A and Wells D.? Nucl.Instr.and Meth.164(1979)129

(We51) Wexler A, J. Appl. Physics 22(1951)1463

(Wh68) White G.K Experimental Techniques in Low-Temperature Physics, Oxford 1968

(Wi56) Wilkinson D.H, Phil.mag,1(1956)379